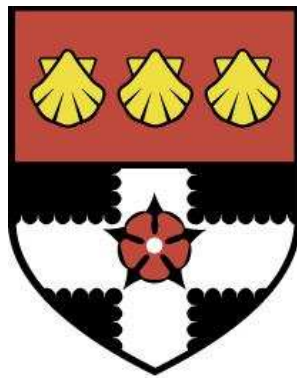


THE UNIVERSITY OF READING

Department of Meteorology



**Representing cloud structure in the
radiation scheme of the Met Office
model**

PETER HILL

A thesis submitted for the degree of Doctor of Philosophy

July 2012

DECLARATION

I confirm that this is my own work and the use of all material from other sources has been properly and fully acknowledged.

Peter Hill

ABSTRACT

Clouds play a fundamental role in the Earth's radiation budget. They have a major impact on surface temperature forecasts and have been identified as the main source of uncertainty in climate prediction. Clouds have significant structure at small scales, but computational constraints mean that general circulation models (GCMs) only resolve cloud structure at much larger scales. The radiative effect of a cloud is non-linearly dependent on its physical properties. Consequently, unresolved cloud structure can have significant radiative effects.

This thesis addresses the problem of representing unresolved cloud structure in GCMs, in particular the Met Office Unified Model (MetUM). We begin by considering evaluation, reduction and impacts of the random errors associated with the Monte Carlo Independent Column Approximation, (McICA, a method for representing the radiative effects of subgrid-scale cloud structure in GCMs). A new method for reducing the magnitude of the noise is described, which halves the noise for an increase in computational cost of less than 50%. By focusing on surface temperature errors, the suitability of McICA for numerical weather prediction models is demonstrated.

Next the subgrid cloud structure itself is considered. Data from several A-train satellites are used to study horizontal water content variability and vertical overlap of clouds. A parametrization of the fractional standard deviation (FSD) of unresolved ice water content is derived, incorporating the effects of horizontal and vertical resolution, and cloud fraction. The observed distribution of overlap is studied and a new parametrization that captures this distribution is described and tested.

Finally the impacts of changes to subgrid-scale cloud structure on 10-year MetUM climate simulations are investigated. Global mean cloud radiative effects (CRE) may be changed by as much as 10%. Local changes to cloud cover, surface temperature and precipitation rate can be quite large, but are not statistically significant. Compared to a simulation using the same mean value globally, the FSD parametrization reduces CREs by around 1 Wm^{-2} , which implies that a globally varying FSD is necessary to obtain unbiased CREs.

ACKNOWLEDGEMENTS

First, I would like to thank my supervisors, Robin Hogan and James Manners, for their guidance and constructive criticism, and their patience in reading through various versions of this thesis.

I'm grateful to Richard Allan and Pete Innes of my monitoring committee and Ian Boutle, Cyril Morcrette, Jon Petch and Jonathan Wilkinson of the Clouds and Radiation group at the Met Office, for their advice and insightful comments.

I'd like to express my gratitude to my managers at the Met Office (Andy Brown, Brian Golding, Roy Kershaw and Jon Petch), for allowing me the funding and time to do this work.

Many thanks to my parents, Ruth and Robert, and to my siblings, Tom, Rozi and Mairéad for their encouragement and support.

Finally, a very big thank you to Sam, for her love, empathy and inspiration and for being there when I needed her.

- Peter Hill - July 2012

CONTENTS

1	INTRODUCTION	1
1.1	RADIATIVE TRANSFER AND CLOUDS	1
1.2	THE REPRESENTATION OF CLOUD-RADIATION INTERACTIONS IN GCMs	3
1.3	EVALUATING CLOUD-RADIATION INTERACTIONS IN GCMs	7
1.4	SUB-GRID CLOUD WATER CONTENT INHOMOGENEITY	9
1.4.1	REPRESENTING CLOUD HORIZONTAL INHOMOGENEITY	9
1.4.2	HOW MUCH INHOMOGENEITY EXISTS?	11
1.4.3	EFFECTS OF REPRESENTING INHOMOGENEITY	12
1.5	CLOUD VERTICAL OVERLAP	14
1.5.1	CONTIGUOUS CLOUDS	15
1.5.2	NON-CONTIGUOUS CLOUDS	16
1.5.3	EFFECTS OF CHANGING OVERLAP	17
1.6	THIS THESIS	17
1.6.1	AIMS	17
1.6.2	OUTLINE	18

2	REDUCING NOISE ASSOCIATED WITH McICA FOR WEATHER FORECASTING MODELS	20
2.1	INTRODUCTION	20
2.2	THE McICA METHOD AND ITS IMPLEMENTATION	22
2.2.1	THE McICA METHOD	22
2.2.2	IMPLEMENTATION IN THE MET OFFICE UNIFIED MODEL	23
2.3	EVALUATION AND OPTIMISATION OF NOISE	25
2.3.1	METHODS FOR REDUCING NOISE	25
2.3.2	TEST SET-UP AND RESULTS	28
2.3.3	COMBINING SW AND LW ERRORS	32
2.4	THE EFFECT OF McICA NOISE ON AN NWP MODEL	36
2.4.1	MODEL SET-UP	37
2.4.2	RESULTS	38
2.5	CONCLUSIONS	42
3	PARAMETRIZING THE HORIZONTAL INHOMOGENEITY OF ICE WATER CONTENT USING CLOUDSAT DATA PRODUCTS	43
3.1	INTRODUCTION	43
3.2	CLOUDSAT DATA	46
3.3	SPECTRAL ANALYSIS	47
3.4	HORIZONTAL SCALE	50
3.5	VARIABILITY AS A FUNCTION OF CLOUD FRACTION	53

3.6	VERTICAL LAYER THICKNESS	57
3.7	PARAMETRIZATION	61
3.7.1	COMPARING OBSERVED FSD TO MODELLED FSD	61
3.8	SUMMARY	65
4	CLOUD VERTICAL OVERLAP	67
4.1	INTRODUCTION	67
4.2	OBSERVATIONAL DATA	69
4.3	OVERLAP PARAMETERS	71
4.4	RANDOM OVERLAP AND HORIZONTAL CLOUD STRUCTURE	72
4.5	OVERLAP FOR VERTICALLY CONTIGUOUS CLOUDS	75
4.6	OVERLAP FOR CLOUDS SEPARATED BY CLEAR LAYERS	78
4.7	OVERLAP PARAMETRIZATIONS	81
4.7.1	COMPARISON OF OBSERVED AND PARAMETRIZED β	85
4.7.2	EFFECT ON TOTAL CLOUD COVER AND OLR	89
4.8	CONCLUSIONS	94
5	THE IMPACT OF CHANGES TO SUBGRID CLOUD STRUCTURE ON CLIMATE SIMU- LATIONS	96
5.1	INTRODUCTION	96
5.2	MODEL CONFIGURATION	97
5.3	MODELLED FSD CLIMATOLOGY	99

5.4	EFFECT OF FSD PARAMETRIZATION	104
5.4.1	GLOBAL MEAN EFFECTS	104
5.4.2	IMPACT ON GEOGRAPHICAL DISTRIBUTIONS	107
5.5	CONCLUSIONS	111
6	CONCLUSIONS AND FUTURE WORK	114
6.1	SUMMARY AND CONCLUSIONS	114
6.2	FUTURE WORK	116
	BIBLIOGRAPHY	120

CHAPTER 1:

INTRODUCTION

Calculating the significant radiative effect of clouds is one of the most important requirements of the radiative transfer schemes employed in general circulation models (GCMs). It is also one of the most uncertain aspects of the radiative transfer calculation, due to the complex structure of clouds at temporal and spatial scales much smaller than can be resolved by GCMs. The non-linear relationship between radiation and clouds means that incorrect assumptions about cloud properties at subgrid-scales may cause radiative biases even if the cloud properties are accurate at the resolved scale.

This chapter describes the background to and motivation for this thesis. We begin by emphasising the critical nature of radiative transfer schemes in numerical weather prediction (NWP) and climate models, and in particular the importance of their cloud representation. We then describe how the radiative effects of clouds are calculated in GCMs, highlighting the approximations that are applied and may be improved and focusing in particular on the Edwards-Slingo radiative transfer scheme (E-S) used in the Met Office Unified Model (MetUM). In section 1.3 we briefly discuss how GCM cloud-radiation interactions are validated. In sections 1.4 and 1.5, we discuss the two aspects of subgrid cloud representation addressed by this thesis, horizontal cloud water content variability and cloud vertical overlap. This chapter concludes with a description of the goals of this project, followed by an outline of the thesis.

1.1 RADIATIVE TRANSFER AND CLOUDS

Ultimately, almost all the energy in the earth system originates from the sun and arrives in the form of radiative energy. The global mean solar (also known as shortwave, SW) insolation is around 340 Wm^{-2} (Trenberth *et al.*, 2009). This is not distributed uniformly and the geographical and temporal differences in solar insolation and hence heating drive the large-scale circulation of

the atmosphere. Infrared (also known as longwave, LW) radiation is emitted by the earth system into space and also redistributes energy within the atmosphere. The distribution of radiative energy is sensitive to many of the other properties of the atmosphere (e.g. temperature, clouds, aerosols, gases) and constantly evolves in response to atmospheric changes. Moreover, anthropogenic activity can change the properties of the atmosphere and hence influence the distribution of radiation; the most famous example being the emission of carbon dioxide, which absorbs LW radiation, leading to warming of the earth's surface. Consequently most NWP and climate models include interactive radiative transfer schemes.

Given a well-characterised atmosphere and sufficient computational resources, it is possible to perform very accurate radiative transfer calculations (e.g. Cahalan *et al.*, 2005). However, in GCMs, many of the input parameters must be predicted by the model (e.g. cloud properties and vertical temperature profiles) and may contain large errors. Moreover, in GCMs it is necessary to balance the accuracy and computational cost of the radiation scheme, resulting in compromised spectral, temporal and spatial resolution and numerous simplifications, such as the two-stream approximation (Meador and Weaver, 1980) which reduces the 3D calculation to two discrete directions.

Clouds are a key component of the earth's radiation budget. The radiative effect of a cloud depends on many aspects of the cloud, both microphysical (e.g. droplet size distribution) and macrophysical (e.g. coverage and height), and also on many non-cloud parameters (e.g. surface albedo). Consequently, the distribution of cloud radiative effects is very broad and clouds can cause either cooling or heating of the surface. The global mean effect of clouds is a cooling of the atmosphere by around 15 Wm^{-2} , which arises due to an imperfect cancellation between mean SW cooling and mean LW heating (Ramanathan *et al.*, 1989). Instantaneous local cloud radiative effects (CRE) may be much larger, with instantaneous estimates of SW CRE in excess of -400 Wm^{-2} and LW values as large as 100 Wm^{-2} (e.g. Allan, 2011). As mean CREs are large, relatively small errors can exceed in magnitude the effect of other significant atmospheric constituents. For example the forcing due to doubling the concentration of carbon dioxide in the atmosphere, estimated to be around 3.7 Wm^{-2} (Ramaswamy *et al.*, 2001), is equivalent to around 25% of the global mean net CRE.

In NWP models, the interactions of cloud and radiation have large impacts on surface temperature, which is a critical forecast variable, used for example in road gritting decisions. By reflecting solar radiation, clouds cool the surface. However, clouds also trap LW radiation, so low clouds cause LW warming of the surface. The net effect depends on the magnitude of solar insolation and the cloud and surface properties, but generally clouds cool the surface during the day and warm it at night.

Despite the obvious importance of clouds in both NWP and climate models, and the considerable time devoted to their study, they remain a leading source of uncertainty and errors. Cloud feedbacks have long been identified as the dominant source of uncertainty in climate prediction (e.g. Cess *et al.*, 1990) and clouds remain the foremost source of differences between GCMs (Soden and Held, 2006). This is generally attributed to differences between the gridbox-mean cloud properties predicted by the cloud schemes rather than differences in the radiation schemes. Nevertheless, there is significant scope to improve the radiative treatment of clouds; a recent inter-comparison of radiation codes (Oreopoulos *et al.*, 2012) found CRE percentage errors larger than 20%. A reduction of radiative errors and biases may lead to improvements in other model fields, either directly by refining the temperature fields, or indirectly by allowing existing compensating errors to be removed. Moreover it would lead to better evaluations of other model fields (particularly cloud fields), which are often assessed through their radiative effects (e.g. Allan *et al.*, 2007; Su *et al.*, 2010).

1.2 THE REPRESENTATION OF CLOUD-RADIATION INTERACTIONS IN GCMs

This section describes how the radiative impacts of clouds are calculated in a typical GCM, with a particular focus on the MetUM (e.g. Walters *et al.*, 2011), which is used in this thesis. The MetUM is used operationally across many different spatial and temporal resolutions, from high resolution (1.5 km) forecasts of UK weather over the next two days to climate modelling over hundreds of years using horizontal resolutions on the order of 100 km. The E-S radiative transfer scheme (Edwards and Slingo, 1996) is used to calculate radiative fluxes and heating rates in all versions of the MetUM.

Numerical models of the atmosphere generally divide the atmosphere into discrete gridboxes. These gridboxes are not usually small enough to resolve individual clouds, so cloud schemes are used to predict the proportion of each gridbox that is cloudy, the proportion of the cloud that consists of each phase (i.e. ice and liquid), and the mean liquid and ice water content within the cloudy part of the gridbox. Generally clouds are assumed to fill the gridbox vertically and partially fill it horizontally and each gridbox is considered independently. However, parametrizations exist (e.g. Boutle and Morcrette, 2010), that reduce the extent to which the gridbox is filled in the vertical by spreading the cloud over a larger horizontal area. GCM cloud fields may include quite large biases and errors, as discussed in section 1.3.

The cloud schemes in modern GCMs can be broadly divided into two categories: prognostic and diagnostic. In diagnostic schemes (e.g. Smith, 1990), instantaneous cloud properties are determined from the large-scale variables (e.g. temperature and humidity). Diagnostic schemes have no memory; cloud properties are calculated afresh on each time-step. However, they are simpler and require less computational resources than prognostic schemes. In prognostic schemes (e.g. Tiedtke, 1993) some cloud properties are ‘remembered’ from time-step to time-step and advected around by the large-scale flow. On each time-step, these prognostic variables are modified by each of the physical processes in the model. Note that not all the cloud properties in a prognostic scheme are prognosed, some are diagnosed. In the MetUM simulations described in this thesis, cloud fields are handled by the prognostic cloud fraction, prognostic condensate (PC2) cloud scheme (Wilson *et al.*, 2008a). PC2 prognoses liquid, ice and total cloud fractions, water vapour, and ice and liquid condensate. Increments to each of these prognostic variables are calculated from each physical process represented in the MetUM. For each gridbox, separate gridbox-mean liquid and ice water content mixing ratios and a cloud fraction are passed to the E-S radiation scheme.

Conceptually, one of the most fundamental approximations used in GCM radiative transfer schemes is the neglect of the full 3D dimensionality of the problem. While full 3D calculations are possible (e.g. Cahalan *et al.*, 2005), they are very computationally expensive. Consequently, in GCMs, only vertical fluxes are calculated and the effect of horizontal photon transport is ignored. The difference between full 3D calculations and 1D calculations is known as the 3D effect (e.g. Pincus *et al.*, 2005). For clear-sky calculations, the 3D effect is small; the effect of horizontal

photon transport in opposite directions tends to cancel. For a cloudy domain, the magnitude of the 3D effect depends on the properties of the cloud (e.g. Gounou and Hogan, 2007) and, in the SW, the solar zenith angle (e.g. Tompkins and Giuseppe, 2007). Efficient methods for approximating the 3D effect in GCM radiative transfer schemes are in development (e.g. Hogan and Shonk, 2012). However, as far as we are aware, such techniques have yet to be incorporated into any GCM. Consequently, the global mean magnitude of the 3D effect is unknown.

Atmospheric extinction spectra show significant variability over small spectral intervals. To account for this variability, most GCM radiative transfer schemes employ the correlated k-distribution method (e.g. Lacis and Oinas, 1991). The SW and LW spectra are each divided into a number of bands. Cloud optical properties are generally assumed to be ‘grey’; they are constant across each band. Each band is divided into ‘k-terms’, which represent all the wavelengths within the interval that have a similar absorption coefficient. A pseudo-monochromatic radiative transfer calculation is performed for each k-term. The fluxes for each k-term are summed with appropriate weighting to calculate the fluxes for each band, which are summed to give the total SW or LW flux. The division of the spectrum into bands and k-terms varies from model to model; increasing the number of bands or k-terms leads to more accurate fluxes and heating rates, but at greater computational expense. In the E-S scheme, the configuration of bands and k-terms depends on the particular ‘spectral file’ used, making the model very flexible.

Within each spectral band, cloud optical properties are calculated in terms of scattering and extinction coefficients and the asymmetry parameter. Numerous parametrizations of the cloud optical properties exist (e.g. Slingo and Schrecker, 1982; Fu, 1996). The current operational version of the MetUM uses the liquid parametrization of Edwards and Slingo (1996) and the ice parametrization of Edwards *et al.* (2007). In reality, the mean in-cloud optical properties depend on the distribution of water content and droplet/crystal sizes within the cloud. Up until relatively recently, most GCM radiative transfer schemes calculated cloud optical properties using the mean in-cloud water content and droplet/crystal size; subgrid variability of microphysical cloud properties was ignored. This is commonly known as the plane-parallel homogeneous approximation. The radiative effect of a cloud is non-linearly dependent on both the water content and the droplet/crystal size. As a result, neglecting the subgrid-scale variability of either leads to a biased estimate of the effect on the domain mean fluxes and heating rates (Räisänen *et al.*, 2003).

The water content homogeneity bias is much larger than the droplet/crystal size homogeneity bias (Barker and Räisänen, 2004) and has been much more widely studied (e.g. Borde and Isaka, 1996; Cairns *et al.*, 2000). The water content homogeneity bias is one of the main problems addressed in this thesis and more detail is available in section 1.4.

As GCMs allow layers to be partially filled with cloud, the solution to the radiative transfer problem depends on the proportion of the radiative fluxes that are transferred between cloudy and clear-sky regions as they pass through layer boundaries. This is determined by the cloud overlap assumption, which is generally incorporated into the radiative transfer solver (e.g. Geleyn and Hollingsworth, 1979). A number of different overlap assumptions have been used in GCMs, including random, maximum-random (Geleyn and Hollingsworth, 1979) and exponential-random (Hogan and Illingworth, 2000). Changes to cloud overlap can have large impacts on the radiative transfer calculation and this is one of the aspects of the cloud representation considered in this project. Cloud overlap is discussed in further detail in section 1.5 and chapter 4.

Despite the numerous simplifications described above, most GCM radiative transfer schemes are too computationally expensive to run on every model time-step and are run with a lower temporal resolution than the rest of the model. Several methods have been suggested to reduce the computational burden of radiative transfer schemes and improve the sampling of the fast-changing cloud field. One method involves compromising between spatial and temporal resolution (Morcrette, 2000). Another solution involves ‘adaptive’ radiative transfer schemes, where expensive, accurate calculations are only performed when most needed, and cheaper, more approximate calculations are performed more regularly (Venema *et al.*, 2007). In the MetUM, ‘incremental’ time-stepping (Manners *et al.*, 2009) is adopted. This involves two different radiative transfer calculations in both the SW and LW: an expensive ‘full’ calculation, using many monochromatic calculations to represent the whole of the SW/LW spectrum and a cheaper, more frequent ‘incremental’ calculation, which uses only one or two pseudo-monochromatic calculations to represent the optically thin part of the spectrum that is most responsive to changes in the cloud field. The frequency of these calculations depends on the model configuration. In the GA3.0 configuration (Walters *et al.*, 2011), full radiative calculations are performed every three hours while incremental calculations are made every hour.

1.3 EVALUATING CLOUD-RADIATION INTERACTIONS IN GCMs

Evaluation of GCM clouds fields, radiation fields, and their interactions is a difficult process. Ground based in-situ observations and aircraft observations have poor coverage, but may be useful for case studies. Satellite observations have better (but still not complete) coverage, but only measure radiation; they cannot measure cloud properties directly. Most GCMs are continually evolving and observational evaluation often lags the model development by several model versions (as illustrated below). Nevertheless, it is useful to consider this subject briefly, if only to provide further context for the results described later in this thesis. By briefly considering a small subset of the vast body of literature on this subject, we shall show that errors in clouds and radiation vary from GCM to GCM and between different versions of the same model, but MetUM errors remain fairly typical of the errors observed in other GCMs.

Radiation fields at the top of the atmosphere (TOA) can be directly measured by passive satellites, which observe broad areas instantaneously. Allan *et al.* (2007) compared around three years (2004-2007) of forecasts of TOA fluxes from several operational cycles (G32-G42) of the global MetUM with geostationary earth radiation budget (GERB) satellite observations. Several systematic errors linked to clouds were identified. Over Europe, a net (SW+LW) model bias of over 30 Wm^{-2} was found to correspond to underestimates of cloud fraction by around 20%, while model overestimates of cloud water content were implicated in a 60 Wm^{-2} overestimate of the TOA reflected SW flux over marine stratocumulus clouds. Greuell *et al.* (2011) conducted a similar study, comparing version two of the Regional Atmospheric Climate Model (RACMO) to GERB observations over Africa for July 2006. They found large radiative errors in the opposite direction in the simulation of marine stratocumulus, with cloud cover, cloud water path and albedo all underestimated. Moreover, in the continental intertropical convergence zone (ITCZ), the mean modelled outgoing LW radiation at the top of the atmosphere (OLR) was 30 Wm^{-2} too high, which was attributed to the modelled cirrus clouds being too thin. Marine stratocumulus have also been found to be poorly simulated by other GCMs. For example, Wild and Roeckner (2006) found that European Centre Hamburg Model 5 (ECHAM5) underestimated the seasonal mean SW CRE of marine stratocumulus by as much as 40 Wm^{-2} .

Although cloud properties cannot be measured directly by satellites, algorithms exist to retrieve cloud properties from the observed quantities (e.g. Delanoë and Hogan, 2010). The retrieved cloud fields can then be compared to GCM cloud fields. Delanoë *et al.* (2011) used CloudSat observations to compare the retrieved distribution of ice water content to modelled (cycle G40, operational from June-September 2006 of the MetUM global forecast model and cycle 32r3 of the European Centre for Medium-Range Weather Forecasts (ECMWF) global model) distributions. They found that both models captured most of the features of the ice water content distribution reasonably well. Moreover, most of the deficiencies of MetUM ice water content distribution were replicated by the ECMWF model. However, other studies are less complimentary about the representation of ice clouds in GCMs. Eliasson *et al.* (2011) compared estimates of monthly average ice water path (IWP) from CloudSat to estimates from other satellites and used this information to evaluate a subset of the Intergovernmental Panel on Climate Change (IPCC) Fourth Assessment Report (AR4) climate models. There were large discrepancies between the models and all models had difficulty capturing the observed IWP distribution.

An alternative approach, which is becoming increasingly popular, is to simulate the observed quantities using the GCM. Bodas-Salcedo *et al.* (2008) estimated radar reflectivity from cycle G42 (operational from December 2006 to May 2007) MetUM global forecast fields, and compared the values to observed CloudSat reflectivity. Clouds and the Earth's Radiant Energy System (CERES) and Earth Radiation Budget Experiment (ERBE) observations were used to show corresponding differences in TOA CREs. Midlatitude systems were found to be better represented than tropical convection, though the occurrence of midlatitude clouds below 5 km was underestimated. Modelled convective cloud amounts around 8-12 km were overestimated but above and below this height, they were underestimated, leading to a 5-10 Wm^{-2} underestimate of LW CRE. For the marine stratocumulus region off California, they found that LW CRE was underestimated (by around 5 Wm^{-2}) due to too few high cirrus clouds in northern hemisphere winter, while SW CRE was overestimated (by around 7 Wm^{-2}) due to an overestimate of the amount of thick low cloud. Zhang *et al.* (2010) simulated CloudSat and Cloud-Aerosol Lidar and Infrared Pathfinder Satellite Observation (CALIPSO) observations in the tropics using the community atmosphere model (CAM). In order to minimise the impact of large-scale dynamics on their analysis, they ran short-range forecasts and studied the average results. Many of the errors in the CAM simulation are similar to the MetUM errors discussed by Bodas-Salcedo *et al.* (2008), for example the frequency

of occurrence of stratocumulus clouds is overestimated by the CAM.

1.4 SUB-GRID CLOUD WATER CONTENT INHOMOGENEITY

1.4.1 REPRESENTING CLOUD HORIZONTAL INHOMOGENEITY

As indicated in section 1.2, CREs depend non-linearly on cloud water content (e.g. Han *et al.*, 1998). Moreover, as we shall discuss in section 1.4.2, observations of cloud water content show that it exhibits significant horizontal variability at scales that are unresolved by GCMs. Combining this knowledge with Jensen's inequality (Jensen, 1906), it is clear that the domain mean cloud water content is insufficient information for calculating the correct domain mean radiative fluxes and heating rates. The problem of neglecting horizontal inhomogeneity has long been recognised (e.g. Weinman and Swartztrauber, 1968). Nevertheless, up until the last decade, the radiative transfer schemes used in most GCMs simply used the gridbox mean cloud water content and assumed that clouds were horizontally homogeneous. Unresolved water content variability is also important for microphysics and thermodynamics (e.g. Larson *et al.*, 2001; Jakob and Klein, 1999). For example, many autoconversion parametrizations are non-linearly dependent on cloud water content.

Early studies of the radiative effect of cloud horizontal inhomogeneity (e.g. Van Blerkom, 1971; McKee and Cox, 1974) generally used 3D radiative transfer models. Hence the radiative effects of inhomogeneity and horizontal photon transport were combined. For the domain sizes generally used in global NWP or climate models, the effect of horizontal photon transport on the domain mean radiative fluxes is smaller than the inhomogeneity effect (Barker *et al.*, 1999). Cahalan *et al.* (1994b) disentangled inhomogeneity and horizontal photon transport by estimating the effect of inhomogeneity when horizontal photon transport is neglected. This is a much more straightforward problem.

The most effective method for representing horizontal inhomogeneity consists of dividing each horizontally inhomogeneous domain into a number of horizontally homogeneous sub-columns, each containing a different water content and a cloud fraction of either one or zero. This is often referred to as the independent column approximation (ICA) (Ronnholm *et al.*, 1980), or

the independent pixel approximation (IPA) and this is what is meant by ICA in this thesis. The number of sub-columns needed depends on the cloud field and accuracy required. Full 3D radiative transfer models (e.g. Monte Carlo photon transport algorithms, Barker *et al.* (1998)) may be used to estimate the impact of the neglect of net horizontal photon transport by the ICA (e.g. Barker and Davies, 1992; Cahalan *et al.*, 1994b). However, the computational expense of these models has restricted these analyses to a limited set of cloud fields. The ICA is often used as a benchmark in radiation studies (e.g. Barker and Fu, 2000; Wu and Liang, 2005), but is too computationally expensive for operational use in a GCM. The ICA method is described in more detail in chapter 2.

The simplest efficient method for accounting for water content inhomogeneity involves scaling the cloud optical properties. The ‘scaling factor’ introduced by Cahalan *et al.* (1994a) is defined as the log-average (exponential of the mean of the logarithm) water content divided by the mean water content. Oreopoulos and Davies (1998b) suggested an alternative scaling factor that takes the value required for the albedo to match the ICA albedo, while Li *et al.* (2005) describes an empirically based parametrization for the scaling factor. Scaling requires negligible additional computational expense and can work reasonably well if the variance is small (Oreopoulos and Davies, 1998b); ECMWF used a global scaling factor of 0.7 for many years (Tiedtke, 1996). However, irrespective of which particular scaling factor is used, the magnitude will depend on: gridbox size (Pomroy and Illingworth, 2000); time of year, location and cloud phase (Oreopoulos and Cahalan, 2005); cloud fraction (Kogan *et al.*, 1995); cloud type (Bäumel *et al.*, 2004); solar zenith angle (Shonk and Hogan, 2008); and even the optical property that the scaling is based on (Szczap *et al.*, 2000).

The ICA calculation of albedo/transmittance can be represented as the integral over optical depth of the optical depth distribution times the plane-parallel albedo/transmittance. Barker (1996) showed that if the optical depth can be represented by a gamma distribution, then these integrals can be solved analytically, leading to new equations for solar albedo and transmittance that include the effect of subgrid-scale optical depth variability. This method can also be extended to the LW (Barker and Wielicki, 1997). However, it increases the computational cost of the radiation calculation by at least 25% (Barker and Fu, 2000), increases the complexity of the calculation, and also suffers from many of the same problems as the simple scaling factor.

More recently, Shonk and Hogan (2008) introduced the ‘Tripleclouds’ method. This works by splitting each layer of each GCM column into three regions: one clear-sky and two equally weighted cloudy regions. One of the cloudy regions is assigned to optically thinner cloud, the other represents the optically thicker cloud. Tripleclouds has been implemented and tested in the Met Office Unified Model (Shonk *et al.*, 2012).

The Monte Carlo Independent column approximation (McICA) (Pincus *et al.*, 2003) mimics the ICA calculation, but is noisier and more computationally efficient. The ICA requires a monochromatic calculation for every sub-column for each point in the integral over wavelength. In McICA, for each point in the integral over wavelength a single monochromatic calculation with a randomly chosen sub-column is performed. This reduces the cost of the radiative transfer calculation considerably, but introduces unbiased random errors, which can be reduced by performing more monochromatic calculations for a selection of wavelengths (e.g. Räisänen and Barker, 2004). However, unless this noise is quite large, it has been shown to have no significant impact on GCM climate simulations (e.g. Räisänen *et al.*, 2005, 2007, 2008; Barker *et al.*, 2008). An important additional advantage of both ICA and McICA is that the cloud representation is separated from the radiative transfer scheme, so making changes to the subgrid-scale cloud structure is easier. This is the reason for the adoption of McICA in the E-S scheme, as described in chapter 2.

1.4.2 HOW MUCH INHOMOGENEITY EXISTS?

As remarked in section 1.4.1 unresolved cloud water content variability has significant radiative impacts and the magnitude of these impacts depends on the magnitude of the unresolved variability. This section addresses the issue of how much subgrid variability exists.

While numerous observational studies of water content variability have been carried out (e.g. Smith and Del Genio, 2001; Rossow *et al.*, 2002), they use different inhomogeneity parameters and observations sources and the results are rather disparate. Shonk *et al.* (2010) reviewed many of these articles. For ease of comparison, the different inhomogeneity parameters were converted to fractional standard deviation (FSD); the standard deviation divided by the mean. Estimates of mean FSD ranged from 0.445 to 1.374. Moreover, while individual studies identified correlations

between FSD and other variables (as detailed below), there were no obvious relationships when the different studies were combined.

Both Barker *et al.* (1996) and Pincus *et al.* (1999) identified a relationship between cloud type and variability, with cumulus clouds showing more inhomogeneity than stratocumulus. Hogan and Illingworth (2003) found that variability increased as the domain size increased and that wind shear was negatively correlated with variability. Cahalan *et al.* (1994a) and Oreopoulos and Cahalan (2005) show conflicting results concerning the relationship between cloud fraction and variability; Cahalan *et al.* (1994a) found that variability increased with increasing cloud fraction, while Oreopoulos and Cahalan (2005) found that cloud fraction and variability were essentially independent, except close to cloud fractions of one, where the variability decreased very sharply.

While knowledge of the water content variability alone is sufficient for Tripleclouds and scaling factor calculations, a statistical distribution is required for McICA calculations. Many different distribution functions have been suggested for subgrid-scale inhomogeneity, including normal (Gollmer *et al.*, 1995), log-normal (Bony and Emanuel, 2001), beta (Tompkins, 2002) and gamma (Barker, 1996) distributions. Observational studies (e.g. Hogan and Illingworth, 2003; Lee *et al.*, 2010; de la Torre Juárez *et al.*, 2011) have generally found that the log-normal and gamma distributions provide the best matches to the observed distributions.

1.4.3 EFFECTS OF REPRESENTING INHOMOGENEITY

Outgoing LW radiation (OLR) is a concave function of optical depth (Fu *et al.*, 2000), so neglect of subgrid water content variability leads to an overestimate of the reduction in OLR by clouds (i.e. an underestimate of OLR). Similarly, in the SW, neglect of inhomogeneity leads to an overestimate of the CRE. Thus the net effect of adding a representation of variability will be a reduction in the CRE for a given water content.

For individual cloud scenes, instantaneous OLR errors due to neglecting subgrid-scale water content variability may be as large as 60 Wm^{-2} (Fu *et al.*, 2000), while instantaneous TOA SW errors may exceed 100 Wm^{-2} (Barker *et al.*, 1999). However, average errors for large numbers of realistic cloud scenes are smaller. Applying Tripleclouds to four months of ERA-40 cloud fields and employing a constant global value for the FSD, Shonk and Hogan (2010) found that

the magnitude of the water content homogeneity bias depended on the magnitude of the FSD. For an FSD of 0.57, the effect on TOA CREs was found to be 3.1 and -1.0 Wm^{-2} in the SW and LW respectively, while for an FSD of 0.93, the corresponding values were 12.1 and -4.1 Wm^{-2} . Barker and Räisänen (2005) performed ICA calculations on stochastically generated cloud fields initialized by data from a super-parametrized (Khairoutdinov and Randall, 2001) GCM. By perturbing the FSD of the generated cloud fields by small values and assuming that the radiative effect could be linearly extrapolated, they estimated that a 1.0 change in FSD would change SW and LW TOA fluxes by 8.75 and -3.86 Wm^{-2} respectively. Note that estimating the effect of a 1.0 change in FSD from the values in Shonk and Hogan (2010) results in a much larger estimate of this sensitivity (24.8 Wm^{-2} for SW fluxes and -8.6 Wm^{-2} for LW fluxes). Nevertheless, both studies suggest that the sensitivity of TOA fluxes to changes in the FSD is significant, which implies that better estimates of the magnitude of unresolved variability are required.

The effects of introducing the radiative effect of inhomogeneity in GCMs have generally been found to be consistent with the off-line calculations described above (i.e. CREs are reduced). Comparing a five year climate simulation with scaling of optical depth (by 0.7) to account for inhomogeneity to one with no scaling, Gu *et al.* (2003) found that OLR was increased by 4.6 Wm^{-2} and the reflected SW was reduced by around 12 Wm^{-2} . Using Tripleclouds, Shonk *et al.* (2012) identified a smaller effect (around 3 Wm^{-2} in both SW and LW TOA fluxes) in 20 year MetUM climate simulations and also showed changes in surface temperature and cloud fraction. GCM sensitivity to changes in the distribution of variability was considered by Gu and Liou (2006); they compared two five year climate simulations, one applying a global scaling factor to cirrus clouds, the other applying a geographically varying scaling factor based on ISCCP data. The non-uniform scaling factor was generally larger than the global value (i.e. inhomogeneity was smaller), so global mean CRE was increased in the experiment using the geographically varying scaling factor. Perhaps more significantly, there were also changes to the geographic distributions of cloud and precipitation.

Climate models are usually ‘tuned’ in order to get the correct global-mean TOA radiative fluxes. This means that the homogeneous clouds bias is often hidden by other compensating biases in the model and the direct effect of introducing inhomogeneity will be an increase in the magnitude of the TOA radiative flux bias.

1.5 CLOUD VERTICAL OVERLAP

Another ramification of the non-linear relationship between clouds and radiation is the sensitivity to the assumptions about vertical overlap of the subgrid cloud. For a pair of partially cloudy layers, the radiative fluxes and heating rates depend on the way that clouds in each layer are aligned vertically: the radiative effect of the cloud decreases as the area of overlapping cloud increases. Cloud overlap is also important for GCM estimates of surface precipitation; whether precipitation falls into cloudy or clear air affects accretion and evaporation rates. (Jakob and Klein, 1999).

There are three standard overlap assumptions, which in order of increasing total cloud cover are maximum, random and minimum overlap. These are illustrated by Figure 1.1. Maximum overlap can be physically justified by each layer containing part of the same cloud (i.e. a single cloud extending over multiple layers). Random overlap can be explained by different clouds being present in each layer, so that the cloud in each layer is independent. Minimum overlap is harder to justify based on meteorological processes, but could arise when the presence of one cloud inhibits the formation of another, for example turbulent mixing associated with shallow cumulus clouds inhibits the growth of deep convective clouds (e.g. Cheng and Xu, 2006). Note that the definition of random overlap is somewhat ambiguous; for random overlap in GCMs the areal fraction of overlapping cloud is generally equal to the product of the cloud fraction in each layer, as shown in the schematic. This is the overlap that would be observed if each cloud was divided horizontally into an infinite number of independent cloud cells, which were randomly overlapped with each other.

Up until relatively recently, GCM overlap assumptions were generally embedded in the radiative transfer solver, as described by Geleyn and Hollingsworth (1979). In this case, only the overlap between adjacent layers can be prescribed; the overlap between discontinuous layers is obliged to be random, while the overlap between contiguous but non-adjacent cloudy layers is only constrained by the overlap of the set of adjacent layers between them and is otherwise random. These overlap constraints do not apply to the ICA and McICA schemes (See section 1.4.1), which separate the assumptions concerning subgrid cloud from the radiative transfer solver, facilitating modifications to the overlap assumptions.

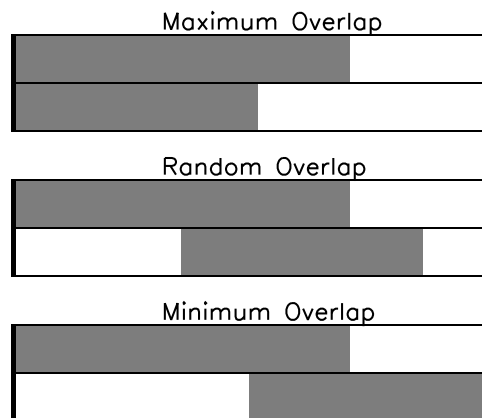


Figure 1.1 Illustration of the maximum, random and minimum overlap assumptions.

While this split between contiguous and discontinuous cloudy layers was originally motivated by the practicalities of calculating the transmission of fluxes between layers of a GCM, observations have confirmed that the overlap assumptions that are required for contiguous and discontinuous layers may indeed be different. Overlap parametrizations that treat contiguous and discontinuous cloud layers separately are often denoted by the overlap parametrization for each, separated by a hyphen, with contiguous overlap first (e.g. maximum-random means contiguous layers are maximally overlapped and discontinuous layers are randomly overlapped). This convention will be used in this thesis.

1.5.1 CONTIGUOUS CLOUDS

Up until relatively recently, most models used maximum overlap for contiguous clouds, as described by Geleyn and Hollingsworth (1979). This method was supported by the study of Tian and Curry (1989), which found that maximum overlap was more appropriate than either random or minimum overlap.

The development of cloud radars in the 1990s provided new datasets for studying cloud overlap; Hogan and Illingworth (2000) found that the average overlap for contiguous clouds was best represented by a linear combination of maximum and random overlap, with the overlap becoming increasingly random as the vertical distance between the layers increased. They suggested that

the ‘overlap parameter’, which controls the proportion of maximum and random overlap could be represented by an inverse exponential function of the vertical distance between the layers, with a ‘decorrelation length’ to control the rate at which the overlap parameter decreases with increasing distance.

Subsequent research (e.g. Mace and Benson-Troth, 2002; Mace *et al.*, 2009; Oreopoulos and Norris, 2011) has confirmed that the exponential overlap method suggested by Hogan and Illingworth (2000) is an excellent approximation for the average overlap between contiguous clouds. However, there remains considerable uncertainty concerning the most appropriate decorrelation length. Hogan and Illingworth (2000) found that decorrelation length varied with horizontal and vertical resolution, while Barker (2008a) found that it was linked to cloud fraction and horizontal resolution had little impact. Shonk *et al.* (2010) suggested a latitudinally dependent value ranging linearly from less than 0.5 km at the poles to around 3 km at the equator. On the other hand, there is a growing body of evidence showing that, at least from a global mean radiation budget perspective, GCMs are reasonably insensitive to the precise value of the decorrelation length (e.g. Barker, 2008b; Shonk and Hogan, 2010).

While the mean overlap for contiguous layers can be well approximated by exponential overlap, the distribution of overlap is less well studied. It is not clear how representative of individual cloud scenes the mean overlap is.

1.5.2 NON-CONTIGUOUS CLOUDS

GCMs generally assume that non-contiguous clouds are independent and overlap is random. Random overlap of non-contiguous clouds has been affirmed by several observational studies (e.g. Hogan and Illingworth, 2000). While some studies have concluded that certain cloud types are correlated and random overlap is not appropriate, these are studies that consider overlap in terms of frequency of co-occurrence of multiple discontinuous cloud layers within each observed domain (e.g. Chen *et al.*, 2000; Wang and Dessler, 2006). The overlap in question applies to very large domains and is not directly comparable to the subgrid overlap that is required by the radiation scheme; the equivalent model values also depend on the resolved cloud overlap as predicted by the cloud scheme.

As for contiguous clouds, previous observational studies have considered the mean overlap only; in order to add further insight on both contiguous and non-contiguous clouds, we intend to study the distribution of overlap parameters. Moreover, we shall consider the implications of using the mean overlap rather than the true overlap for atmospheric radiative transfer calculations.

1.5.3 EFFECTS OF CHANGING OVERLAP

For individual cloud scenes, the overlap assumption can have a very large impact on the radiative fluxes and heating rates (e.g. Barker *et al.* (1999) showed that changing the overlap assumption could change the TOA SW fluxes by more than 300 Wm^{-2}). The effect on global mean fluxes is smaller, due to the presence of overcast layers. For example, using year-long climate simulations, Morcrette and Jakob (2000) found that the difference between maximum-random and random overlap in terms of global mean TOA fluxes were 6.9 and 1.5 Wm^{-2} in the LW and SW respectively.

As acknowledged earlier, if exponential-random overlap is adopted, the sensitivity of the global mean radiation budget to the exact magnitude of the decorrelation length is smaller still. Barker (2008b) found that zonal-average CRE biases arising from the use of a global decorrelation length of 2km were at most around 10 and 5 Wm^{-2} in the SW and LW respectively, while root mean square errors were less than 30 and 12 Wm^{-2} . Shonk and Hogan (2010) estimated that the range of net CRE values resulting from the estimated uncertainty in their zonal mean decorrelation length parametrization was 0.5 Wm^{-2}

1.6 THIS THESIS

1.6.1 AIMS

The primary aim of this work is to improve understanding of cloud structure and the affect that unresolved cloud structure has on cloud-radiation interactions. In particular this work focuses on two radiatively important facets of cloud structure; cloud vertical overlap and subgrid-scale horizontal cloud water content variability.

The secondary aim of this thesis is to improve the representation of cloud in the Edwards-Slingo radiative transfer scheme that is used in the Met Office Unified model. This will give us more confidence in the model and potentially contribute towards improved weather forecasts and climate prediction.

1.6.2 OUTLINE

The following chapter, which has been published as Hill *et al.* (2011), concerns the use of McICA to represent the radiative effects of unresolved cloud structure in the MetUM, focusing on evaluation, reduction and impacts of the associated random errors. We introduce a new algorithm for choosing how cloudy sub-columns should be sampled by the radiation scheme in order to efficiently reduce noise. We consider how McICA noise affects an NWP simulation and compare surface temperature errors related to McICA noise to the errors arising from an incorrect treatment of subgrid cloud structure.

Chapter 3, published as Hill *et al.* (2012), employs a set of combined CloudSat and Moderate Resolution Imaging Spectroradiometer (MODIS) observations of ice water content to determine how much ice water content variability is unresolved by GCMs. The FSD of ice water content is found to increase with the horizontal scale over which it is calculated and also with the thickness of the layer. The connection to cloud fraction is more complicated; for small cloud fractions FSD increases as cloud fraction increases while FSD decreases sharply for overcast scenes. The derivation of a simple parametrization of ice water content variability including these relationships, suitable for use in GCMs, is detailed.

Chapter 4 concerns cloud vertical overlap. CloudSat radar and CALIPSO lidar observations are merged in order to produce a combined cloud mask. We investigate the mean overlap parameter and confirm that it is well predicted by the exponential-random overlap parametrization. We also consider the distribution of overlap parameters and show that the mean overlap parameters given by exponential-random overlap are rarely suitable for individual cloud scenes. We investigate the relationship between horizontal cloud structure and overlap and suggest some changes to the representation of cloud overlap in models in order to better capture the observed distribution of overlap. The impact of these changes on total cloud cover and estimates of OLR is described.

Chapter 5 describes the impact of changes to subgrid-scale cloud structure on 10-year climate simulations, focusing in particular on the effect of the FSD parametrization derived in chapter 3. The climatology of the FSD that arises from applying the parametrization in the model is discussed. Comparing a climate simulation using the FSD parametrization to one using the same mean FSD applied globally, we show that allowing the FSD to vary according to the parametrization reduces the global mean CREs.

Finally, chapter 6 contains a summary of the thesis, followed an outline of potential future work.

CHAPTER 2:

REDUCING NOISE ASSOCIATED WITH

McICA FOR WEATHER FORECASTING

MODELS

The following chapter has been published as Hill *et al.* (2011).

2.1 INTRODUCTION

The importance of cloud to the distribution of radiative heating rates has long been recognised (e.g. Liou, 1986), as has the importance of representing subgrid-scale cloud inhomogeneity (e.g. Cahalan *et al.*, 1994a). However, the radiative transfer schemes used in many general circulation models ignore subgrid-scale cloud water content variability, and assume that clouds are vertically overlapped according to the maximum-random approximation (e.g. Geleyn and Hollingsworth, 1979). Barker *et al.* (1999) showed that these assumptions lead to biases in the calculated fluxes and heating rates, both individually and when combined.

The Monte Carlo Independent Column Approximation (*McICA*), described by Pincus *et al.* (2003), is a method for representing cloud inhomogeneity in radiative transfer schemes. It approximates the accurate but costly full independent column approximation (*ICA*) calculation (e.g. Barker *et al.*, 1999), at considerably less computational expense. For the integral over wavelength, at each quadrature point, instead of calculating the monochromatic flux for every sub-column, the monochromatic flux for one or more randomly chosen sub-columns is calculated. For further details, see section 2.2.

McICA has two major advantages compared with the alternative methods for representing

cloud inhomogeneity in GCMs, such as the use of a scaling factor (e.g. Cahalan *et al.*, 1994a) or ‘Tripleclouds’ (e.g. Shonk and Hogan, 2008). Firstly, it is unbiased with respect to the full ICA calculation. Secondly and perhaps more importantly, it removes the cloud structure representation from the radiative transfer code and thus allows for a more flexible cloud representation. On the other hand it introduces conditional random errors, which depend on the choice of sub-columns mapped to each quadrature point. The amount and effect of this noise has been the subject of several papers. However, such papers have generally tended to focus on its impacts in climate models.

Pincus *et al.* (2003) performed a number of tests on cloud fields from a cloud-resolving model (CRM). They calculated a standard deviation of McICA errors for short-wave (SW) surface flux of 105 Wm^{-2} (approximately 10% of the incident TOA radiation). The effect of this noise on a seasonal forecast model was estimated by randomly perturbing radiative fluxes and heating rates. They found no statistically significant differences to their control.

Räisänen *et al.* (2005) and Räisänen *et al.* (2007) investigated the effect of McICA noise on the National Center for Atmospheric Research (NCAR) Community Atmosphere Model (CAM) and European Centre Hamburg Model 5 (ECHAM5) climate models respectively, using a low-noise version of McICA as the reference. In both models they found that their noisiest implementations of McICA led to a significant reduction in low cloud fractions. They were able to remove this effect by reducing the level of noise.

More recently, Barker *et al.* (2008) investigated the effect of McICA noise on several global models. Again using a low-noise version of McICA as the reference, they ran 14 day simulations. They found that some of their models responded significantly to the noisiest tests, but no models displayed significant impacts when noise was reduced.

While the effect of McICA noise on climate models has been quite extensively studied, its effect on numerical weather prediction (NWP) models, particularly where the time and spatial scales of interest are smaller, is not so well documented. McICA has been tested in the European Centre for Medium-Range Weather Forecasts (ECMWF) integrated forecast system (Morcrette *et al.*, 2008), and as in the climate simulations, the related noise was not found to be detrimental to results. However, the radiation scheme employed at ECMWF has many more quadrature points

than most other forecast models and as a result the magnitude of McICA noise in the ECMWF model is significantly smaller.

As McICA noise is generally thought to be of little consequence, only a single article has been published regarding methods for reducing noise. Räisänen and Barker (2004) suggested two methods for minimising McICA noise. Combining these methods they found that they could reduce the standard deviation of McICA noise by approximately a factor of three, while increasing the number of monochromatic calculations required by 50%.

This chapter investigates the effect of McICA noise on the MetUM. In section 2.2 we consider the McICA scheme in more detail, discuss its implementation in the MetUM and describe the cloud generator that provides the subgrid cloud profiles required. Section 2.3 considers the magnitude of the noise associated with McICA, introduces techniques for efficiently minimising this noise and compares these techniques to a previous method. In section 2.4 we consider the effect of McICA noise on a MetUM NWP simulation, with regards to 1.5 metre temperature in particular. Finally, conclusions are presented in section 2.5.

2.2 THE MCICA METHOD AND ITS IMPLEMENTATION

2.2.1 THE MCICA METHOD

At its core, the McICA method is an efficient mechanism for approximating the full ICA calculation. As such, we shall first describe the full ICA calculation in detail and then go on to describe how the McICA method relates to it.

The full ICA calculation consists of splitting each GCM column into a number of sub-columns, each of which is either overcast or cloud-free. The distribution of water content within the cloud can be represented by allocating different water content values to each sub-column. Assuming the flux in each sub-column is independent of the flux in the other sub-columns, i.e using the independent column approximation, the radiative transfer calculation is performed for each sub-column individually. The fluxes for the entire profile are then determined as the mean of the sub-column fluxes. Considering a profile divided into N sub-columns and a radiative transfer

scheme with K quadrature points to approximate the integral over wavelength, the full ICA flux, \bar{F} , is given by

$$\bar{F} = \frac{1}{N} \sum_{i=1}^N \sum_{j=1}^K f_{i,j} \quad (2.1)$$

where $f_{i,j}$ denotes the flux calculated for the quadrature point j and the sub-column i . This method is far too computationally expensive for practical use in GCMs, due to the double sum over quadrature points and sub-columns (in the equation above, NK monochromatic radiative transfer calculations are required, as opposed to K monochromatic calculations for the corresponding plane-parallel homogeneous calculation). However, it is often applied as a benchmark when evaluating other methods of treating horizontal inhomogeneity.

In the McICA scheme, each GCM column is again divided into sub-columns. However, rather than calculating fluxes for every combination of quadrature points and sub-columns, the flux for each quadrature point is calculated using one or more randomly chosen sub-columns. Thus the McICA flux, F , is given by:

$$F = \sum_{j=1}^K \sum_{i=1}^{n(j)} \frac{f_{rand(i,j),j}}{n(j)} \quad (2.2)$$

where $n(j)$ denotes the number of randomly chosen sub-columns for the quadrature point j and $f_{rand(i,j),j}$ denotes the flux calculated for the quadrature point j and a randomly chosen sub-column, $rand(i,j)$. If the distribution of sub-columns amongst the quadrature points is truly random, then McICA fluxes are unbiased with respect to the full ICA fluxes. However conditional random errors are introduced. If the sub-columns are sampled without replacement, then at the limit of $n(j)$ equals N for all j , we have exactly the full ICA calculation.

2.2.2 IMPLEMENTATION IN THE MET OFFICE UNIFIED MODEL

The Edwards-Slingo radiative transfer code (e.g. Edwards and Slingo, 1996) employed in the MetUM currently splits both the SW and long-wave (LW) spectra into a number of distinct bands. Within each band, extinction due to cloud condensate is treated as a ‘grey’ process. The correlated k -distribution method (e.g. Fu and Liou, 1992) is employed to represent gaseous absorption within the bands. This consists of reducing the number of quadrature points representing the integral over wavelength by binning those wavelengths with similar absorption coefficients (hereafter referred to as k -terms). Overlap of absorption is accounted for by equivalent extinction (Edwards,

1996) where full calculations are only performed for the k -terms representing the ‘major’ gas in each band. External ‘spectral files’ are used to provide information on the decomposition of the spectrum into bands and k -terms, along with the optical properties of gases, aerosols and cloud condensate.

The homogeneous plane-parallel method currently in operation in Edwards-Slingo allows for fractionally cloudy layers, by splitting each layer into horizontally homogeneous regions (e.g. Shonk and Hogan, 2008). Thus, assuming we have two regions in each layer (i.e. cloudy and clear) we must solve for a clear and cloudy flux in each layer in order to obtain total up and downwelling fluxes.

The McICA scheme requires information about subgrid cloud. We use a stochastic cloud generator that implements the approach described by Räisänen *et al.* (2004). This generates 100 sub-columns, which may or may not contain cloud, once per radiative time-step, so the same set of sub-columns can be sampled in both the SW and the LW. Moreover it is called independently of the radiation scheme. Hence the cloud sub-columns are available for use in other parametrisation schemes, such as the precipitation scheme, if required.

We have extended the generator to include a representation of the exponential-random overlap approximation suggested by Hogan and Illingworth (2000), in addition to the separate exponential and random overlap parametrisations already available. Here contiguous clouds are overlapped according to the exponential parametrisation while non-contiguous clouds are randomly overlapped. In addition, we redefined the decorrelation length scale of Hogan and Illingworth (2000) in terms of pressure, as a pragmatic measure to more closely match the vertical coordinates used within the radiation scheme.

For our implementation of McICA, we allocate a distinct cloud sub-column to each k -term. Thus cloud optical properties must be calculated once per k -term rather than once per band as in the plane-parallel case. Moreover, each sub-column is either overcast or clear, so we only need to solve for a single set of fluxes, which is significantly less computationally expensive.

The computational cost of the McICA method depends on the chosen numbers for n in equation 2.2. Clearly, as the values of n increase, more monochromatic calculations are required, so the cost of the code increases. Consider a McICA calculation which requires the same number

of monochromatic calculations as the plane-parallel calculation (so in equation (2.2), $n(j) = 1$ for all j). As we have the same number of monochromatic calculations, but only require a homogeneous solver, calculating fluxes once the optical properties have been calculated is computationally cheaper. However, calculating the optical properties is more expensive, as the cloud contributions must be calculated once per k -term rather than once per band. Moreover we must account for the further cost of generating the cloud sub-columns. Thus the total cost of such a McICA calculation is comparable to that of the plane-parallel calculation.

2.3 EVALUATION AND OPTIMISATION OF NOISE

In order to study whether noise has an impact, a mechanism for controlling the level of noise is necessary. Thus in this section we consider methods for optimally reducing the magnitude of McICA noise.

2.3.1 METHODS FOR REDUCING NOISE

Techniques for efficiently reducing McICA noise were first considered by Räisänen and Barker (2004). Two methods were introduced: optimising the spatial sampling and optimising the spectral sampling.

The method of optimising the spatial sampling consists of splitting the flux calculation into clear and cloudy parts and restricting the random sampling of sub-columns to the cloudy part of the calculation. Thus equation (2.2) becomes:

$$F = (1 - C_{tot}) \sum_{j=1}^K f_j^{clr} + C_{tot} \sum_{j=1}^K \sum_{i=1}^{n(j)} \frac{f_{rand(i,j),j}^{cld}}{n(j)} \quad (2.3)$$

where C_{tot} is the total cloud cover in the profile, f_j^{clr} is the clear sky flux calculated for the j -th k -term and $f_{rand(i,j),j}^{cld}$ is the flux calculated for the j -th k -term and a randomly chosen cloudy sub-column. Clear-sky fluxes are often determined for diagnostic purposes, in which case this optimal spatial sampling is no more expensive than the basic calculation as given by equation (2.2).

The method of optimising the spectral sampling is based on the fact that the various k -terms in a spectral file respond differently to changes in cloud (e.g. Manners *et al.*, 2009). The idea is to sample more cloudy sub-columns with the k -terms which contribute most to the radiative effects of cloud. Thus in equation 2.3, higher values of n are used for the k -terms which are more responsive to cloud. Hence a method is required to choose how many sub-columns each k -term should sample. Note that as described in section 2.2.2, in the MetUM, cloud sub-columns are generated independently of the radiative transfer scheme. Thus, we are taking additional samples from an existing pool of sub-columns.

We developed a simple algorithm that can be run once offline to choose how many sub-columns each k -term should sample. The aim of our algorithm is to identify those k -terms which contribute most to the changes in fluxes that occur for a change in cloud water content. Several factors contribute to the magnitude of this change in flux: the weight of the k -term, which represents the proportion of the total flux corresponding to the k -term, the atmospheric clear-sky transmission, and the difference in atmospheric transmission for the two different cloud water contents. The importance of the k -term increases as the magnitude of each of these factors increases. As the weight increases, the proportion of the total flux increases. Similarly, as the clear-sky transmission increases, there is less clear-sky extinction and a greater proportion of the flux is available to be extinguished by the cloud. A larger difference in cloud transmission corresponds to greater sensitivity to the actual value of the cloud condensate. Thus the following equation gives the relative ‘importance’ ι of each k -term:

$$\iota(j) = \frac{w(j) \times tg(j) \times (tc_{thin}(j) - tc_{thick}(j))}{n(j)} \quad (2.4)$$

where, $n(j)$ is the number of sub-columns sampled by the j -th k -term, $w(j)$ is the weight of the k -term, given by equation (2.5), $tg(j)$ is the atmospheric gaseous transmission for that k -term, calculated as in equation (2.6), $tc_{thin}(j)$ is the total atmospheric transmission value for optically thin cloud, as given by equation (2.7) and $tc_{thick}(j)$ is the total atmospheric transmission value for optically thick cloud, calculated as in equation (2.8).

$$w(j) = w_b(j) \times w_f(j) \quad (2.5)$$

$$tg(j) = e^{-(k_{esft}(j) \times u_g)} \quad (2.6)$$

$$tc_{thin}(j) = e^{-(\epsilon(j) \times u_1)} \quad (2.7)$$

$$tc_{thick} = e^{-(\epsilon(j) \times u_2)} \quad (2.8)$$

In equations (2.5) to (2.8):

- $w_b(j)$ is the weight of the k -term as a fraction of the band.
- $w_f(j)$ is the weight of the band as a fraction of the flux, calculated using the solar spectrum in the SW and a Planck function in the LW.
- $k_{esft}(j)$ is the absorption coefficient for the gas for the k -term.
- u_g is the integrated column amount of the gas.
- $\epsilon(j)$ is either the total extinction coefficient of the cloudy component or the absorption coefficient of the cloudy component, depending on whether the aim is to minimise surface flux or heating rate errors.
- u_1 is the integrated column amount of condensate for an optically thin cloud, 0.002 kgm^{-2} .
- u_2 is the integrated column amount of condensate for an optically thick cloud, 0.2 kgm^{-2} .

We include three gases in this calculation: water vapour, carbon dioxide and ozone, with integrated column amounts of 25 kgm^{-2} , 5 kgm^{-2} and 0.008 kgm^{-2} respectively. Each k -term represents absorption by one of these gases. The particular choices of condensate values above are rather arbitrary, but allow us to estimate the change in transmission due to changes in cloud thickness, as opposed to whether or not cloud is present. This prevents us from wasting samples on k -terms which respond strongly to cloud but quickly become saturated.

Initially, $n(j)$ equals 1, for all k -terms. The algorithm consists of the following steps:

- Calculate the values of $\iota(j)$ for all k -terms.
- Allocate an additional sample to the k -term with the largest value of ι .
- Add 1 to the value of $n(j)$ for the k -term which has been allocated an additional sample.
- If there are further sub-column samples to allocate, go back to the first step.

By assigning each additional sample to the most ‘important’ k -term, rather than the k -term which will have its importance reduced most, we minimise the individual importance of the k -terms rather than the sum of their importances. Minimising the individual importance results in more samples being assigned to fewer k -terms. Moreover, results showed that this leads to lower heating rate errors than when the sum is minimised.

As mentioned above, we suggest that $\epsilon(j)$ is defined as the total extinction coefficient of the cloudy component if one wishes to minimise flux errors and the absorption coefficient if one wishes to minimise heating rate errors. In the SW, both heating rates and the surface flux are significant, so we assigned sub-columns to minimise heating rates and fluxes alternately. In the LW, there is far more absorption than scattering, so we found that we got the same values for N irrespective of whether we used total cloud extinction or absorption.

Räisänen and Barker (2004) use an alternative method to allocate sub-columns to k -terms. This algorithm consists of calculating the global mean cloud radiative effect (CRE) for each k -term, either in terms of surface flux or heating rates. Then, further sub-column samples are allocated one-by-one to the k -term whose CRE is reduced most by allocating it an additional sub-column. We compare the two algorithms in the case study described in the following section.

2.3.2 TEST SET-UP AND RESULTS

The magnitude of noise associated with the McICA method was evaluated using the offline version of the Edwards-Slingo code, together with the spectral files which are used for both the HadGEM climate model and the global forecast model. The SW file contains 6 spectral bands and 20 k -terms for the major gases, while the LW file contains 9 spectral bands with a total of 33 k -terms for the major gases.

We shall discuss heating rate and SW surface flux errors for two different versions of McICA. In the single sampling version of McICA, optimal spatial sampling is applied, but no further additional cloud sub-columns are used. In the optimal version of McICA both optimal spatial and optimal spectral sampling are applied. Here we distribute 16 additional sub-columns in the SW and 12 in the LW using the algorithm outlined above (the effect of changing these numbers is discussed later in the chapter).

As mentioned in the previous section, the choices of gas and cloud amounts used in the algorithm were somewhat arbitrary. In the SW, for this particular spectral file, the algorithm is rather insensitive to the particular integrated column amounts of gas used; doubling or halving the amount of any of the gases has no effect. The algorithm is more sensitive to the cloud amounts, which of course are more variable. Nevertheless, modifying either of the cloud amounts by a factor of 10 only changes the distribution of at most three (out of 16) sub-columns. In contrast, in the LW, the algorithm is more sensitive to the gas amounts than the cloud amounts, but is relatively insensitive to both the gas and cloud amounts and the temperature from which the Planckian is calculated. While the algorithm showed little sensitivity to the particular values used for the temperature, gas and cloud amounts for the particular spectral files tested, it should be noted that this may not be the case for significantly different spectral decompositions.

The test cases were nine 100 column strips taken from various cloud resolving model (*CRM*) simulations. Properties of these cases are given in Table 2.1. Each of these strips is considered to be representative of a single GCM gridbox, divided into 100 sub-columns. For each case, the full ICA calculation was applied to obtain benchmark fluxes and heating rates. For each of the versions of McICA, for each CRM case, 1000 different McICA calculations were performed, with a different random assignment of sub-columns to k -terms for each calculation. For each of the 1000 versions of McICA, differences relative to the full ICA calculation were determined. The absolute values of these errors were then averaged, resulting in mean absolute heating rate and SW surface flux errors for each cloud case.

In order to put the degree of noise into context, we also used mean water content and cloud fraction profiles from each of the CRM fields to calculate fluxes using the homogeneous plane-parallel maximum-random overlap treatment of cloud, which we shall hereafter refer to as PP-MRO. It is important to remember that the McICA values below represent the expected magnitude

Case	Description of CRM simulation	Total cloud fraction	Layers	Fractional standard deviation of integrated total water content
A	extensive stratocumulus	1.0	127	0.166
B	extensive stratocumulus	1.0	127	0.249
C	extensive stratocumulus	1.0	127	0.560
D	convection over west Pacific	1.0	52	0.834
E	convection over west Pacific	1.0	52	0.834
F	convection over west Pacific	0.16	52	1.066
G	convection over Amazon	0.74	167	1.352
H	convection over Amazon	0.47	167	1.531
I	convection over Amazon	0.34	167	1.072

Table 2.1 Properties of the CRM cloud fields on which methods for reducing McICA noise are tested.

of an unbiased error. On the other hand, the PP-MRO errors we compare them to are biases, due to the combination of two biased assumptions: maximum-random overlap of plane-parallel cloud.

Figure 2.1 shows the mean value of the SW downwelling surface flux absolute errors for each of the CRM cloud fields. Note that although the magnitude of the noise varies significantly from case to case, the optimal method is always less noisy than the single-sampling method. Furthermore, the range of values for the optimal McICA experiment is significantly less than that of the PP-MRO experiment. It should be noted that the PP-MRO errors depend on the particular combination of the maximum-random and plane-parallel errors. The McICA errors on the other hand depend on the cloud water content fractional standard deviation and the number of cloudy sub-columns available to sample.

Table 2.2 shows the mean across all cloud cases for the SW surface flux errors shown in Figure 2.1. Also shown are the equivalent SW, LW and net heating rate errors. These mean absolute heating rate errors were calculated as follows. For each cloud case, the absolute heating rate error for each of the rows between the cloud top and the cloud base was diagnosed. These absolute heating rate errors were then weighted by the normalised mass of the layer. Finally, the mean of these weighted absolute heating rate errors were calculated.

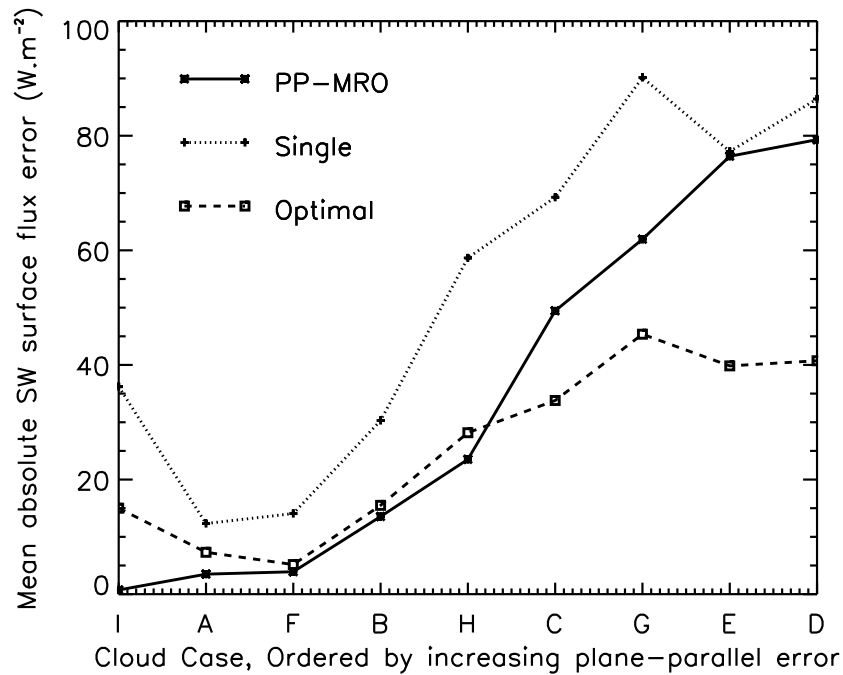


Figure 2.1 Mean SW surface down-welling flux absolute error. Each point represents a different cloud case. The solid, dotted and dashed lines correspond to the PP-MRO, single sampling and optimal results respectively.

Note that unlike for the SW surface flux errors, both SW and LW (and consequently net) mean absolute weighted heating rate errors are smaller for the PP-MRO experiment than either of the McICA experiments. This is because the surface fluxes depend on the water content values in the entire column. Thus, assuming that the distributions of water content in distinct layers are not completely correlated, there is some cancellation of water content sampling errors within each sub-column. The heating rates for each layer depend only on the change in flux for that layer and thus in their case no such cancellation of errors occurs.

We repeated the experiment described above using the alternative algorithm suggested by Räisänen and Barker (2004), tuned using the mean cloud radiative effect for each k -term from the CRM cases. The results are included in Table 2.2. As we used the same CRM cases on which we test the algorithm to tune the algorithm, the magnitude of the errors is probably somewhat underestimated. Nevertheless, the results are not significantly different to those obtained using

Code Version	Mean Error			
	down-welling SW surface flux (Wm^{-2})	SW heating rates (Kday^{-1})	LW heating rates (Kday^{-1})	Net heating rates (Kday^{-1})
PP-MRO	35	0.3	1.0	0.9
Single sampling	53	1.2	2.6	3.0
Optimal sampling	25	0.6	1.2	1.4
Raisanen and Barker	24	0.6	1.1	1.3

Table 2.2 Mean absolute surface flux and heating rate errors for each of the methods of representing clouds.

the simpler and quicker ‘importance’ algorithm.

For the initial experiments we have used an arbitrary number of additional sub-columns for optimal sampling (16 SW and 12 LW). Thus we performed further experiments to investigate how the magnitude of the noise depends on the number of additional sub-columns used. These experiments consisted of repeating the tests described above, with different numbers of additional sub-columns, assigned using the ‘importance’ algorithm. Once we had derived mean absolute errors for each cloud case, we then averaged these values to get a single value for each number of sub-columns. Figures 2.2 and 2.3 show the result of increasing the number of additional sub-columns for heating rates and SW surface fluxes respectively. The magnitude of the noise decreases sharply with the first few additional sub-columns and less sharply as further sub-columns are added. The number of additional sub-columns applied in an operational model will depend on the accuracy and cost constraints of that particular model. Also shown in 2.3 is the corresponding error calculated when two and three sub-columns are designated to each k -term. This line shows how the error would decrease if the number of sub-columns sampled by each k -term was chosen randomly.

2.3.3 COMBINING SW AND LW ERRORS

Generally, individual SW and LW heating rates are significant only in the context of their contribution to the net heating rates. Comparing the net heating rates in Table 2.2 we see that for the

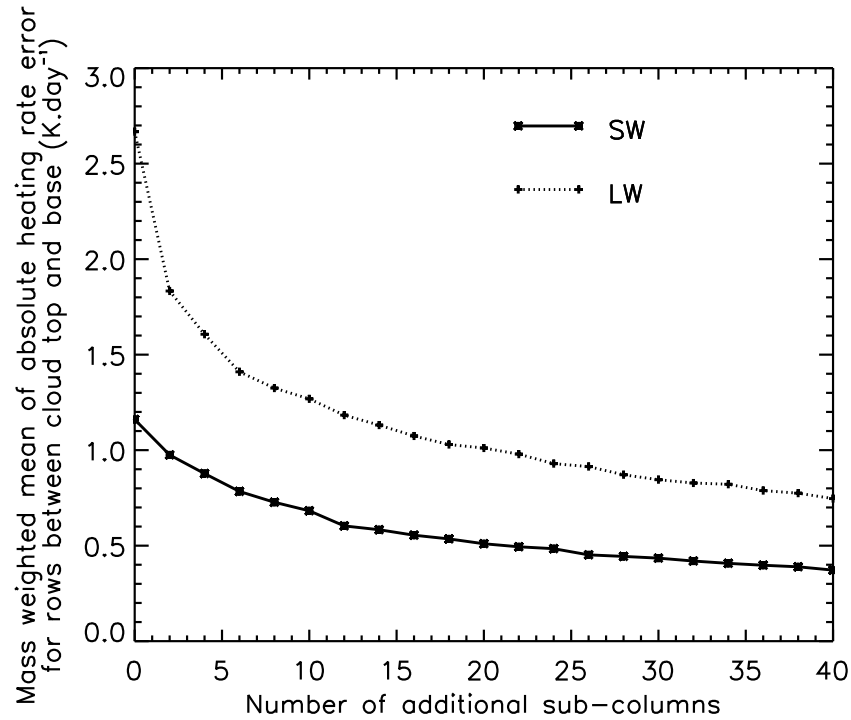


Figure 2.2 Total mass-weighted heating rate absolute errors, averaged across all CRM cases as in table 2.2, compared to the number of additional sub-columns used. The solid line shows SW values, while the dotted line shows LW values.

McICA experiments the mean absolute weighted net heating rate error is larger than either the SW or LW values, which is not the case for PP-MRO. This result can be explained as follows. As a general rule, clouds have a warming effect in the SW and a cooling effect in the LW. Thus in both the full ICA and plane-parallel methods, the net cloud heating is smaller than either the SW or LW components. In particular, this leads to a cancellation of errors in the plane-parallel run. In the McICA experiments described in the previous section, the sampling of sub-columns in the SW is independent of the sampling in the LW. Thus it is perfectly feasible for the dominant k -terms in the SW to be randomly assigned sub-columns which are relatively optically thin, while the dominant k -terms in the LW are assigned relatively optically thick sub-columns (or vice versa). In this case, the errors are in the same direction, and the net (SW+LW) error is larger than either of the constituent SW and LW errors.

This combination of errors of the same sign increases the magnitude of the mean errors and

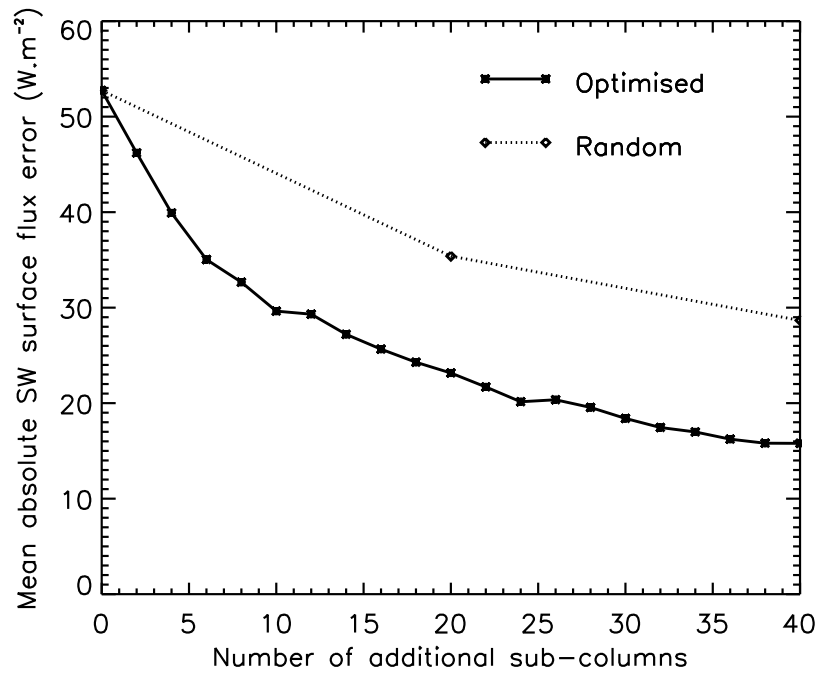


Figure 2.3 As Figure 2.2, but shows the dependence of SW surface flux errors on the number of additional sub-columns used. The solid line shows the error for our optimal sampling, while the dotted line shows the error when the sub-columns are spread evenly among the k -terms.

can lead to very large deviations. Table 2.3 shows the percentage of errors exceeding a given threshold, calculated from the cloudy layers in every case. In a GCM simulation, calculating a heating rate with large errors in the same direction on successive time-steps is unlikely. However, due to the long time-steps generally utilised in radiation schemes, errors persist for long enough to lead to quite a large erroneous temperature change. For example in the HadGEM climate model, which has radiation time-steps of three hours, a radiative heating error of 30 Kday^{-1} would lead to erroneous heating of almost 4 K.

In order to reduce the mean net heating rate errors and the likelihood of very large errors occurring, we introduced an extension to the method of distributing sub-columns to k -terms. For the single sampling case, we rank the k -terms in order of 'importance' separately for the LW and SW. We then assign the same cloud sub-column to LW and SW k -terms of the same rank. This ensures the dominant k -term calculations in both the SW and LW are done for the same cloud.

Code Version	Percentage of Errors		
	Exceeding... (Kday ⁻¹)		
	10	20	30
PP-MRO	2.30	0.00	0.00
Single sampling	8.01	3.18	1.31
Single + reordering	7.43	2.71	1.00
Optimal sampling	1.82	0.17	0.01
Optimal + reordering	1.38	0.08	0.00

Table 2.3 The percentage of mass-weighted heating rate errors exceeding the given magnitude, calculated for layers between cloud top and base, in every simulation.

When the list of either SW or LW k -terms is exhausted some k -terms will remain unmatched, but these are the least important and will have the smallest effect on the total error. For the optimal sampling case the ranking will include a number of terms of equal importance for each k -term, but otherwise the assignment of sub-columns proceeds as for the single sampling case.

The rearrangement of the sub-columns has no effect on the magnitude of the noise for the individual SW and LW calculations, but reduces the magnitude of the noise for the net (SW+LW) heating rates for each CRM case as shown in Figure 2.4. For comparison to Table 2.2, the mean net absolute heating rate error across all cases is reduced to 2.8 K for the single sampling version of McICA and 1.2 K for the optimal sampling version of McICA. These reductions in mean net heating rate errors are significant. Moreover the rearrangement comes at no additional computational cost and can be used in conjunction with any method for reducing noise that involves estimating the importance of the k -terms. The rearrangement also reduces errors in total net surface and TOA fluxes.

Some of the reduction in the total error shown in Figure 2.4 is simply due to the fact that the same set of sub-columns is used in both the SW and the LW rather than the actual matching of terms of equal rank. Further experiments were conducted to separate these effects. For the single sampling experiments, virtually all of the reduction in error was due to the reordering, while for the optimal experiment, most of the reduction in error was due to sampling the same set of sub-columns in both regions. This is because the distribution of ‘importance’ amongst the

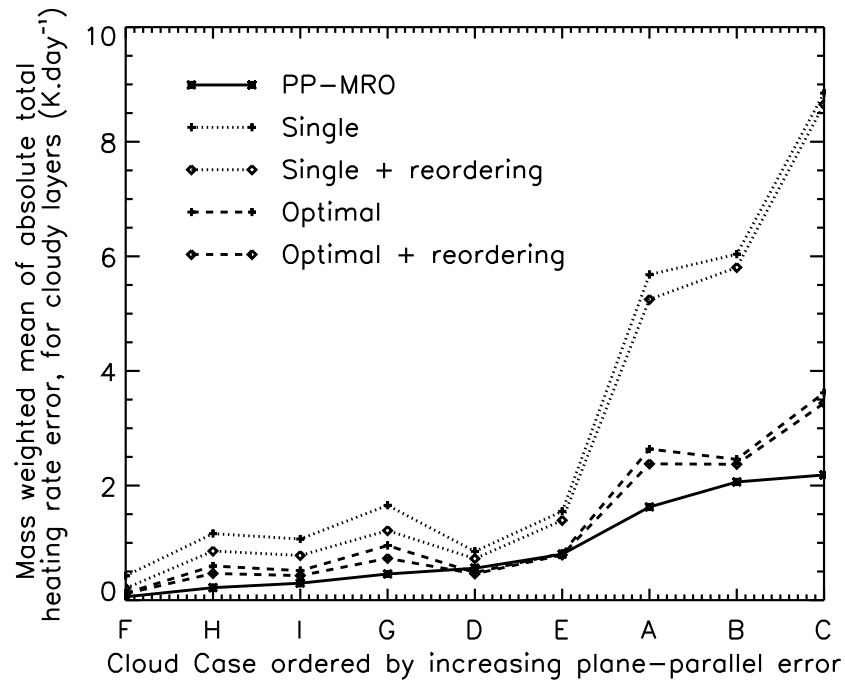


Figure 2.4 Mean total mass-weighted heating rate absolute errors for each of the cloud cases. The solid, dotted and dashed lines correspond to the plane-parallel, single sampling and optimal results respectively, while lines with ‘+’ symbols denote results without the rearrangement and lines with ‘◊’ symbols denote results where sub-columns have been rearranged to minimise errors.

sub-columns is much smoother by design in the optimal sampling experiments and matching the terms in exact rank order is less important.

2.4 THE EFFECT OF McICA NOISE ON AN NWP MODEL

In this section we study the effect of McICA noise on a global version of the MetUM. We compare the errors due to noise with those due to the combination of the plane-parallel and maximum-random overlap assumptions.

2.4.1 MODEL SET-UP

The case study adopted for test purposes is a five day simulation, beginning on 16th December 2002 at 0900 GMT, as used by Manners *et al.* (2009). The model considered was a reduced resolution configuration of the operational global forecast model. This model has 50 vertical levels of varying resolution and is divided into 96 longitudes and 73 latitudes. The model dynamics use a semi-implicit time-integration scheme with a time-step of 15 minutes. The radiation scheme is called every 12 time-steps (i.e. every three hours), as for the full operational resolution. The spectral files are the same as those used in the offline calculations described in section 2.3.2. A fixed distribution of sea surface temperatures was used.

Although the resolution of the test model is significantly lower than that of operational NWP models, it was necessary to run at this resolution in order to perform the benchmark ICA calculations described below. Increasing resolution will mean that more water content variance is resolved, and noise will be injected at smaller scales. However, cloud water content variance remains significant at higher resolutions (e.g. Hogan and Illingworth, 2003) and gridbox scale results remain important for forecasting applications even at resolutions of 25 km. Thus we would expect our results to remain applicable at higher resolutions.

Benchmark fluxes and heating rates were derived by fully sampling the generated cloud with every k -term (i.e using the full ICA). Three different versions of McICA were tested: the noisiest using the single sampling method, a second using the single sampling method together with the reordering of sub-columns, and the third using the optimal method for sampling sub-columns together with reordering. As in the offline experiments, a PP-MRO simulation was performed which uses the plane-parallel and maximum-random overlap approximations.

For the ICA and McICA experiments, subgrid-scale cloud profiles were generated using the generator described in section 2.2. The exponential-random overlap method was used, with a global cloud decorrelation scale of 100 hPa and a condensate decorrelation scale of 50 hPa. In-cloud water condensate followed a gamma distribution, with a fractional standard deviation of 0.75. The sensitivity of the results to these parameters is discussed below.

Although exponential-random overlap can be represented without using the McICA scheme,

the combination of the exponential-random overlap and plane-parallel assumptions leads to larger errors than the combination of the maximum-random overlap and plane-parallel assumptions (e.g. Shonk and Hogan, 2010). This is because the maximum-random overlap and plane-parallel approximations have biases in opposite directions. Thus when combined, there is some cancellation of errors. For this reason, we compare the exponential-random McICA results to maximum-random plane-parallel results.

2.4.2 RESULTS

The following results mainly concern the model 1.5 metre temperature. This near-surface temperature is an important forecast variable. Moreover, we expect it to respond strongly to radiative changes, due to its dependence on surface SW fluxes. Precipitation was also considered, but was found to be insensitive to the radiative changes.

For each experiment a set of instantaneous absolute 1.5m temperature errors, relative to the full ICA value, was calculated every three hours. The mean of these absolute errors was then calculated and is shown in Figure 2.5. As the simulation used a fixed sea surface temperature, we excluded sea points from the calculation of the mean errors (i.e. only land and sea ice points are included).

At the start of the forecast, the lowest errors are obtained using the optimal McICA experiment, with slightly larger errors for PP-MRO, and larger errors again for the two single sampling experiments. The relative magnitudes of these errors are similar to the relative magnitudes of the SW surface flux absolute errors shown in Figure 2.1 which, given the dependence of near-surface temperatures on the SW surface flux, may be expected. This shows that our results for the CRM cases hold globally.

As the forecast progresses, the errors grow due to radiative errors propagating into the rest of the model, which cause the experiments to diverge. While the errors in each of the McICA experiments appear to grow at roughly the same rate, the mean absolute error for the PP-MRO run grows more quickly. Thus after 48 hours the PP-MRO errors are as large as the single sampling errors and by the fifth day of the experiment, the PP-MRO errors are larger than any of the McICA errors. This can be explained by the fact that the PP-MRO errors are biased.

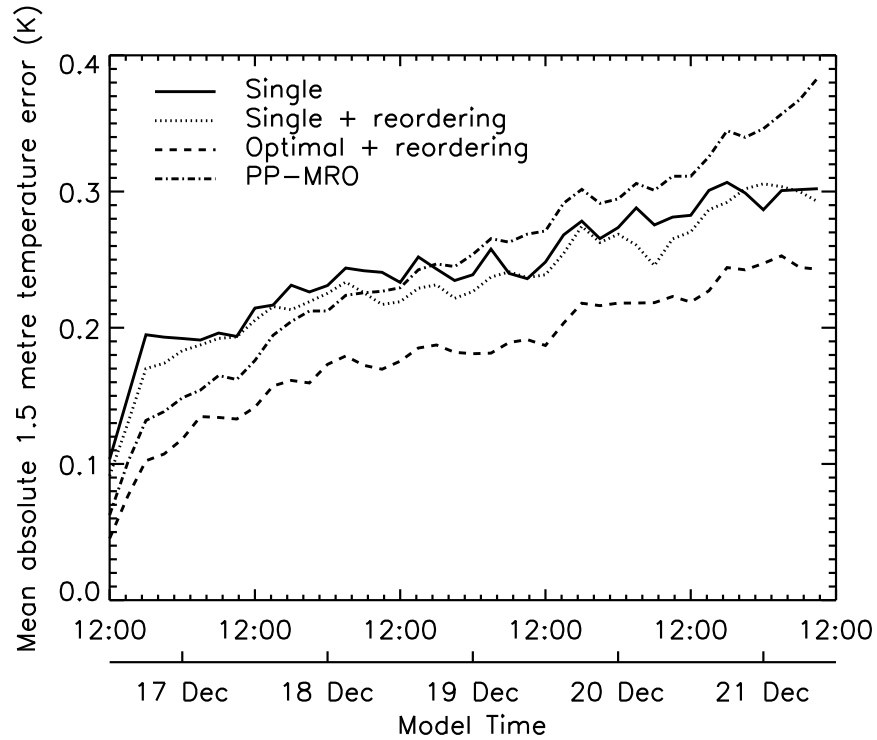


Figure 2.5 Mean 1.5m temperature absolute error. The solid, dotted, dot-dash and dashed lines correspond to the single sampling without reordering, single sampling with reordering, plane-parallel and optimal with reordering experiments respectively.

Errors in the single sampling experiments are consistently lower when sub-columns are re-ordered, indicating that noise in the net flux values contributes to the surface temperature errors.

Figure 2.6 shows the distribution of the 1.5m temperature errors, three hours into the forecast and on the final time-step of the forecast for the optimal McICA and PP-MRO experiments. These errors were calculated by subtracting the temperature values in the benchmark from their equivalent values in the experiments. The vertical scale is logarithmic and in order to avoid discontinuities, we added one to all frequencies. Moreover, although only errors of magnitude four Kelvin are shown, larger errors were obtained, but these occur very infrequently.

As the radiative transfer scheme is called every three hours, the temperature errors at noon on the first day of the forecast (the inner two distributions) can be traced to radiative fluxes and heating rates on the first model time-step, where the radiative transfer calculation was performed for identical atmospheres. Subsequent temperature errors are contaminated by radiative feedbacks

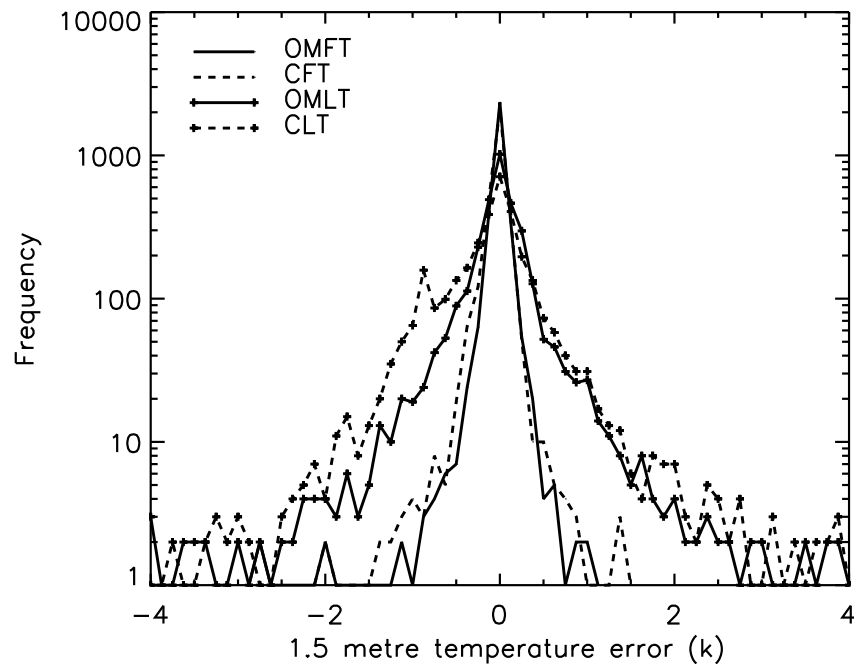


Figure 2.6 Frequency of 1.5m temperature errors of given magnitude. The solid lines correspond to the optimal McICA experiment, while the dashed lines correspond to the PP-MRO experiment. Lines with '+' symbols correspond to results at the end of the experiment, while the lines without symbols correspond to the start of the experiment. Note that the vertical scale is logarithmic.

in the simulations.

The flux errors introduced by the McICA scheme are unbiased, so there is no bias in the 1.5m temperature errors, as Figure 2.6 shows. The mean McICA 1.5m temperature errors at the start and end of the model are -0.007 K and -0.008 K respectively. In contrast, the PP-MRO temperature errors are biased; on average the PP-MRO temperatures are too small, corresponding to a tendency to overestimate the SW cloud extinction. This is because the overestimation of cloud forcing due to the plane-parallel approximation is larger on average than the underestimation due to the maximum-random overlap assumption, (e.g. Shonk and Hogan, 2010; Barker *et al.*, 1999). As a result, the corresponding mean temperature errors for the PP-MRO experiment are -0.022 K and -0.125 K respectively.

The results presented so far depend on the generated cloud and thus in particular the input

estimates of fractional standard deviation and decorrelation scale. We tested the sensitivity of the results to these parameters by repeating the above experiments using a range of parameter values. Sensitivity to fractional standard deviation was examined by conducting experiments with fractional standard deviations of 0.5 and 1.0, while sensitivity to decorrelation scales was studied in further simulations with decorrelation scales of 50 hPa and 200 hPa. Table 2.4 presents the results from these experiments. For conciseness, we have calculated mean values in time.

Decorrelation Scale (hPa)	Fractional Stand. Dev.	PP-MRO	Optimal McICA	Single McICA	No reordering McICA
100	0.75	0.247	0.182	0.234	0.244
100	0.5	0.266	0.193	0.239	0.246
100	1.0	0.244	0.182	0.242	0.241
50	0.75	0.292	0.184	0.236	0.236
200	0.75	0.220	0.189	0.241	0.245

Table 2.4 Absolute 1.5 m temperature errors for each of the methods of treating cloud and a selection of decorrelation scales and fractional standard deviations. For conciseness, these means are calculated by averaging across all model points at all times.

From Table 2.4 we can see that the extent of horizontal inhomogeneity and vertical overlap in the generated cloud has little impact on the magnitude of the McICA 1.5m temperature errors. On the other hand the PP-MRO errors are sensitive to the choice of decorrelation scales and fractional standard deviation used in the benchmark. If the input parameters are considered individually, the PP-MRO error will tend to zero as fractional standard deviation tends to zero and decorrelation scales tend to infinity. However, the pattern is complicated by the fact that the inhomogeneity and overlap errors are in opposite directions. In any case, although the PP-MRO errors depend on the input parameters to the cloud generator, for all choices of parameters, the optimal McICA experiment results in a smaller mean absolute 1.5m temperature error than the PP-MRO.

For GA3.0 (Global Atmosphere 3.0; Walters *et al.* (2011)) N320 (640 longitude points and 481 latitude points) 1.5 m temperature forecasts, global root mean square errors (with respect to observations) for land points are typically an order of magnitude larger than the mean absolute errors considered here (i.e. 2-3 K). In comparison, the mean effect of reducing noise on surface

temperature absolute errors (around 0.05 K) is rather insignificant. Nevertheless, the optimal version of McICA is recommended because of the significantly reduced likelihood of larger surface temperature errors.

2.5 CONCLUSIONS

This chapter has considered the effect of McICA noise on NWP simulations. We used CRM cloud fields and an offline version of the radiative transfer scheme to examine the magnitude of McICA noise and suggested methods for efficiently reducing the magnitude of this noise, including a mechanism for reducing the net error when SW and LW errors are combined. We tested the effect of noise on a low resolution global NWP simulation, focusing in particular on near-surface temperature. We found that a simple implementation of McICA gives worse forecasts of near-surface temperature than the widely-used combination of the plane-parallel and maximum-random overlap assumptions. However, when noise was reduced using the methods we suggest, the temperature forecasts were an improvement over those from the plane-parallel, maximum-random overlap simulation.

While we have shown that the McICA scheme can improve forecasts of near-surface temperature in comparison to a full ICA benchmark, it remains to show that it gives an improvement compared to observations. This will depend on the ability of the cloud generator to provide realistic cloud fields, which in turn depends on the input values of decorrelation scale and fractional standard deviation. Thus future work shall consider the values of these input parameters, with the aim of refining the generator, thereby improving the model across all time-scales, from NWP through monthly and seasonal to climate.

CHAPTER 3:

**PARAMETRIZING THE HORIZONTAL
INHOMOGENEITY OF ICE WATER
CONTENT USING CLOUDSAT DATA
PRODUCTS**

This chapter has been published as Hill *et al.* (2012).

3.1 INTRODUCTION

Many of the processes that are modelled in general circulation models (GCMs) are non-linear and the physical quantities on which these processes depend are often spatially variable at unresolved scales. Consequently, the process rate calculated using the gridbox mean value of such a variable is a biased estimate of the mean process rate within each gridbox. One such physical quantity is cloud water content. Pincus and Klein (2000) estimated that process rates calculated from gridbox mean water content values could have relative biases as large as 100%. Larson *et al.* (2001) showed that representing subgrid-scale water content variability is important for microphysics and thermodynamical processes. In particular they suggested that neglecting water content variability could lead to reduced autoconversion rates in GCMs. Subgrid-scale water content variability is also important for radiative transfer calculations; the radiative effect of a cloud depends non-linearly on the cloud water content (e.g Han *et al.*, 1998). As a result, GCM radiative transfer calculations that use the mean cloud water content and assume that clouds are horizontally homogeneous do not give the correct domain mean radiative fluxes (e.g. Cahalan *et al.*, 1994a).

In the past decade, computationally efficient methods for representing the radiative effects of subgrid cloud water content variability have been developed and tested (e.g. Pincus *et al.*, 2003; Li *et al.*, 2005; Shonk and Hogan, 2008; Hill *et al.*, 2011). Monte Carlo methods have also been suggested for representing the microphysical effects (Larson *et al.*, 2005). While progress has been made towards representing the effects of subgrid-scale cloud variability in GCMs, it remains unclear how much subgrid-scale water content variability exists.

A number of articles have used observations to quantify horizontal cloud water variability (e.g. Rossow *et al.*, 2002; Hogan and Illingworth, 2003; Oreopoulos and Cahalan, 2005). However, as highlighted in the review of Shonk *et al.* (2010), these published articles use different inhomogeneity parameters, observation sources, cloud types and space and time scales. As a consequence of this their results and conclusions are quite different and in some cases seem contradictory.

Studies that have considered radiative sensitivity to the magnitude of cloud water content variability suggest that it can have a significant impact. Shonk and Hogan (2010) estimated that the uncertainty in their estimate of a global mean variability parameter could change the global mean top of atmosphere (TOA) net radiation budget by 2-4 Wm^{-2} . For a small systematic change to a globally varying inhomogeneity parameter, Barker and Räisänen (2005) estimated a smaller, but still significant change of 0.98 Wm^{-2} , with larger changes at most latitudes. Although these values are small, they are a significant proportion of the net cloud radiative effect (CRE) at TOA, estimated to be around 18 Wm^{-2} (Allan, 2011). Gu and Liou (2006) considered the difference between two 5-year climate simulations. In one they scaled the optical depth of all clouds by a globally constant factor of 0.7 to account for water content inhomogeneity. In the other they used a globally varying climatological scaling factor for high-level clouds derived from International Satellite Cloud Climatology Project (ISCCP) data. They found significant differences, not only in the cloud albedo, which is directly affected by the change, but also in the cloud and precipitation fields.

Barker *et al.* (1996) found significantly different inhomogeneity parameters for stratocumulus and cumulus clouds, while Oreopoulos and Cahalan (2005) showed that cloud inhomogeneity varies with latitude. This implies that cloud water content variability depends on the meteorological regime, which means that a global mean inhomogeneity parameter will be a biased estimate of

the inhomogeneity for different regimes. In a GCM simulation these biases could have feedback effects leading to further errors. GCMs do not generally predict meteorological regimes explicitly (e.g. they don't explicitly predict whether a cloud is stratocumulus or cumulus). Moreover using an inhomogeneity parameter that depends on location as in Gu and Liou (2006) means that the inhomogeneity parameter will be unable to respond to changes in climate. However, it may be possible to capture this dependence on regime using some of the variables predicted in a GCM.

In this chapter we describe water content variability in terms of the fractional standard deviation (FSD) of cloud water content. The FSD is simply the standard deviation divided by the mean. FSD was chosen as the inhomogeneity parameter because it accounts for the strong correlation (e.g. Carlin *et al.*, 2002) between the mean and standard deviation of cloud water content, and it has been used in previous studies of water content variability (e.g. Räisänen *et al.*, 2004; Shonk *et al.*, 2010). We are interested in in-cloud variability, so only include cloudy values (i.e. water content greater than zero) in the calculation of FSD. Moreover, we are interested only in the instantaneous spatial variability, not unresolved temporal changes in cloud water content, the radiative effects of which can be modelled by using output from a GCM cloud scheme (e.g. Manners *et al.*, 2009)

This study of cloud water content variability is based on CloudSat data. CloudSat (Stephens *et al.*, 2008) is a polar orbiting satellite that carries a cloud radar and is part of the 'A-train', a constellation of satellites each carrying different instruments, orbiting the earth in sufficiently close proximity for their observations to be combined. The data product resolves cloud water content (the mass of liquid or ice water per unit volume of air) vertically and horizontally and thus is an excellent resource for the study of the magnitude of in-cloud water content variability. This chapter focuses on ice water content (IWC) variability as the retrieval is thought to be more accurate than that of liquid water. For further details on the CloudSat data used in this study, see Section 3.2.

This chapter describes the development of a parametrization for the FSD of ice water content, suitable for use in both numerical weather prediction (NWP) and climate models, based on CloudSat data. Section 3.2 consists of a brief description of the CloudSat data used in the study. In section 3.3 we perform a spectral analysis of the data, in order to inform the study of the dependence of water content variability on horizontal resolution, which is described in section 3.4.

Section 3.5 discusses the sensitivity of FSD to the cloud fraction, while section 3.6 considers the effect of vertical resolution on the FSD. The final parametrization for use in GCMs is presented and tested in 3.7. Finally, conclusions are drawn and avenues for further work are highlighted in section 3.8.

3.2 CLOUDSAT DATA

CloudSat was launched in April 2006 and data are available from June 2006. As one of five satellites in the sun-synchronous A-train, CloudSat orbits in close proximity to the Aqua satellite carrying the Moderate-Resolution Imaging Spectroradiometer (MODIS), which measures radiances. A number of CloudSat products have been developed, which combine observations from CloudSat, Aqua and other A-train satellites and are available from the CloudSat website (<http://www.cloudsat.cira.colostate.edu>). In particular, this study uses the 2B-CWC-RVOD (cloud water content, radar and visible optical depth) product, which combines CloudSat observations with MODIS radiance observations from the Aqua satellite in order to estimate the distribution of cloud water content within the atmosphere.

The algorithm used to produce this product is a modified version of that used to produce the equivalent radar only product that is described by Austin *et al.* (2009). We shall provide a brief description of the method for retrieving ice water content. A more extensive description is available from the CloudSat website.

The retrieval assumes that ice particles are spheres with a log-normal particle size distribution (PSD). The PSD has three parameters: the geometric mean particle diameter, the distribution width parameter and the total particle number concentration. A priori values for the first two parameters are temperature dependent. The a priori particle concentration is more complex (see Austin *et al.* (2009) for details). Optimal parameter values are obtained by using the PSD to forward model the extinction and backscatter, then comparing to observations. Once the optimal parameters have been calculated, ice water content is calculated by integrating over the PSD, assuming the ice particles have the density of solid ice (0.917 kgm^{-2}). Separate retrievals are performed for liquid and ice; ice properties are used at temperatures less than -20°C , liquid at temperatures larger than 0°C and a linear combination of the two at intermediate temperatures.

Each of the 2B-CWC-RVOD profiles measures 1.7 km along track and 1.3 km across track and divides the atmosphere into 125 vertical layers each of which is 240 m thick. At this horizontal scale, almost all of the cloud water content variability is captured (Oreopoulos and Davies, 1998a). The largest length scales used in this study consist of 500 CloudSat profiles, which corresponds to 850 km. As a new CloudSat profile is observed every 0.16 seconds, 850 km of data is observed in only 80 seconds and any variability is approximately instantaneous, an advantage over ground-based studies where changes in time are assumed to be due to changes in space advected over the site (e.g. Hogan and Illingworth, 2003).

The cloud profiling radar on board CloudSat operates at 94 GHz. At this frequency radars suffer virtually no attenuation by ice water (Hogan and Illingworth, 1999). However, in liquid clouds, drizzle droplets can dominate the radar reflectivity factor while containing negligible liquid water and thus the radar reflectivity factor is not a good indicator of the liquid water content (Fox and Illingworth, 1997). For this reason, CloudSat estimates of ice water content are expected to be more accurate than those of liquid water content. Hence we focus on the FSD of ice water content. It should be noted that this ice water content includes all frozen hydrometeors. Thus the results presented here are not necessarily applicable to ice particles that have been split into multiple categories, such as “precipitating” and “suspended”.

This study uses data from two separate arbitrarily chosen periods. Initially we use data observed between 22nd December 2007 and 10th January 2008, a total of 9,752,539 CloudSat profiles, and over a billion values of ice water content. As the satellite is polar orbiting, this includes observations from all latitudes and longitudes and should be representative of the whole CloudSat data set. Nevertheless, to check that it is indeed representative, we test the parametrization on data observed between 15th June and 25th June 2006 (5,006,028 profiles and over 500 million water content observations).

3.3 SPECTRAL ANALYSIS

A number of metrics have been used to study the statistical properties of clouds (e.g. Marshak *et al.*, 1997). In this section we use one such technique, spectral analysis, to study CloudSat ice water content. We chose this metric as it is most widely used in the existing literature (e.g.

Cahalan and Joseph, 1989; Lewis *et al.*, 2004; Davis *et al.*, 1999) and thus allows us to confirm that the spatial statistical properties of the CloudSat ice water content are consistent with other observation sources. This spectral analysis complements the following section, which considers how the FSD changes with horizontal domain size.

Many previous studies have observed that for scales between metres and tens of kilometres, the wavenumber spectrum of cloud water content approximately follows a $-5/3$ power law (e.g. Davis *et al.*, 1996; King *et al.*, 1981). However, this $-5/3$ power law is not observed universally. For example, using ground-based radar observations of a cirrus cloud, Hogan and Kew (2005) found that for scales less than 50 km, the power spectrum of the natural logarithm of ice water content appears to obey a $-5/3$ power law at cloud top, with the spectra becoming steeper with depth into the cloud, obtaining values as low as -3.5 in some cases. This is thought to be due to the effects of wind shear. For scales larger than 50 km they find that the spectra are flat. Lewis *et al.* (2004) calculated spectra for LandSat observations of marine boundary layer clouds. They considered 12 overcast and 12 partially cloudy scenes and found that the spectrum of liquid water path obeyed a $-5/3$ power law for overcast scenes. For the partially cloudy scenes the spectra displayed more scene to scene variability with the average spectrum following a -1 power law.

We calculated the mean ice water content spectrum for isolated clouds of various sizes, the smallest containing 8 CloudSat cells and the largest containing 128 cells (i.e. 13.6 km and 217.6 km long respectively). These spectra were produced as follows. Each layer of the CloudSat data was divided into individual clouds, separated by at least one clear-sky cell. The ice water content for each cloud was divided by the mean ice water content for that cloud and the spectrum for the resulting normalised ice water content was calculated. The spectra for individual clouds of the same size were then averaged together and multiplied by the size of the cloud (i.e. the number of cells in the cloud). By Parseval's theorem, the integral of the resulting mean spectrum for a given cloud size is equal to the mean fractional variance (FVAR) for clouds of that size, where the FVAR of a cloud is defined as the square of the FSD of that cloud. (Note however, that as the square is non-linear, the mean FVAR is not equal to the square of the mean FSD.) These spectra are shown in Figure 3.1 below.

Figure 3.1 shows several interesting features. The spectrum for each cloud size appears to approximately obey a $-5/3$ power law, as shown by the thick black line. This is consistent with

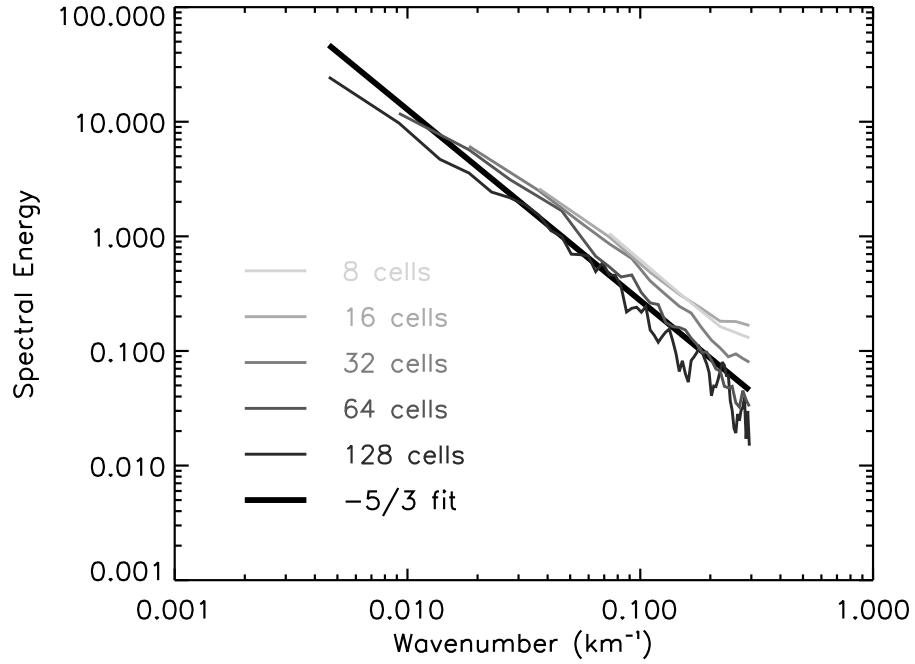


Figure 3.1 Mean spectra for clouds of fixed size, ranging from 8 to 128 CloudSat cells (thin lines). For comparison, the thick black line obeys a $-5/3$ power law.

the existing literature, as described at the beginning of this section. While the spectra obey a $-5/3$ power law for all cloud sizes, the values of the spectra decrease for larger clouds. This implies that the FVAR per unit length of a small cloud is larger on average than that of a larger cloud. Despite this, the integral under the spectrum increases for larger clouds, because we integrate over a larger horizontal scale.

As the mean spectrum, E for a cloud of length x can be approximated by a power law of the form

$$E = A(x)k^{-5/3}, \quad (3.1)$$

where k is the wavelength, the mean FVAR for a cloud of length x can be calculated by integrating under the spectrum as follows

$$\text{FVAR} = \int_{1/x}^{1/x_1} E(k)dk = A(x)(x^{2/3} - x_1^{2/3}). \quad (3.2)$$

The upper limit of the integral, $1/x_1$ corresponds to the maximum wavenumber for which the spectrum is defined. This means that x_1 is equal to the resolution of the data, which in the case of the 2B-CWC-RVOD data used here equals 1.7 km.

Water content spectra have been observed to follow power laws down to scales as small as 3 m (King *et al.*, 1981). This suggests that the spectra observed in Figure 3.1 can be extrapolated to smaller scales. In this case, the mean FVAR for a cloud of length x will simplify to

$$\text{FVAR} = A(x)x^{2/3}. \quad (3.3)$$

Note however, that while this is a prediction of the actual FVAR, to ensure the best comparison to the CloudSat data we must include the x_1 in order to exclude the variability that is unresolved in the data.

In our spectral analysis, we have considered how ice water content variability changes with cloud size. However, the sizes of individual clouds are not predicted in GCMs, which in general simply predict the cloud fraction within a gridbox. Consequently the observed relationship between variability and cloud size cannot be used as a basis for the parametrization.

3.4 HORIZONTAL SCALE

In this section we consider how the FSD of ice water content changes with the scale of the domain over which it is calculated. For ground-based cloud radar data, Hogan and Illingworth (2003) found that, for overcast gridboxes, the FVAR of ice water content was proportional to the size of the gridboxes to the power of 0.3 for scales up to 60 km, but that it grows no further for larger gridboxes.

To calculate the IWC FSD for a given domain size, each layer of the data is sub-divided horizontally into adjacent ‘gridboxes’ each containing the same number of CloudSat cells. For each gridbox that contains more than one cloudy cell the FSD is calculated. Figure 3.2 shows the mean FSD of both ice water content and ice water path (calculated by summing the ice water content in a column), calculated for gridboxes ranging from 4 to 500 profiles (6.8 to 850 km) in size. The FSD rises sharply with gridbox size at smaller scales, then levels off at larger scales. Note that the

FSD for water path is larger than that for water content. This contradicts the suggestion by Shonk *et al.* (2010) that the FSD for water content was larger. This relationship is considered in more detail in section 3.6, where we consider the effect of the layer thickness on the inhomogeneity.

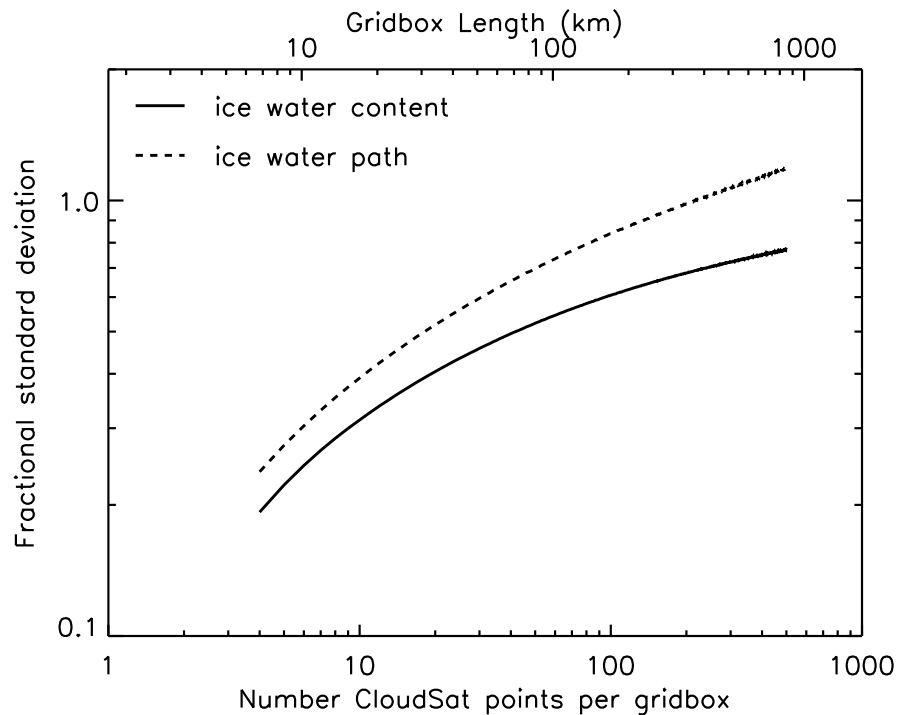


Figure 3.2 Mean FSD of ice water content (solid line) and ice water path (dashed line) when data is divided into horizontal boxes containing the given number of CloudSat profiles.

The trend of the FSD can be explained by the results of the spectral analysis. The FSD increases with gridbox size because as the gridbox size is increased, the gridbox may contain larger clouds, which have larger values of FSD. The slope decreases with gridbox size because the rate at which the FSD rises with cloud size decreases and larger clouds occur less frequently.

Figure 3.3 again shows how the FSD of ice water content increases with gridbox size (solid black line), this time with vertical bars that show the standard deviation of the FSD for a selection of the gridbox sizes. The dashed line shows the case when we include only overcast gridboxes, in which case the results are similar to those of Hogan and Illingworth (2003), who also considered only overcast gridboxes. Note that the standard deviation of the FSD is much smaller when only overcast gridboxes are included. This implies that a considerable amount of the variability of the

FSD is due to the variability in cloud fractions, which suggests there is a significant relationship between FSD and cloud fraction, which is considered in more detail in Section 3.5. As the FSD for overcast gridboxes is less variable, we shall begin by parametrizing this and then extend the parametrization to capture some of the extra variability that is introduced when different cloud fractions are considered.

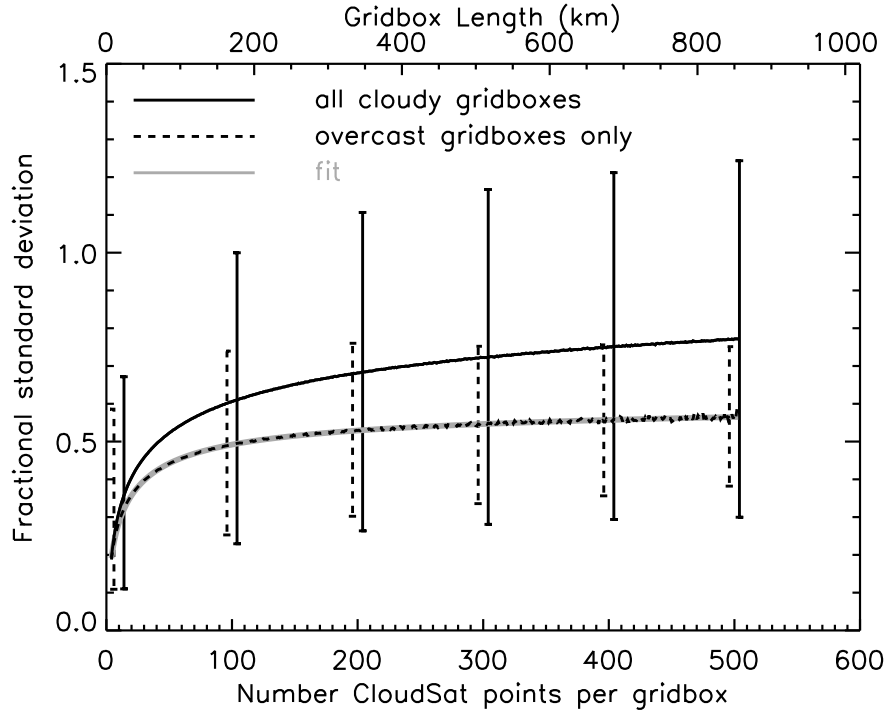


Figure 3.3 Mean FSD of ice water content as a function of gridbox size for all data (solid line) and only those gridboxes that are overcast (dashed line). The vertical bars show the standard deviation of the FSD for the given gridbox size. The grey line shows the FSD given by equation 3.5.

An overcast gridbox can only contain clouds that are larger than or equal to that gridbox in size. Thus the mean FSD for an overcast gridbox of size x can be calculated by summing the contributions to the FSD for each cloud size, approximately equal to the square root of equation 3.2, and weighting by the likelihood of sampling a cloud of that size,

$$\text{FSD} = \sqrt{x^{2/3} - x_1^{2/3}} \sum_{z=x}^{\infty} \sqrt{A(z)} W(z), \quad (3.4)$$

where $W(z)$ is the likelihood of an overcast gridbox of size x being a sample from a cloud of size z . Using a gradient-expansion algorithm to compute a non-linear least squares fit, we can

approximate the sum by a combination of power laws, resulting in the following parametrization for the FSD of an overcast gridbox of size x km,

$$\text{FSD} = 0.13\sqrt{x^{2/3} - 1.41} \left[(0.016x)^{1.10} + 1 \right]^{-0.26}. \quad (3.5)$$

The FSD predicted by equation 3.5 is shown by the grey line in Figure 3.3 and is an excellent fit to the mean observed FSD. Note that the -1.41 term corresponds to putting the CloudSat resolution as the value of x_1 and is only necessary when comparing to the observed data, to account for the unresolved variability.

3.5 VARIABILITY AS A FUNCTION OF CLOUD FRACTION

According to Cahalan (1994), in the case of California marine stratocumulus, the liquid water content variance increases as the cloud fraction increases. This could perhaps be explained by the horizontal scale dependence discussed in the previous section. By contrast, Oreopoulos and Cahalan (2005) found no strong relationship between cloud fraction and inhomogeneity, except for cloud fractions greater than 0.9, when clouds become considerably more homogeneous. In this section, we investigate the relationship between FSD and cloud fraction and attempt to explain these apparently contradictory results.

Figure 3.4 shows the mean FSD when gridboxes with cloud fraction within a given range are binned together. Values for gridboxes containing 25, 50, 100 and 200 CloudSat cells are shown. For all gridbox sizes, FSD initially increases with cloud fraction, then remains fairly constant, before dropping off sharply if the gridbox is overcast. As the gridbox size is increased, the cloud fraction at which the FSD no longer increases gets smaller. This suggests that the observed increase in FSD with cloud fraction is related to cloud size rather than cloud fraction.

Assuming that the CloudSat resolution is sufficient to resolve cloud edges, an overcast gridbox contains only a single cloud and in almost all cases excludes the edges of that cloud. In theory, either or both of these could lead to the steep decrease in FSD that is observed as cloud fractions approach one. A gridbox containing a single cloud may have a lower in-cloud FSD than one containing multiple clouds, which includes contributions from both internal cloud variability and

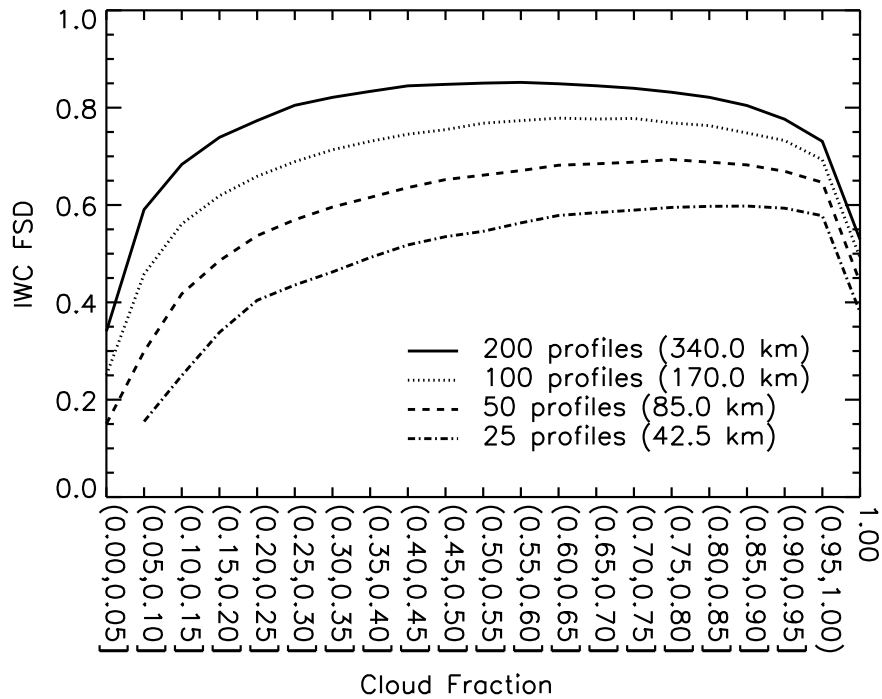


Figure 3.4 Fractional standard deviation of ice water content (IWC FSD) as a function of cloud fraction for gridboxes containing 200, 100, 50, and 25 CloudSat cells (solid, dotted, dashed and dot-dashed lines respectively).

the variance in mean water content between different clouds (cf. Figure 3.8). Cloud edges often contain lower values of liquid water content than the rest of the cloud, and as a result have the effect of both increasing the variability of water content in the cloud and decreasing the mean water content of the cloud. Both of these lead to larger values of FSD.

Alongside the FSD for all gridboxes, Figure 3.5 shows the FSD for those gridboxes that contain exactly one cloud, but not necessarily the entire cloud (where a gridbox contains one cloud if the cloudy cells are not separated by any clear cells). Also shown is the FSD for gridboxes that contain exactly one cloud and both cloud edges (where the edges are defined as the single cloudy cells at either end of the cloud). Data for gridboxes containing 50 cells are shown. It is clear that the drop in FSD as cloud fraction nears one is due to the fact that overcast gridboxes tend not to include cloud edges.

Equation 3.5 gives the FSD only for a cloud fraction of one. In developing a parametrization

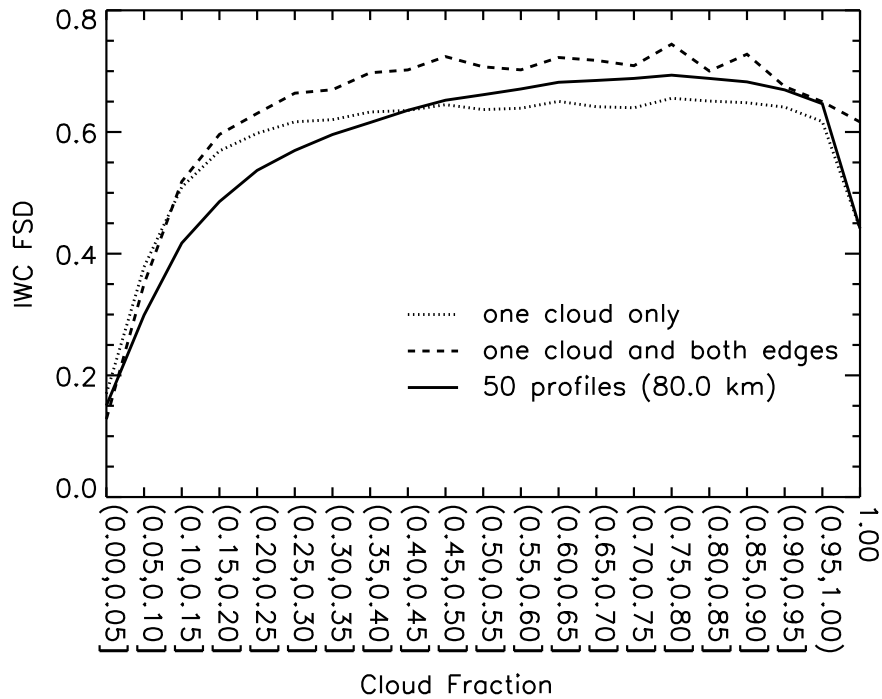


Figure 3.5 Fractional standard deviation of ice water content (IWC FSD) as a function of cloud fraction for gridboxes containing 50 cells. Solid lines show the FSD for all gridboxes. Dotted lines show the FSD for those gridboxes that contain one cloud only. Dashed lines show the FSD for those gridboxes that contain only one cloud and contain all of this cloud.

applicable to smaller cloud fractions, we start by replacing the dependence on gridbox size (x) with a dependence on cloud extent (xc) (i.e. the gridbox size multiplied by the cloud fraction). However, the resulting FSD is an underestimate for cloud fractions smaller than one. The four thin black lines in Figure 3.6 show the ratio of the observed mean FSD to this predicted FSD, for the same 20 cloud fractions and four gridboxes sizes in Figure 3.4. Note that we do not include overcast scenes, for which equation 3.5 is a good estimate. These ratios are reasonably similar for all gridbox sizes, except for small cloud fractions, where the FSD is already small, so a large difference in ratio has less impact. Since the ratios are similar, we average across the four gridbox sizes, as shown by the light grey line and then fit a linear function of cloud fraction to this average, as shown by the thick dark grey line.

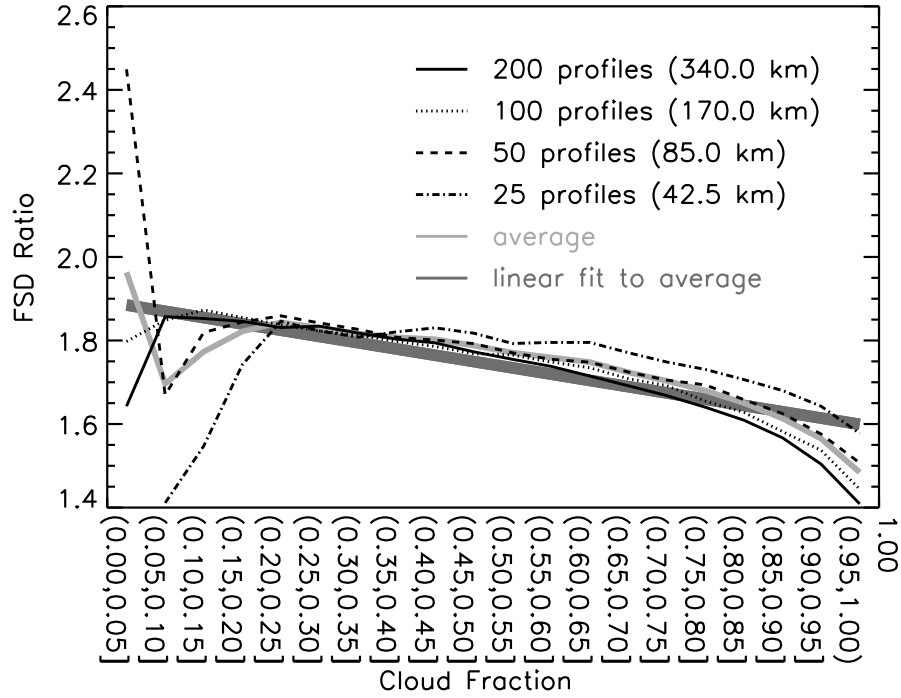


Figure 3.6 Ratio of observed ice water content fractional standard deviation (FSD) and the FSD predicted by equation 3.5 as a function of cloud fraction. Note that we use the cloud extent instead of the gridbox size in equation 3.5. The thin black lines correspond to the observed relationship for the different gridbox sizes. The light grey line shows the average relationship for these gridbox sizes and the dark grey line shows a linear fit to this average relationship.

Combining the average ratio estimated from Figure 3.6 and the FSD based on cloud extent gives the following equation for the FSD for a partially cloudy gridbox.

$$\text{FSD} = (0.25 - 0.04c)\sqrt{(xc)^{2/3} - 1.41} \left[(0.016xc)^{1.10} + 1 \right]^{-0.26} \quad (3.6)$$

where c is the cloud fraction. The FSD predicted by this equation is shown in Figure 3.7. The equation captures the FSD pattern well, though the slight decrease in FSD as cloud fractions approach one, which is particularly evident for the large gridboxes, is not captured by the parametrization. As a result the FSD for cloud fractions around 0.9 is overestimated. For the smallest gridboxes, the FSD for very small cloud fractions is overestimated. However, for other gridbox sizes the initial increase in FSD with cloud fraction is very well predicted and for intermediate cloud fractions the parametrization errors are small. Despite being relatively simple, the

parametrization provides a very good estimate of the complex relationship between IWC variability and cloud fraction at all gridbox sizes.

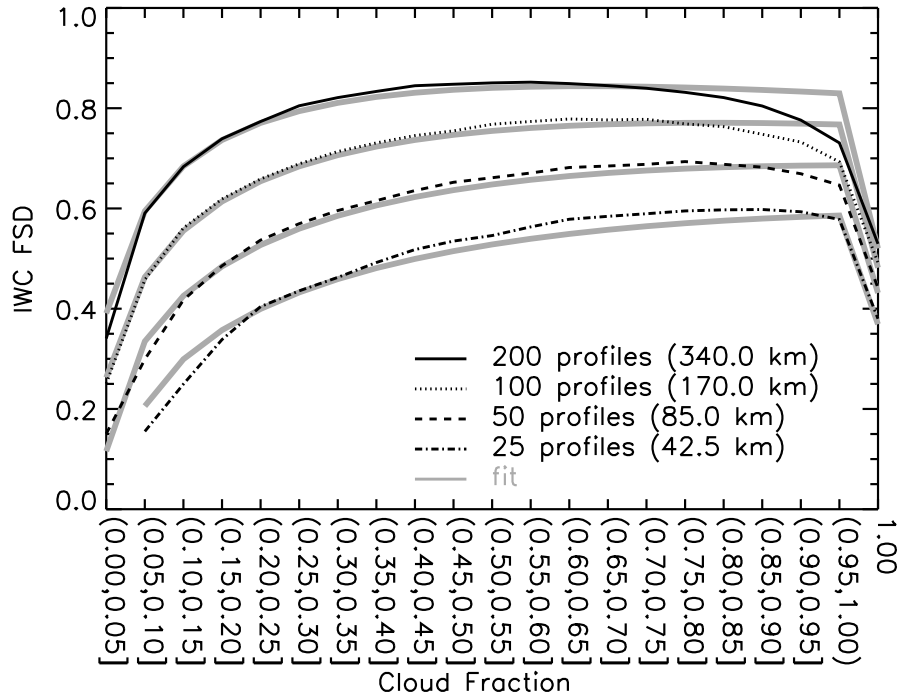


Figure 3.7 Fractional standard deviation of ice water content (IWC FSD) as a function of cloud fraction. Black lines are as in Figure 3.4. Grey lines show the FSD predicted by equation 3.6.

3.6 VERTICAL LAYER THICKNESS

Figure 3.2 shows that the FSD of ice water path is larger than that of ice water content, which suggests that the FSD increases as vertical resolution decreases. This section considers the relationship between FSD and vertical layer thickness in more detail.

To determine the sensitivity of FSD to vertical scales, IWC values are averaged in the vertical to create thicker layers. For example, after the original data, the next highest resolution data was calculated by summing the IWC in adjacent layers to create a profile containing 124 overlapping vertical layers each of which is 480 m thick (recall the original data has 125 layers, each of which is 240 m thick).

Figure 3.8 shows the mean FSD calculated for layers of the given thickness, for two different horizontal gridbox sizes, containing 200 and 25 CloudSat cells. The solid lines include all data and show that the FSD increases as layer thickness increases. The increase is most rapid for the thinnest layers, which correspond to the vertical resolutions that are likely to be used in GCMs.

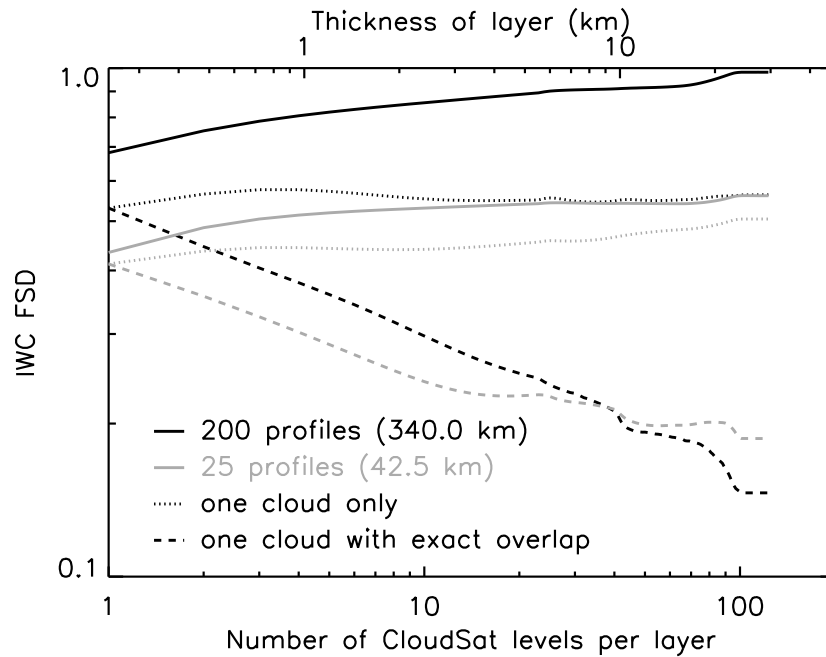


Figure 3.8 Mean fractional standard deviation of ice water content (IWC FSD) for given vertical resolution. The solid lines show the mean FSD when no restrictions are applied to the data, the dotted lines show the mean FSD for those gridboxes that contain only one cloud (i.e. no breaks between cloudy cells) and the dashed lines show the FSD for those gridboxes that contain only one cloud where exactly the same cells contain cloud in each layer of the original data. The black lines correspond to gridboxes containing 200 cells and the grey lines to gridboxes containing 25 cells.

The increase in FSD as the layer thickness increases can be explained as follows. Consider a gridbox containing multiple layers, each of which contains n cloudy cells, covering a fraction of the gridbox. Assume that the clouds are horizontally homogeneous and the water content in each cloudy cell equals x . Thus the FSD in any layer equals zero. Now sum the water contents in the vertical. If the same n cells are cloudy in each layer (i.e. the clouds are exactly overlapped), then

the integrated water content in each column will be the same and the FSD will be zero. However if not, then the columns would contain different integrated water content and FSD will be non-zero. That is, the integrated FSD would be larger than that in any layer because the integrated FSD is accounting for apparent in-cloud inhomogeneity that is in fact simply due to the vertical resolution being insufficient to resolve cloud boundaries.

The dashed lines in Figure 3.8 show how the FSD changes with layer thickness for gridboxes that contain one cloud whose layers are exactly overlapped (i.e. the vertically integrated cloud fraction is identical to the cloud fraction in each layer). For these gridboxes, the FSD does not need to account for any unresolved cloud structure. Hence the FSD decreases as layer thickness increases. This is the behaviour predicted by Shonk *et al.* (2010), who suggested that this is because in-cloud water content decorrelates as the distance between layers increases (e.g. Barker and Räisänen, 2005; Hogan and Illingworth, 2003), which has the effect of smoothing the vertical average.

The FSD for those gridboxes that contain exactly one cloud, with no restriction on overlap between cloud in different layers, is shown by the dotted lines in Figure 3.8. Now the FSD has to account for some unresolved cloud structure. As the layer thickness increases, the amount of unresolved structure increases. The competing effects of the unresolved cloud structure and the smoothing effect of decorrelating water content lead to an FSD that generally increases slightly with layer thickness.

If no restrictions are placed on the gridboxes (other than that they contain some cloud), then there may be multiple clouds in the gridbox and as the layer thickness increases, there may be a great deal of unresolved cloud structure. This means that the FSD increases significantly as layer thickness increases, as shown by the solid lines in Figure 3.8.

Figure 3.8 suggests that FSD of ice water content is quite sensitive to vertical resolution and that it is worthwhile including a vertical resolution dependence in any parametrization. For simplicity, the parametrization is restricted to layers that are thinner than 2.4 km (i.e. contain less than 10 CloudSat layers). Beyond this scale, the relationship between FSD and layer thickness cannot be accurately described with a simple equation. Moreover, the relevant layers in current GCMs (i.e. the layers that contain clouds) are generally thinner than 2.4 km.

The relevant part of Figure 3.8 is shown again in Figure 3.9 (note that it is no longer in log-log space). The broken lines show the relationship between FSD and layer thickness, which appears to be best described by a power law. The dark grey lines show the mean FSD given by equation 3.6. Neither of the dark grey lines show any significant change with increasing thickness, which implies that the thickness dependence is independent of this equation. Thus we assume that we can predict the FSD for a single layer exactly and simply consider how the relationship between this FSD and the multi-layer FSD changes with increasing layer thickness. Letting Δz denote the layer thickness (in km) and A denote the FSD for a single layer, a least square error fit gives

$$\text{FSD} = A \left(\frac{\Delta z}{0.24} \right)^{0.11}. \quad (3.7)$$

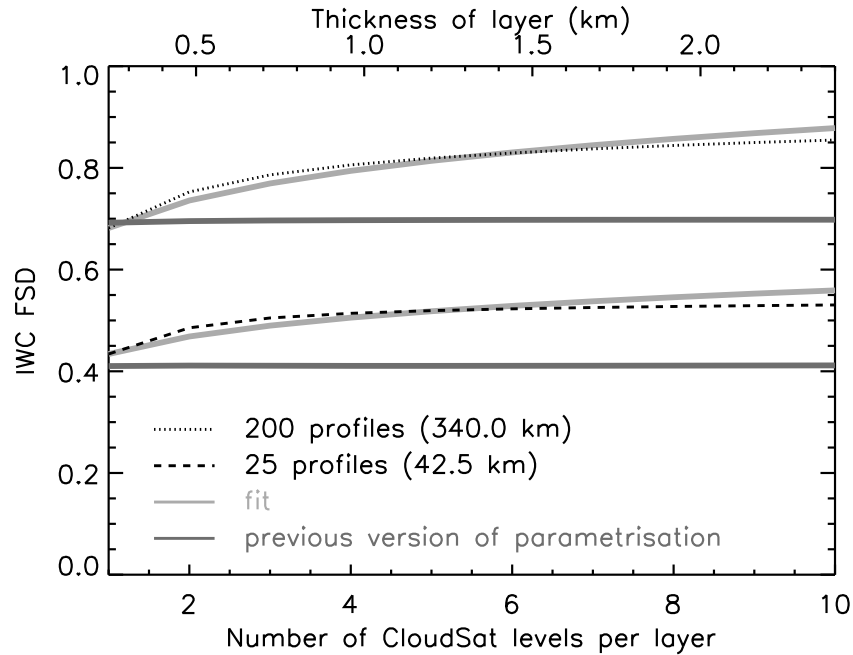


Figure 3.9 Mean fractional standard deviation of ice water content (IWC FSD) for vertical resolution between 240 m and 2.4 km. For gridboxes of length 340 km (dotted line) and 42.5 km (dashed line). The dark grey lines show the mean FSD predicted by equation 3.6, which does not include any dependence on layer thickness. The light grey lines show the FSD given by equation 3.7, where the value of A is chosen so that the equation gives the observed value of FSD for individual CloudSat layers.

3.7 PARAMETRIZATION

We have seen that the mean in-cloud FSD depends on the scale over which it is calculated (both horizontally and vertically) and cloud fraction. The remainder of this chapter illustrates how these relationships can be combined into a single parametrization and describes the results of testing this parametrization.

The mean FSD for a gridbox of horizontal length x km and thickness Δz km is obtained by combining equations 3.5-3.7 to get equation 3.8, where c is the cloud fraction. Note that x_1 is again equal to the minimum resolved scale, and for the purpose of comparing this parametrization to CloudSat observations is set to 1.7 km. However when this parametrization is implemented in a GCM, x_1 should be set to zero.

3.7.1 COMPARING OBSERVED FSD TO MODELLED FSD

The parametrization defined by equation 3.8 is tested on several days of CloudSat data from Summer 2006. These data are independent of the CloudSat data that were used to develop the parametrization. The data were divided into gridboxes of size 200, 100, 50 and 25 km (which corresponds to gridboxes containing 117, 59, 29 and 15 CloudSat profiles respectively) and thickness from 240 m to 2.4 km in 240 m increments (which corresponds to vertically averaging between 1 and 10 CloudSat layers). For each cloudy gridbox, the observed FSD and parametrized FSD were calculated. These were then used to calculate the parametrization bias (i.e. the mean difference between the FSD predicted by the parametrization and the observed FSD), shown in Figure 3.10 and the mean absolute error (the mean of the absolute value of the difference between the FSD

$$\text{FSD} = \begin{cases} (0.29 - 0.05c) \sqrt{(xc)^{2/3} - 1.41} \left[(0.016xc)^{1.10} + 1 \right]^{-0.26} (\Delta z^{0.11}) & \text{if } c < 1; \\ 0.15 \sqrt{x^{2/3} - 1.41} \left[(0.016x)^{1.10} + 1 \right]^{-0.26} (\Delta z^{0.11}) & \text{if } c = 1. \end{cases} \quad (3.8)$$

predicted by the parametrization and the observed FSD) of the parametrization, shown in Figure 3.11. To put these values into context, the bias and mean absolute error for a constant FSD equal to 0.75 are also shown. This is the global mean FSD for all cloud types estimated by Shonk *et al.* (2010) based on a review of the existing literature.

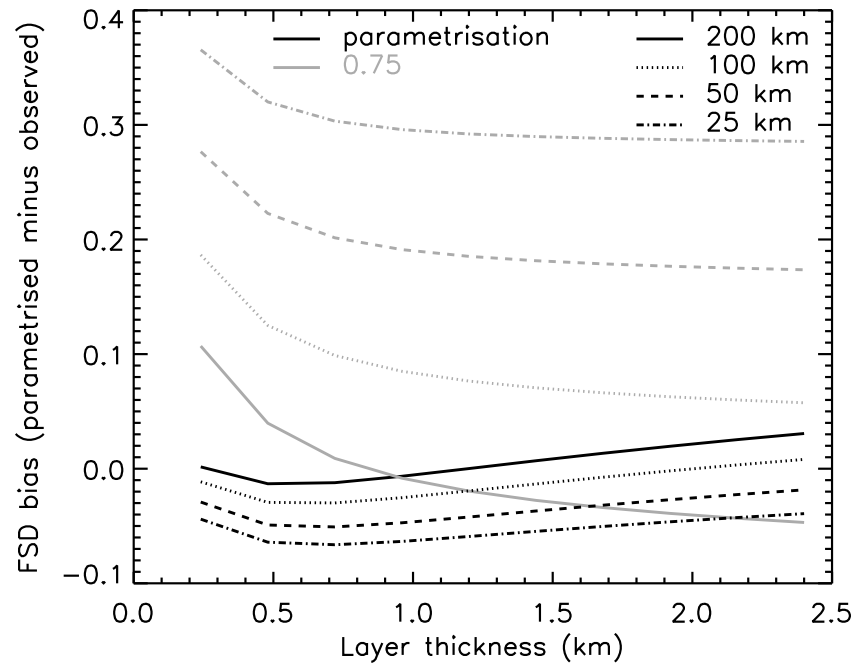


Figure 3.10 Mean difference between the fractional standard deviation (FSD) of ice water content given by equation 3.8 and the observed FSD, for layers between 240 m and 2.4 km in thickness and gridbox sizes of 200 (solid), 100 (dotted), 50 (dashed) and 25 (dot-dashed) km.

The bias of the FSD predicted by the parametrization is small for all gridbox sizes and layer thicknesses. The behaviour of this bias can be understood by considering the individual components of the parametrization. The relationship between FSD bias and layer thickness is similar for all four gridbox sizes and is the same as that for the thickness parametrization shown in Figure 3.9. The relationship between FSD bias and gridbox size is consistent with that shown in Figure 3.7. The constant FSD is a good estimate of the mean FSD for gridboxes that are 200 km in length, but overestimates the observed FSD for smaller gridboxes and has larger biases than the parametrization for all gridbox sizes.

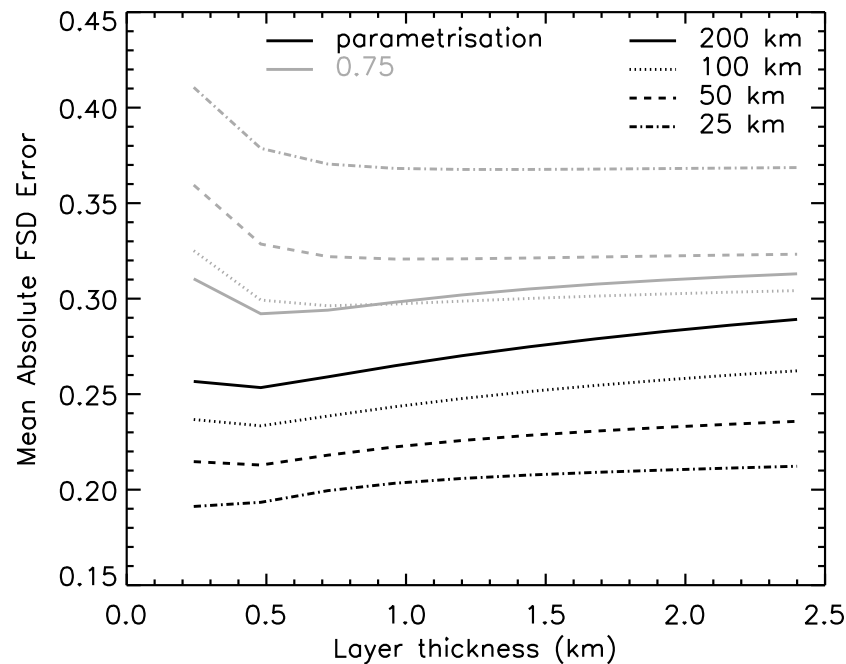


Figure 3.11 Mean absolute difference between the fractional standard deviation (FSD) of ice water content given by equation 3.8 and the observed FSD, expressed as a percentage of the mean observed FSD. Layers range from 240 m to 2.4 km in thickness and gridbox sizes are 200 (solid), 100 (dotted), 50 (dashed) and 25 (dot-dashed) km.

The mean absolute errors of the FSD predicted by the parametrization are shown in Figure 3.11. These errors increase with gridbox thickness and length. The largest error is approximately 0.29 and corresponds to gridboxes that are 2.4 km thick and 200 km long. The mean absolute errors for the parametrization are smaller than those obtained from the single FSD value for all gridbox sizes and thicknesses. Of particular note is the improvement for the gridboxes that are 200 km long and 1.0 km thick. Here the biases for both the parametrization and 0.75 are approximately zero. However, due to the cloud fraction dependence in the parametrization, the mean absolute error for the parametrization is significantly smaller than that for FSD=0.75.

The information shown in these figures is summarised in Table 3.1, which shows mean values across all the horizontal and vertical scales included in Figures 3.10 and 3.11. To add further context we also include the statistics for the mean FSD, calculated by averaging the mean FSD

for each of the resolutions shown in Figures 3.10 and 3.11. This is unbiased when all the data is combined, but biased for any individual resolution. The bias row shows the mean error of all biases shown in Figure 3.10, which is zero by definition for the mean. The mean absolute bias row shows the mean of the absolute value of the the biases shown in Figure 3.10 and the mean absolute error shows the mean of the absolute errors shown in Figure 3.11. The parametrization performs better than both the unbiased FSD value and the control FSD.

	Control (0.75)	Mean (0.60)	Param
Bias	0.15	0.00	-0.02
Mean absolute bias	0.16	0.11	0.03
Mean absolute error	0.33	0.28	0.24

Table 3.1 Mean statistics for all the data shown in Figures 3.10 and 3.11. The first column shows the statistics for a constant value of 0.75, the second column shows the statistics for the mean value for the data, and the third column shows the statistics for the parametrization given in equation 3.8.

The mean absolute FSD error can be split into four components. Some of the error is due to the relationships that are included in the parametrization being in error. This corresponds to the errors that arose when fitting equations to the observed trends. There is also a component due to an FSD dependence on variables that are not included in the parametrization. For example Hogan and Illingworth (2003) found a dependence on wind shear, which is not included in this parametrization, due to a lack of reliable global wind speed data to compare to the ice water content observations. The third component of the mean absolute error is the sampling error introduced when the observed FSD is calculated. This decreases as the gridbox size increases. This could be reduced by using higher resolution observations. The final component of the error is due to unpredictable variability of FSD; Hogan and Illingworth (2003) observed that even within a single cloud, the horizontal inhomogeneity varies significantly.

It should be noted that the ‘true’ parametrization errors are likely to be larger than those presented here; the CloudSat ice water content values contain errors, which will lead in turn to errors in the FSD derived from CloudSat data. CloudSat has a minimum detectable reflectivity of around -30 dBZ, which means that it may miss low ice water content values, which would lead

to an underestimate of the FSD. It would be useful to test the parametrization on data from other observation sources, to highlight the errors arising from the use of CloudSat data. Another source of error is that the parametrization gives the FSD for a 1D line; GCMs require the FSD for the 2D area represented by each gridbox. Full 3D cloud observations are required to calculate the desired quantities. These observations could be provided by scanning cloud radars.

3.8 SUMMARY

This chapter describes a study of ice water content variability using combined CloudSat and MODIS observations. Ice water content variability is considered in terms of the fractional standard deviation (FSD); the standard deviation divided by the mean. Results show that FSD increases as the horizontal scale over which it is calculated increases and when water content is averaged over larger vertical scales. A nonlinear dependence on cloud fraction was also identified; FSD was seen to increase with cloud fraction for small cloud fractions, while the mean FSD for overcast gridboxes was found to be significantly smaller than that for gridboxes with large cloud fractions. This decline in FSD was shown to be a result of overcast gridboxes excluding cloud edges. These relationships have been included in a relatively simple parametrization of ice water content, suitable for use in a GCM.

The performance of the new parametrization was tested using data taken from a different period in time. For the horizontal and vertical resolutions considered, the magnitude of the parametrization bias was shown to be less than 0.07. Mean absolute errors were found to be larger, but significantly smaller than those arising from the use of a single global FSD. The size of these mean absolute errors suggests that the parametrization could be developed further, either by using a function that better fits the relationships considered in this chapter, or by including the effect of other variables (e.g. wind shear) on the FSD. The parametrization should also be tested on other observational data, in order to expose any errors arising from the limitations of the CloudSat dataset and get a better estimate of the ‘true’ error.

In future work, this parametrization will be implemented in the UK Met Office Unified Model (MetUM) and tested in both NWP and climate simulations. Results of these tests should indicate

how much benefit there would be in further developing the parametrization, for example by linking FSD to meteorological regime.

In many GCMs ice particles are split into two or more categories (often described as ice and snow). However, there is no such split in either the CloudSat data product or the MetUM. Consequently, there is no such split in the parametrization described in this chapter. When this parametrization is included in other GCMs, care should be taken to ensure that it is applied to the *total* ice content. This may be more challenging for those GCMs which have a diagnostic ice category.

The existing parametrization is for ice water content only. Liquid water content variability is equally important and it is not clear whether it is significantly different. Using MODIS data, Oreopoulos and Cahalan (2005) found similar variability in ice and liquid clouds. On the other hand, Shonk and Hogan (2008) found that ice clouds exhibit more water content variability than liquid clouds. It would be informative to compare this parametrization to observations of liquid water content variability.

CHAPTER 4:

CLOUD VERTICAL OVERLAP

4.1 INTRODUCTION

The cloud schemes in most general circulation models (GCMs) predict a cloud fraction for each layer in each column, but the total cloud cover for a column is not directly predicted; instead it is computed by combining the layer cloud fractions with assumptions about how the clouds in each layer are vertically overlapped. These cloud vertical overlap assumptions can have large impacts. They directly affect the total cloud cover, which is the leading-order variable for determining the interaction of radiation and cloud and is also used to validate numerical weather prediction (NWP) models (e.g. Mittermaier, 2012). Changes to the overlap assumptions have been shown to have large impacts on the calculated radiative fluxes and heating rates (e.g. Morcrette and Fouquart, 1986) and also on cloud microphysics calculations (Jakob and Klein, 1999), which lead in turn to significant impacts in GCM simulations (e.g. Liang and Wang, 1997; Morcrette and Jakob, 2000).

From a radiation budget perspective, the most significant effect of changing the cloud overlap assumptions is on the total cloud cover; as the degree of overlap is decreased, the cloud cover is increased. This reduces the amount of shortwave (SW) solar radiation reflected to space (e.g. Barker and Räisänen, 2005). The cloud overlap assumption also affects the cloud fraction that is exposed to space in each layer, which is important for the computation of outgoing longwave radiation (OLR) and the heating rate profile (e.g. Barker *et al.*, 1999). Furthermore it can change the water path inhomogeneity; Hill *et al.* (2012) found that water path inhomogeneity was smaller when cloud edges overlapped exactly.

Until fairly recently, the radiative transfer schemes used in most GCMs applied the maximum-random overlap assumption, where clouds in adjacent layers are maximally overlapped and cloudy layers separated by clear-sky are randomly overlapped. In many observational studies (e.g. Hogan and Illingworth, 2000; Mace and Benson-Troth, 2002; Tian and Curry, 1989), this is in-

terpreted as maximum overlap for non-adjacent cloudy layers, as long as the layers between them are cloudy. However, in most GCMs, this is implemented following Geleyn and Hollingsworth (1979); maximum overlap is applied for clouds in adjacent layers, but the overlap between contiguous clouds in non-adjacent layers is not defined. This overlap is constrained somewhat by the maximum overlap applied to the adjacent layers, but otherwise is random.

Exponential-random overlap, first suggested by Hogan and Illingworth (2000), has been consistently found to fit observations better than maximum-random overlap. In this parametrization the overlap between two cloudy layers is a linear combination of maximum and random overlap, with the proportion of maximum overlap decreasing in proportion to the negative exponent of the distance between the two layers. The rate of the decrease is controlled by the ‘decorrelation length’, which is a parameter that can be parametrized or tuned to give the correct cloud cover. Further studies have confirmed that, for large datasets, the exponential-random overlap parametrization is a good predictor of the decrease in the mean overlap parameter with increasing vertical distance between layers (e.g. Mace and Benson-Troth, 2002; Naud *et al.*, 2008). However it is not clear how well this parametrization approximates individual cases. Note that Hogan and Illingworth (2000) applied this parametrization to vertically continuous clouds only; they found that on average discontinuous clouds tend to be randomly overlapped. However, other studies (e.g. Bergman and Rasch, 2002; Oreopoulos and Khairoutdinov, 2003; Oreopoulos and Norris, 2011) have applied this parametrization without discriminating between contiguous and discontinuous clouds, which has the advantage that the overlap is completely independent of the model vertical resolution.

In this chapter, we use combined CloudSat and Cloud-Aerosol Lidar and Infrared Pathfinder Satellite Observation (CALIPSO) observations to study cloud vertical overlap. Although there are many previous studies of cloud vertical overlap, some of which use CloudSat and CALIPSO observations (e.g. Barker, 2008b; Kato *et al.*, 2010; Shonk *et al.*, 2010), these existing studies have focused on the mean overlap. This analysis considers not only the mean, but also the distribution of cloud overlap.

The observation sources and the manner in which they are combined are described in the following section. In section 4.3, we define a new overlap parameter, which is based on that defined by Hogan and Illingworth (2000), but is more suitable for considering the distribution of

overlap. Section 4.4 shows how horizontal structure affects the distribution of overlap parameters for randomly overlapped clouds. Section 4.5 considers overlap for vertically contiguous cloud layers, while non-contiguous layers are considered in Section 4.6. This analysis suggests some modifications to the exponential-random parametrization of clouds, which are tested in Section 4.7. The implications of this study are discussed in section 4.8.

4.2 OBSERVATIONAL DATA

This study of cloud overlap is based on an amalgam of CloudSat radar (Stephens *et al.*, 2008) and CALIPSO lidar data. These satellites are part of a constellation of satellites known as the ‘A-train’ and fly in sufficiently close proximity for their observations to be combined. The CloudSat radar and the CALIPSO lidar each have complementary strengths; the CloudSat radar can probe optically thick clouds, while the CALIPSO lidar can detect optically thin clouds. The radar observations used in this study are from the GEOPROF cloud mask, while the lidar observations are from the GEOPROF-LIDAR cloud fraction. Both these products are freely available from the CloudSat data processing center website (<http://www.cloudsat.cira.colostate.edu>).

The 2B-GEOPROF cloud mask algorithm is described in detail by Marchand *et al.* (2008). For convenience we summarise the algorithm here. The first step in the production of the cloud mask is the calculation of the mean noise power (the mean power return due to background noise) and its standard deviation using the measured return power from the stratosphere. A first guess cloud mask is then derived by comparing the target power in each vertical range bin to this noise. This mask is not binary; larger values are used to denote more confidence. Next, the observations in a box centred on each point are considered. Assuming that the noise is Gaussian and independent, the probability of the observed cloud configuration arising due to noise is calculated. This is multiplied by the probability of the centre pixel being a false detection. The centre pixel may then be changed to cloudy or clear if the probability is below or above a certain threshold. This box filter is applied several times. The number of times this filtering is applied, size of the box and probability threshold are tunable parameters. Finally, this is repeated with an along-track moving average applied to the raw return power, to improve the detection capability. The previous mask and moving averaged mask are merged by taking the original mask and adding points that are

cloudy in both the new mask and a reduced resolution version of the previous mask. If cloud is detected, the mask is given a value between 20 and 40, with increasing values representing more confidence in the detection.

The 2B-GEOPROF-LIDAR cloud fraction product is described by Mace *et al.* (2009). The basis for this data product is the CALIPSO virtual feature mask (VFM) (Vaughan *et al.*, 2004). ‘Features’ are identified with each profile by comparing backscatter measurements at 532 nm to an adaptive threshold. These features are then classified as either clouds or aerosols according to the feature mean attenuated backscatter at 532 nm and the feature mean total colour ratio (the backscatter at 1064 nm divided by that at 532 nm). Below 8.2 km, the VFM has a horizontal resolution of 330 x 330 m and a vertical resolution of 30 m, so there are potentially 9-10 profiles per CloudSat profile. Above 8.2 km the VFM resolution is 1 km along track, 330 m across track and 75 m in the vertical, so there are potentially 3-4 profiles per CloudSat profile. These CALIPSO cloud detections are then mapped onto CloudSat space and the fraction of lidar volumes within each radar volume is denoted the lidar ‘cloud fraction’.

Each of the 2B-GEOPROF and 2B-GEOPROF-LIDAR profiles measures 1.7 km along track and 1.3 km across track and divides the atmosphere into 125 vertical cells each of which is 240 m thick. Cloud thresholds are chosen following Mace *et al.* (2009); a 2B-GEOPROF cell is considered cloudy if the cloud mask has a value greater than or equal to 20, while a 2B-GEOPROF-LIDAR cell is considered cloudy if the cloud fraction is greater than or equal to 50%. When combining the observations, a cell is considered cloudy if it is cloudy according to *either* of the individual data products. Mace *et al.* (2009) found that this combination of CloudSat and CALIPSO observations showed excellent agreement with airborne remote sensors. Nevertheless not all clouds are detected. For example, Chan and Comiso (2011) showed that some low level, optically and geometrically thin clouds at high latitudes are detected by neither CloudSat nor CALIPSO. In this investigation, we use CloudSat and CALIPSO observations obtained between 22nd December 2007 and 10 January 2008. While there is no break in the availability of the 2B-GEOPROF product between these dates, resulting in almost 10 million radar profiles, two of the 262 2B-GEOPROF-LIDAR ‘granules’ are missing. Where the lidar observations are unavailable, we use the radar observations on their own.

For the purposes of calculating an estimate of the OLR in section 4.7 we use temperature

profiles from another dataset available from the CloudSat website: the CloudSat ECMWF-AUX product. This dataset consists of pressure, temperature and humidity fields from the ECWMF ERA-INTERIM reanalysis (Dee *et al.*, 2011) interpolated onto the CloudSat observations space. For each CloudSat profile, the four surrounding ERA-INTERIM gridboxes are found and linear interpolation is used to attain a temperature for each of these gridboxes at the height of each of the CloudSat layers. Bilinear interpolation is then applied to the 4 temperatures at each height to produce a single temperature for each CloudSat cell.

4.3 OVERLAP PARAMETERS

Based on ground-based radar observations, Hogan and Illingworth (2000) suggested that the combined cloud cover between two layers, C_{tot} could be approximated by a linear combination of the combined cloud given by the maximum and random overlap assumptions (C_{max} and C_{rand} respectively).

$$C_{tot} = \alpha C_{max} + (1 - \alpha) C_{rand}. \quad (4.1)$$

Hence the ‘overlap parameter’, α , that gives the correct observed combined cloud cover is given by

$$\alpha = \frac{C_{tot} - C_{rand}}{C_{max} - C_{rand}}. \quad (4.2)$$

α takes a value of one if the clouds are maximally overlapped. If the combined cloud cover is the same as the expected value for randomly overlapped clouds then α equals zero. Moreover α converges to an average value of zero when sampling from a set of randomly overlapped clouds. For minimum overlap, as has been observed for some pairs of clouds (e.g. Hogan and Illingworth, 2000; Mace and Benson-Troth, 2002) the value taken by α depends on the probability of minimum overlap occurring when the clouds are located randomly within each layer. This means that for minimum overlap α may take any value between zero and minus infinity, with the value depending on the cloud fraction in each layer. Consequently α is not particularly useful for looking at the distribution of cloud overlap.

In order to consider the distribution of cloud overlap we have devised a new overlap parameter, which takes a single value for minimally overlapped clouds. In order to allow us to exploit the significant body of existing literature concerning the α overlap parameter we have defined the new

overlap parameter as similarly as possible. This new overlap parameter, which we shall denote β , is given by

$$\beta = \begin{cases} \alpha & \text{if } \alpha \geq 0; \\ \frac{C_{rand} - C_{tot}}{C_{min} - C_{rand}} & \text{if } \alpha < 0, \end{cases} \quad (4.3)$$

where C_{min} is the combined cloud cover if the cloud in the two layers is minimally overlapped. This new overlap parameter takes a value of one if clouds are maximally overlapped, minus one if they are minimally overlapped and zero if the combined cloud cover is the expected value for randomly overlapped clouds. Hence it is more useful for looking at the distribution of cloud overlap. However, it does not necessarily converge to zero on average for multiple randomly overlapped clouds.

4.4 RANDOM OVERLAP AND HORIZONTAL CLOUD STRUCTURE

In overlap parametrizations that are incorporated directly into radiative transfer solvers, such as that described by Geleyn and Hollingsworth (1979), random overlap is deterministic; the combined cloud fraction for two randomly overlapped layers is equal to the expected combined cloud fraction if they are randomly overlapped. However, if random overlap is applied stochastically as is becoming more common as GCMs adopt stochastic cloud generators (e.g. Hill *et al.*, 2011) such as that described by Räisänen *et al.* (2004), a distribution of combined cloud fractions and hence overlap parameters will arise. In this section we shall use randomly generated pairs of cloudy layers to examine the distribution of overlap parameters that arise from random overlap for comparison to the observed distributions of overlap parameters that we shall show in sections 4.5 and 4.6.

Figures 4.1 and 4.2 show the distribution of overlap parameters calculated for gridboxes containing 25 and 200 profiles (42.5 km and 340 km in length) respectively. These distributions were calculated based on a uniform distribution of cloud fractions between 0.04 and 0.96 (overlap is not defined for cloud fractions of zero or one) with no correlation between the cloud fraction in each layer (i.e. cloud fractions in each pair of layers were chosen so that every possible combina-

tion occurred equally frequently). Note that cloud fractions of one and zero are not included as β is not defined in either case.

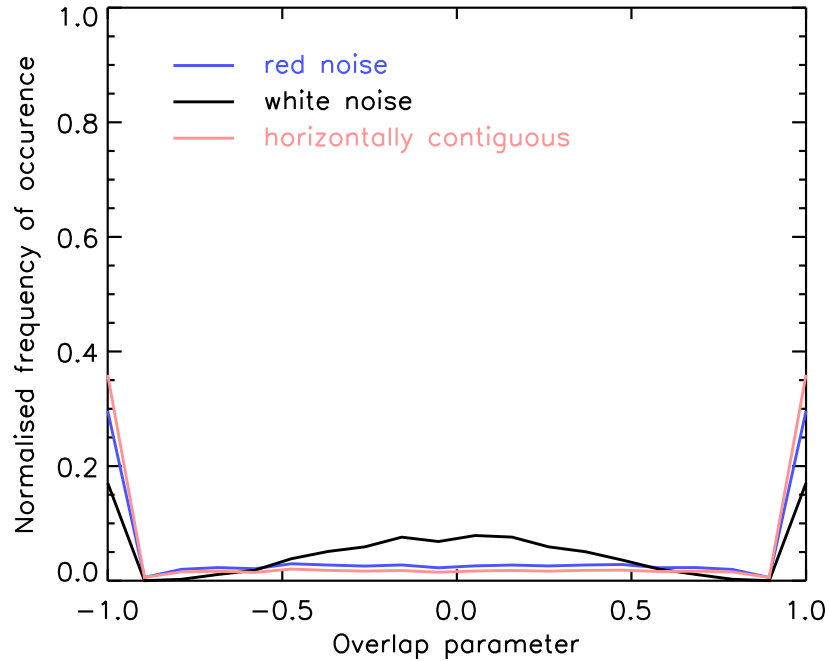


Figure 4.1 Distribution of the beta overlap parameter for randomly overlapped clouds, for grid-boxes containing 25 cells. The different coloured lines denote clouds with different horizontal structure applied; the black line denotes clouds with no horizontal structure (the underlying random numbers which determines which cells are cloudy is white noise), the red line denotes horizontally contiguous clouds, while the blue line denotes the case when the underlying random numbers are red noise.

The black lines in Figures 4.1 and 4.2 show the distribution of overlap parameters that arise when the cloudy cells in each layer are chosen at random. In practice, this was achieved by taking a random sample from a uniform distribution for each cell in each layer and setting the cell as cloudy if this random number was below a certain threshold, where the threshold is chosen separately for each layer to ensure the required number of cells in each layer are cloudy. Thus the underlying random numbers are white noise. This is the distribution of overlap parameters that will arise when clouds are randomly overlapped in the cloud generator of Räisänen *et al.* (2004). The distribution is symmetric and trimodal, with local maxima at minus one, zero and one. The

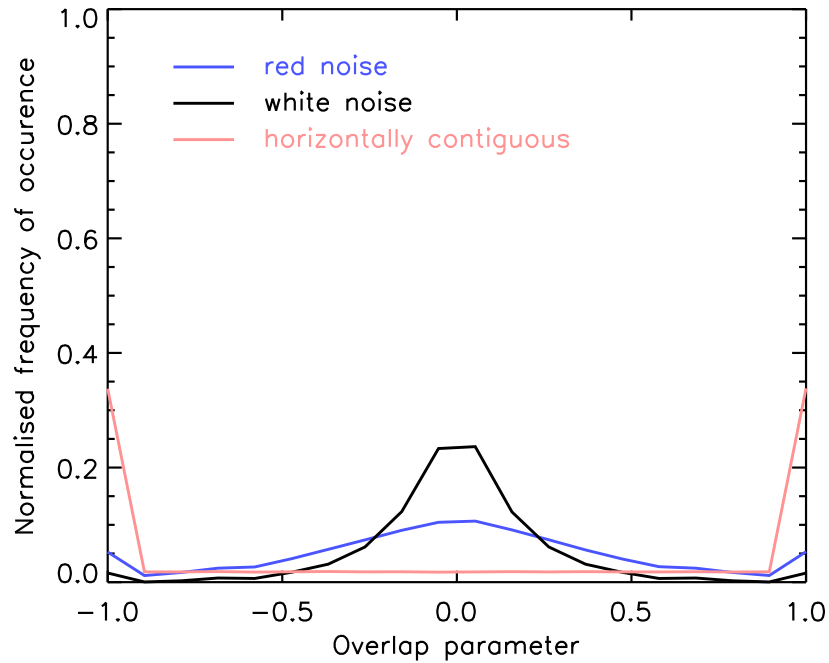


Figure 4.2 As Figure 4.1, but for gridboxes containing 200 cells.

relative magnitude of these modes depends on the number of cells used in the calculation and are quite different for 25 and 200 cells. The distribution of overlap parameters also depends on the distribution of cloud fractions. When the cloud fractions in both layers are small, random overlap is more likely to lead to apparent minimum overlap, as is the case if the cloud fractions in both layers are large. On the other hand, if the cloud fraction is large in one layer and small in the other, then random overlap is more likely to lead to apparent maximum overlap.

The pale red lines in Figures 4.1 and 4.2 show the distribution of overlap parameters when the cloudy cells in each layer are horizontally contiguous. These distributions are bimodal, with peaks at minus one and one, but no peak at zero. The blue lines show the distribution of overlap parameters when red noise is used for the random number in each layer, which means that cloudy cells tend to be grouped together, but may be separated by clear cells. In practice the set of random numbers x_i , that determines which cells are cloudy was calculated for each layer as follows

$$\begin{aligned}
 x_0 &= y_0 \\
 x_{i+1} &= Ax_i + (1 - A)y_i
 \end{aligned}
 \tag{4.4}$$

where y is a set of independent random numbers, and $A \in [0, 1]$ is a constant, which was set to 0.9 to produce the distributions shown in Figures 4.1 and 4.2. Unsurprisingly, this distribution lies somewhere between the horizontally contiguous and horizontally independent cases.

Figures 4.1 and 4.2 show that the expected distribution of overlap parameters for randomly overlapped clouds is highly dependent on the horizontal structure of the cloud in each layer. They also highlight that both maximum and minimum overlap are likely to arise as a result of random overlap, with the likelihood dependent on the horizontal cloud structure in each layer.

4.5 OVERLAP FOR VERTICALLY CONTIGUOUS CLOUDS

As discussed in the introduction there are both advantages and disadvantages to separating vertically contiguous and discontinuous clouds when parametrizing cloud overlap. As the mean overlap is different for contiguous and discontinuous clouds, it is easier to both identify and explain any changes to the overlap when they are considered independently. As a result, we have chosen to separate them in this analysis.

In this section we shall use combined CloudSat and CALIPSO observations to consider the distribution of the new overlap parameter β for vertically contiguous clouds. To facilitate comparison with other studies, we also compute the mean value of the α overlap parameter. In this analysis, we use the GCM definition of vertically contiguous (i.e. that there are no completely clear layers between the cloud layers). Thus it is possible for two cloud layers to be ‘contiguous’ even if there are no individual clouds that extend continuously between the two layers.

The overlap parameters discussed in the remainder of this chapter were computed as follows. First we split each layer of the data into continuous ‘gridboxes’ each containing the same number of observed profiles. We then searched for error indicators in each gridbox and considered only the layers above the highest layer containing an error. Following the conventions explained in section 4.2 we determined whether each cell in each column was cloudy or not and deduced a cloud fraction for each layer by dividing the number of cloudy cells by the gridbox size. We then calculated a β overlap parameter for each pair of cloudy layers in the gridbox. Overcast layers were not included in the calculations, as the overlap parameter is undefined.

Figure 4.3 shows the mean and distribution of the β overlap parameter as a function of distance between layers for vertically contiguous clouds, for gridboxes containing 25 cells (i.e. 32.5km long). The solid line shows the mean value of β . For comparison, the dashed line shows the mean value of the α overlap parameter, calculated as in Hogan and Illingworth (2000) (i.e. equation 4.2 was applied to the mean observed maximum and random cloud fractions). This estimate of α is similar to that for β and, as in the existing literature (e.g. Hogan and Illingworth, 2000; Mace and Benson-Troth, 2002), it decreases from one to zero with distance between layers, similarly to an inverse exponential function. The shading denotes the proportion of the gridboxes separated by the given distance for which the value of β is within the given interval. Most clouds appear to obey either maximum or minimum overlap and clouds only occasionally exhibit overlap between these extremes. Although the exponential-random overlap parametrization of Hogan and Illingworth (2000) does not explicitly allow for minimum overlap, we have already seen in Figures 4.1 and 4.2 that if the clouds are horizontally contiguous, applying random overlap stochastically can lead to a large frequency of apparent minimum overlap. Thus for cloud layers sufficiently far apart, random overlap can perhaps be used to explain the observed distribution. However, the lack of intermediate values of β (i.e. values between one and minus one) implies that in individual columns the overlap changes more abruptly than the gradual decrease implied by exponential-random overlap, which is only applicable to the mean overlap parameter.

Estimates of cloud overlap are rather sensitive to the presence of precipitation (e.g. Barker, 2008a). To examine how precipitation affects the calculation of the overlap parameter, gridboxes containing columns with radar reflectivity (Z) larger than -15 dBZe were removed from the dataset. While this should completely remove the effect of precipitation, it will also remove many of the thicker clouds which produce precipitation. Consequently, the true cloud overlap parameter is likely to lie between the values calculated with and without precipitation. Figure 4.4 is as Figure 4.3 except that precipitation is excluded as described above. As expected, there are fewer occurrences of maximum overlap and the mean overlap parameter decreases much more quickly. The results are also considerably noisier, simply because fewer gridboxes remain. However, the general conclusions drawn for Figure 4.3 remain valid. Figure 4.5 shows the mean overlap parameter as a function of distance between layers for several gridbox sizes with and without precipitation. The difference between the mean overlap parameters with and without precipitation remains consistent across the gridbox sizes considered.

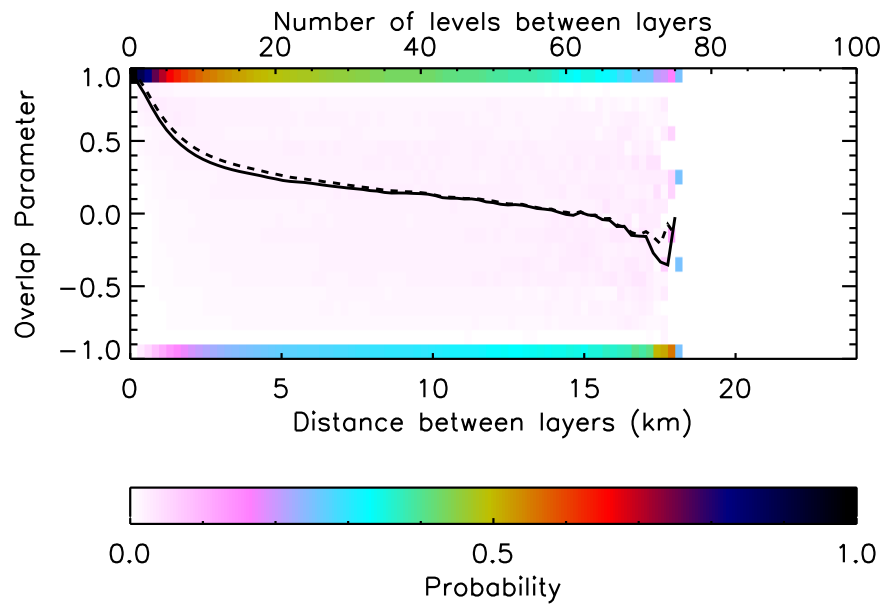


Figure 4.3 Mean values of β and α as a function of distance between layers (solid black and dotted black lines respectively), for contiguous clouds. The shading denotes the probability of β being within the given bin for layers separated by the given distance.

Figure 4.5 also illustrates that the gridbox size has little effect on the mean overlap parameter (whether or not ‘precipitating’ clouds are included), which is consistent with the findings of Barker (2008a). This suggests that the apparent relationship between overlap and horizontal gridbox size found by Hogan and Illingworth (2000) may be solely due to temporal changes in the cloud.

These results suggest more maximally overlapped clouds and correspondingly larger decorrelation lengths than Barker (2008a) found using combined CloudSat and CALIPSO data. This is probably due to the different criteria used to identify cloudy pixels. Barker (2008a) required that the radar reflectivity was greater than or equal to -30 dBZe and both the lidar and the radar identified a pixel as cloudy. As the lidar cannot probe optically thick clouds, this means that many maximally overlapped geometrically thick clouds are not included in Barker (2008a), but are included here.

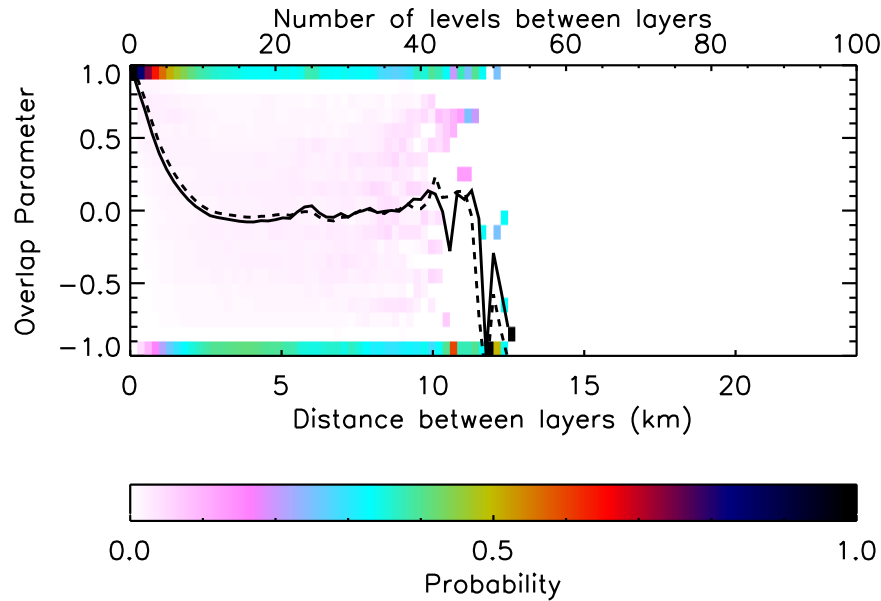


Figure 4.4 Mean values of β and α as a function of distance between layers (solid black and dotted black lines respectively), for contiguous clouds, where precipitation is screened by removing gridboxes containing columns with $Z > -15$ dBZe. The shading denotes the probability of β being within the given bin for layers separated by the given distance.

The uncertainty in the decorrelation length due to precipitation means that a quantitative analysis of overlap is unlikely to be very helpful. The analysis described in the rest of this chapter was applied to the observations both with and without precipitation and the general qualitative conclusions are applicable to both datasets. However, for succinctness, we shall focus on “precipitation-free” data in the remainder of this chapter.

4.6 OVERLAP FOR CLOUDS SEPARATED BY CLEAR LAYERS

In numerous observational studies (e.g. Tian and Curry, 1989; Hogan and Illingworth, 2000; Willén *et al.*, 2005; Naud *et al.*, 2008), the overlap between clouds separated by clear layers have been found to be approximately random, regardless of the vertical distance between them. This

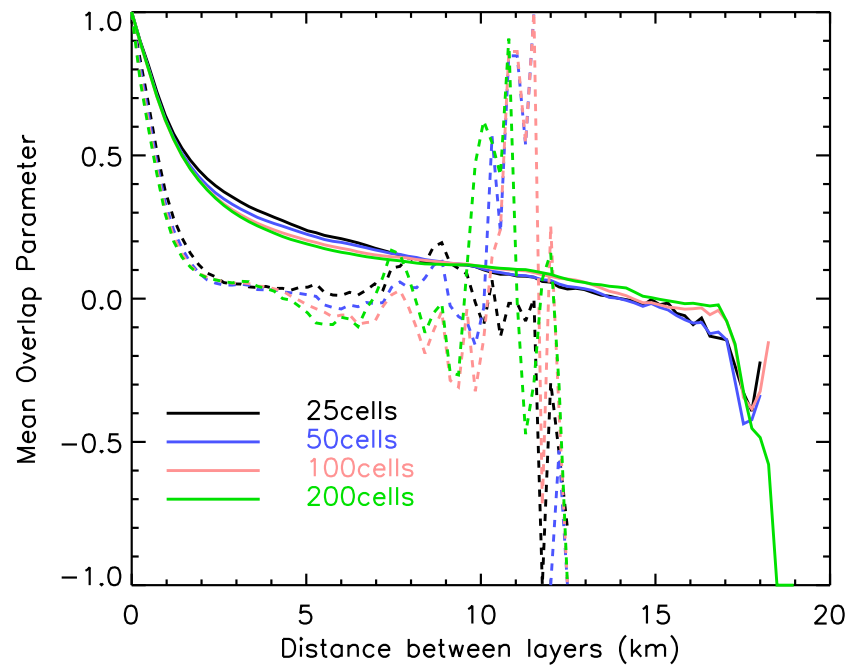


Figure 4.5 Mean values of the β overlap parameter as a function of distance between the layers. The dashed lines show the overlap when the data has been filtered to remove precipitating gridboxes, as explained in the text, while the solid lines show the overlap for the unfiltered data. The correspond to gridboxes containing 25,50,100 and 200 columns respectively.

is thought to be because such clouds are essentially independent. In this section, we consider the observed overlap for these vertically discontinuous clouds.

Overlap parameters for clouds separated by clear-sky, for gridboxes containing 25 cells (32.5 km long), excluding ‘precipitating’ gridboxes, are shown in Figure 4.6, which has the same format as Figure 4.4. The mean values of β and α are close to zero for all vertical separations, but as in the vertically contiguous case, individual clouds tend to be either maximally or minimally overlapped. The β parameter suggests that minimum overlap is slightly more common than maximum, particularly for small vertical separations, which leads to a mean value that is less than zero. This is because the distribution of cloud fractions is not uniform. The alpha parameter does not have this problem.

The solid lines in Figure 4.7 show the observed distributions of the beta overlap parameter for

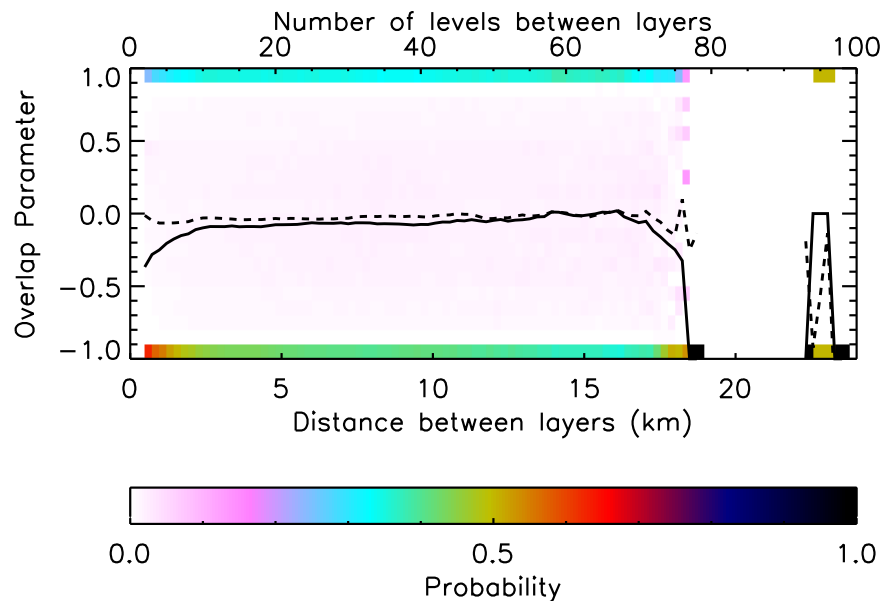


Figure 4.6 Mean values of β and α as a function of distance between layers (solid black and dotted black lines respectively), for discontinuous clouds, where precipitation is screened by removing gridboxes containing columns with $Z > -15$ dBZe. The shading denotes the probability of β being within the given bin for layers separated by the given distance.

gridboxes containing 25 and 200 cells, for cloudy layers that are any vertical distance apart and separated by clear layers. For the larger gridbox, the distribution is skewed towards minimum overlap. This is because small cloud fractions become more frequent and pairs of layers containing small cloud fractions that are randomly overlapped are more likely to exhibit minimum overlap. The frequency of intermediate values of β also increases with increasing gridbox size, in agreement with the difference between Figures 4.1 and 4.2 for non-horizontally contiguous clouds. The dashed lines show the distributions of overlap parameters that are obtained by taking each pair of observed cloudy layers and randomly overlapping them whilst maintaining the observed horizontal cloud structure. In practice this was achieved by moving each of the cells in the bottom layer to the right by the same random number, with the cells reappearing on the far left of the row when they were moved to the right of last cell in the row. These distributions match the observed distributions very well, which implies that if the horizontal cloud structure is correct,

it is possible to model the observed overlap distribution for discontinuous clouds using random overlap.

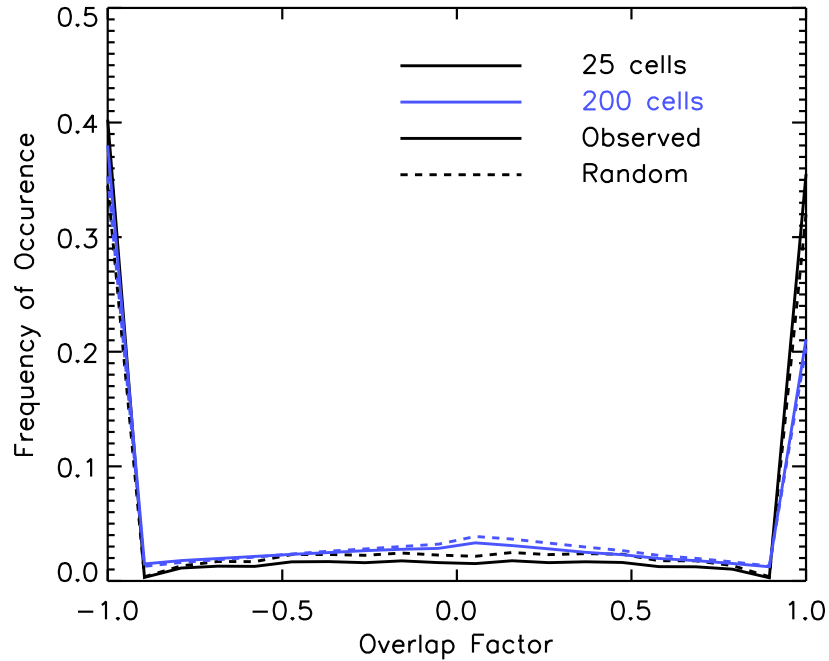


Figure 4.7 Distribution of β for discontinuous clouds. Solid lines denote the observed distribution. The dashed lines show the distribution obtained if the clouds in each layer are randomly overlapped, while the observed horizontal structure is maintained. The different lines colours correspond to different gridbox sizes as indicated by the key.

4.7 OVERLAP PARAMETRIZATIONS

The preceding sections have shown that individual clouds tend to be either maximally or minimally overlapped and that this behaviour can arise from random overlap with the correct horizontal cloud structure. In this section, we suggest and test some modifications to the overlap parametrization. The modified overlap parametrizations are implemented in a stochastic cloud generator and used to generate cloud fields which are compared to the observed cloud fields. First we compare these modified parametrizations to the observations in terms of the mean and distributions of beta. We then consider the effects on estimates of the total cloud cover and OLR.

To test changes to the overlap parametrization we used a version of the stochastic cloud generator described by Räisänen *et al.* (2004). This generator can produce any number of sub-columns; as the number of sub-columns is increased, the overlap between any two layers converges to its expected (i.e. input) value. To minimise differences due to noise in the generated cloud fields, the number of sub-columns was set to 4000. This is many more sub-columns than the 100 or so that are typically generated in GCMs (e.g. Walters *et al.*, 2011), which will lead to narrower generated distributions of overlap parameters (Compare Figures 4.1 and 4.2). The cloud generator was modified to allow it to produce cloud fields according to the overlap parametrizations defined below. An example of the cloud field resulting from each parametrization is shown in Figure 4.8. Note the similarity between these examples, which highlights the quasi-deterministic nature of the cloud generator when 4000 sub-columns are produced. The overlap parametrizations are as follows:

- (a) Geleyn maximum-random overlap: The version of maximum-random overlap described by Geleyn and Hollingsworth (1979), where maximum overlap is applied to adjacent cloud layers only and not to contiguous clouds. The overlap between non-adjacent contiguous clouds that is not constrained to be maximum by the overlap between the adjacent pairs of layers is random. Cloud horizontal structure is random. We shall denote this max-rand.
- (b) Exponential-random overlap: As introduced by Hogan and Illingworth (2000); the overlap between clouds in contiguously cloudy layers is a linear combination of maximum and random overlap, becoming increasingly random as the distance between the layers increases. Clouds separated by clear layers are randomly overlapped. Again, cloud horizontal structure is random. We shall denote this exp-rand-A.
- (c) Geleyn exponential-random overlap: As exponential-random overlap above, but only adjacent layers are exponentially overlapped. As for Geleyn maximum-random overlap, the overlap between clouds in non-adjacent contiguously cloudy layers is random when not constrained by the overlap assumptions between adjacent layers. This results in slightly more random overlap between contiguous non-adjacent layers, which is particularly evident when comparing the overlap between the fifth and seventh layers in Figure 4.8 (b) and (c). This parametrization is included because it is how exponential-random overlap is realised when

incorporated directly into a radiative transfer solver. As for max-rand and exp-rand-A, cloud horizontal structure is random. We shall denote this exp-rand-B.

- (d) Horizontally-contiguous exponential-random overlap: As exp-rand-A, but the cloudy cells in each layer are assumed to be horizontally contiguous (i.e. all the cloudy cells in each layer are adjacent) and the switch from maximum to random overlap is applied to whole layers α of the time rather than to a fraction α of every pair of layers. We shall denote this exp-rand-C. Note that this parametrization preserves the stochastic element of the generator as the number of sub-columns is increased (i.e irrespective of the number of sub-columns, there are numerous different possible cloud fields).

It should be noted here that the implementation of maximum-random overlap is slightly different to that described by Räisänen *et al.* (2004). Räisänen *et al.* (2004) generates a new random number if the cell above is cloudy, multiplying it by the clear-sky fraction to ensure it remains clear if the cloud fraction does not change. Consequently cloudy layers separated by layers with smaller cloud fractions are not maximally overlapped (cf layers 5 and 7 in Figure 4.8 (a)), but cloudy layer separated by layers with larger clouds fractions *are* (incorrectly) maximally overlapped. We have fixed this by generating a new random number if the cell above is cloudy, scaling this random number to ensure that the cell will remain cloudy if the cloud fraction does not change. Thus cloudy layers separated by layers with larger cloud fractions are not maximally overlapped (cf layers 1 and 3 in Figure 4.8 (a)). This means that the overlap between cloudy layers that are contiguous but non-adjacent is exactly as in the Geleyn and Hollingsworth (1979) parametrization. The Geleyn-style parametrizations mimics the overlap behaviour in a GCM that incorporates the overlap assumptions into the radiative transfer solver.

To test the various overlap parametrizations described above, the combined CloudSat-CALIPSO cloud mask was again divided into gridboxes. Within each gridbox the cloud fraction for each layer was calculated and the profile of cloud fractions was passed to the cloud generator, which generated 4000 sub-columns for each gridbox for each overlap parametrization. The decorrelation lengths passed to the generator were chosen to minimise the total cloud cover bias for the exp-rand-A case. Beta overlap parameters were then calculated as described in Section 4.5 for the observations and each overlap parametrization.

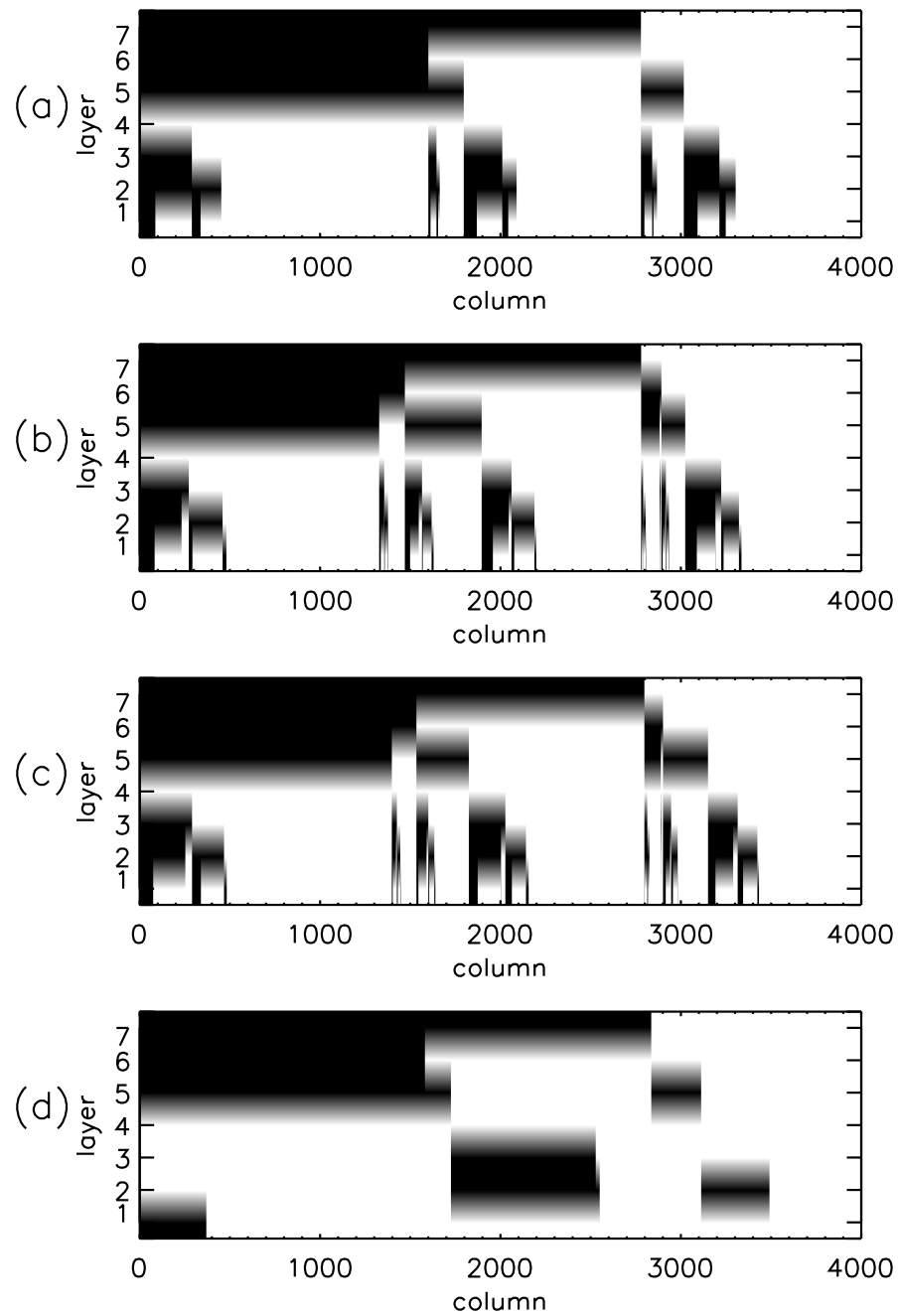


Figure 4.8 Example of the cloud field generated by each of the overlap parametrizations. (a) shows Geleyn maximum-random overlap, (b) shows exponential-random overlap, (c) shows Geleyn-exponential-random overlap and (d) shows horizontally-contiguous exponential-random overlap. Each of these overlap parametrizations is defined in the text. Clouds are left justified, beginning with the top layer. The input layer cloud fractions were (from top to bottom) 0.7, 0.4, 0.5, 0.0, 0.2, 0.3 and 0.1.

4.7.1 COMPARISON OF OBSERVED AND PARAMETRIZED β

Figures 4.9 and 4.10 show the mean value of the beta overlap parameter for gridboxes containing 25 and 200 observed profiles respectively. As for the various exponential-random overlap parametrizations, the Geleyn-maximum-random overlap parametrization decreases exponentially, the main difference being that the decrease is offset by one layer. This is very different behaviour to the version of maximum-random overlap where all contiguous clouds are maximally overlapped. For exponential-random overlap, the difference between applying overlap to contiguous layers or just to adjacent layers (i.e the difference between exp-rand-A and exp-rand-B) is smaller than for maximum-random overlap. Exp-rand-B and exp-rand-C give the best matches to the mean overlap.

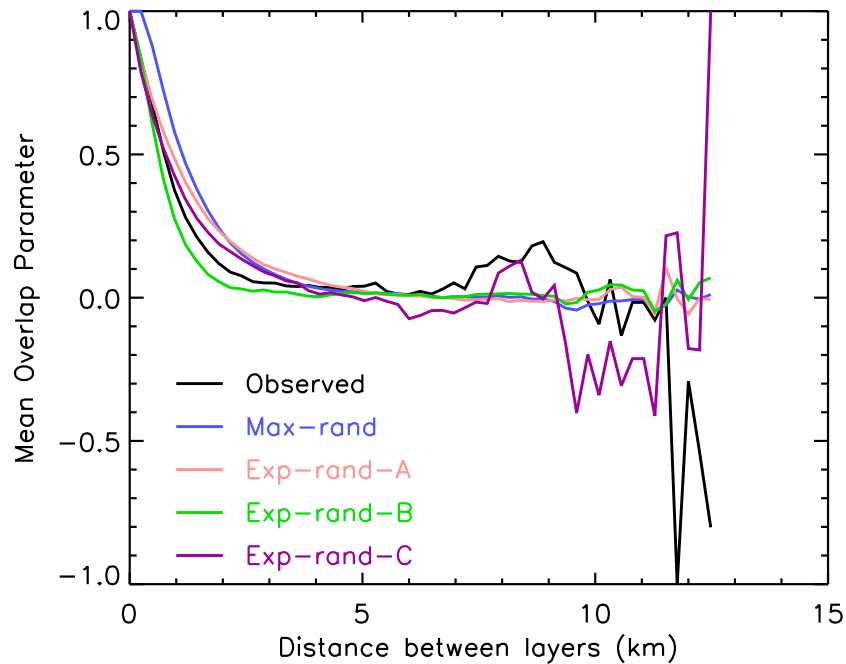


Figure 4.9 Mean value of β as a function of distance between the layers. The different lines colours correspond to different overlap parametrizations, as indicated by the key.

Figure 4.11 shows the distribution of β for adjacent cloudy layers for gridboxes containing 25 profiles. The observed distribution is shown by the black line, while maximum-random overlap is shown in blue. The two versions of exponential-random overlap that assume there is no cor-

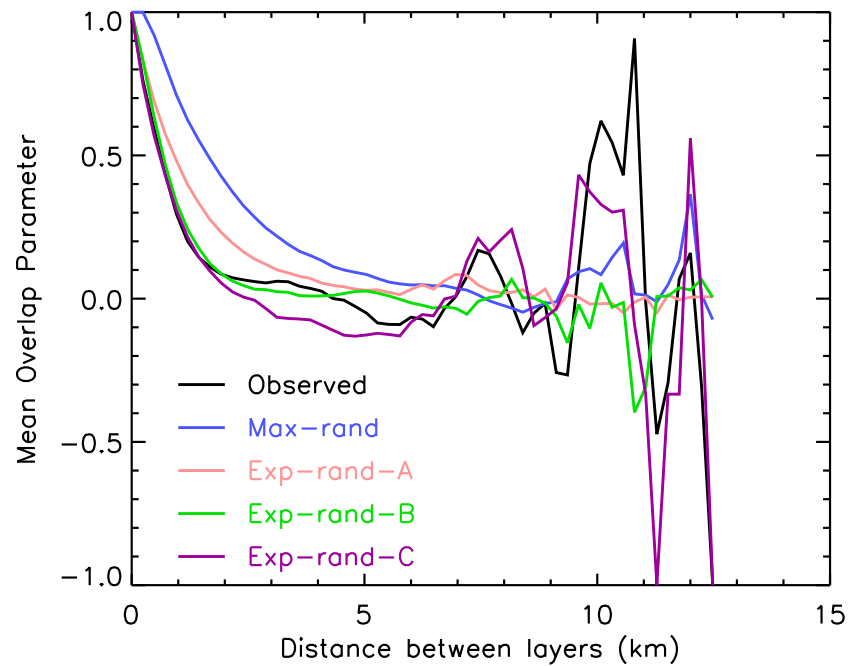


Figure 4.10 As Figure 4.9, but for gridboxes containing 200 columns.

relation between the horizontal location of cloudy cells, shown by the pale red and green lines, have narrow distributions with modes at the value of the overlap parameter given by the decorrelation length. As a comparison of Figures 4.1 and 4.2 illustrates, the width of these distributions is a function of the number of generated cells; the distribution converges to a delta function as the number of cells approaches infinity. The purple line shows the horizontally contiguous parametrization, which matches the observed distribution of β very well; slight overestimates of the frequency of maximum and minimum overlap correspond to underestimates of the frequency of intermediate values. This could probably be improved by a better estimate of the horizontal cloud structure.

As gridbox size is increased to 200 cells, as shown in Figure 4.12, the frequency of observed intermediate values of the overlap parameter increases, with corresponding decreases in the frequency of maximum and minimum overlap. However, the shape of the distribution is quite different to that for exp-rand-A and exp-rand-B, with the frequency increasing as the magnitude of the overlap parameter is increased. Analysis of some randomly chosen cases where the overlap

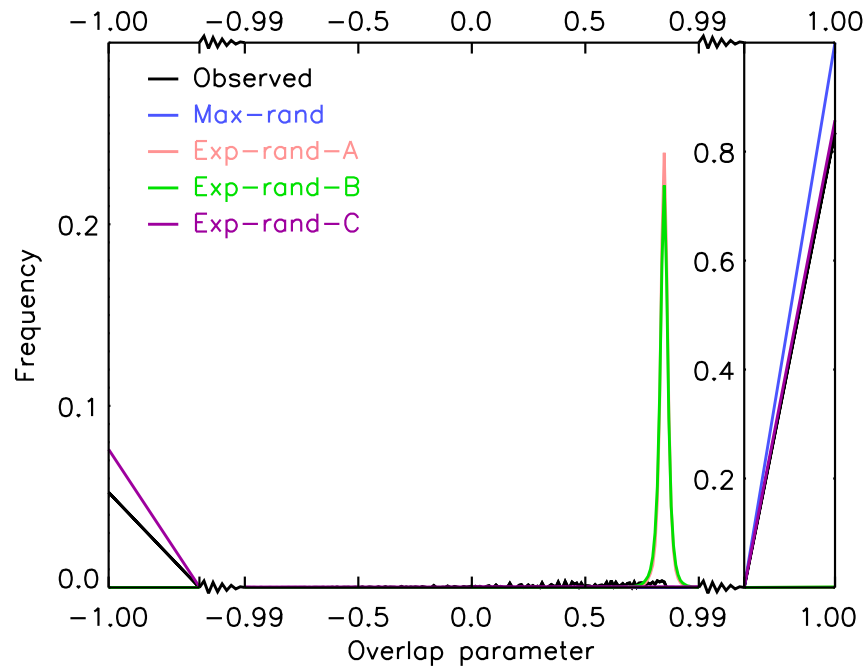


Figure 4.11 The distribution of the beta overlap parameter for adjacent cloudy layers for observed gridboxes that contain 25 columns. Note that the axes are not continuous. The line colours denote the various overlap parametrizations, as indicated by the key. Overcast layers are not included.

parameter takes a value between 0.9 and 1.0 suggests that this is usually due to the presence of multiple clouds in the gridbox; each individual cloud obeys maximum overlap, but the combined overlap parameter is less than one due to the overlap between distinct clouds, which is minimum by definition. However, we have not analysed the statistics of the whole data set to confirm this theory.

The mean β overlap parameters for discontinuous clouds are shown in Figure 4.13 as a function of distance between layers. The observed values, shown by the black line tend to have a mean value less than zero, particularly for small layer separations. This is also evident (to a smaller extent) in Figure 4.6 and is due to the distribution of cloud fractions being non-uniform. All three overlap parametrizations where clouds have no horizontal structure (max-rand, exp-rand-A, exp-rand-B) tend to overestimate the mean overlap parameter, with values much closer to zero. However, when the clouds are horizontally contiguous as in exp-rand-C, the mean overlap

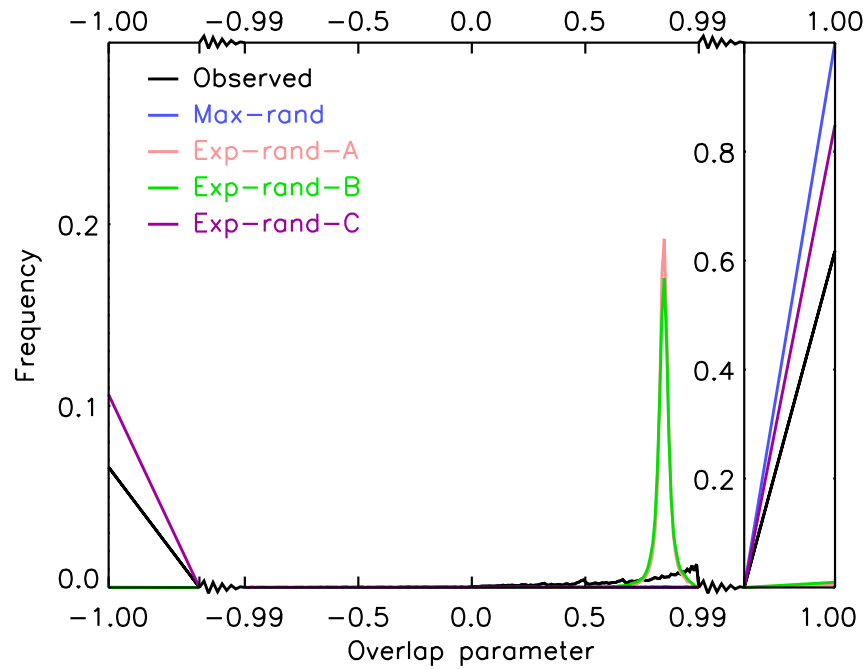


Figure 4.12 As Figure 4.11, but the observed gridboxes contain 200 columns.

parameter is much closer to the observed value.

Figure 4.14 shows the distributions of the overlap parameter that result in the mean values shown in Figure 4.13. The observed distribution, again shown by the black line shows peaks corresponding to maximum and minimum overlap, as was previously shown for various different gridbox sizes in Figure 4.7. Intermediate values are reasonably common at this scale; while the frequency of any individual intermediate value is small, around 30% of the cases are neither maximum nor minimum. The three overlap parametrizations where clouds have no horizontal structure have similar distributions, with modes around zero. The exp-rand-C parametrization is a better match to the observations, with peaks at maximum and minimum overlap. However, the frequency of each of these is overestimated.

Clearly the best performing parametrization in terms of predicting the mean and distribution of the cloud overlap parameter is exp-rand-C. As we have already noted, this parametrization could probably be further improved by applying a horizontal cloud structure that better matches the observed structure.

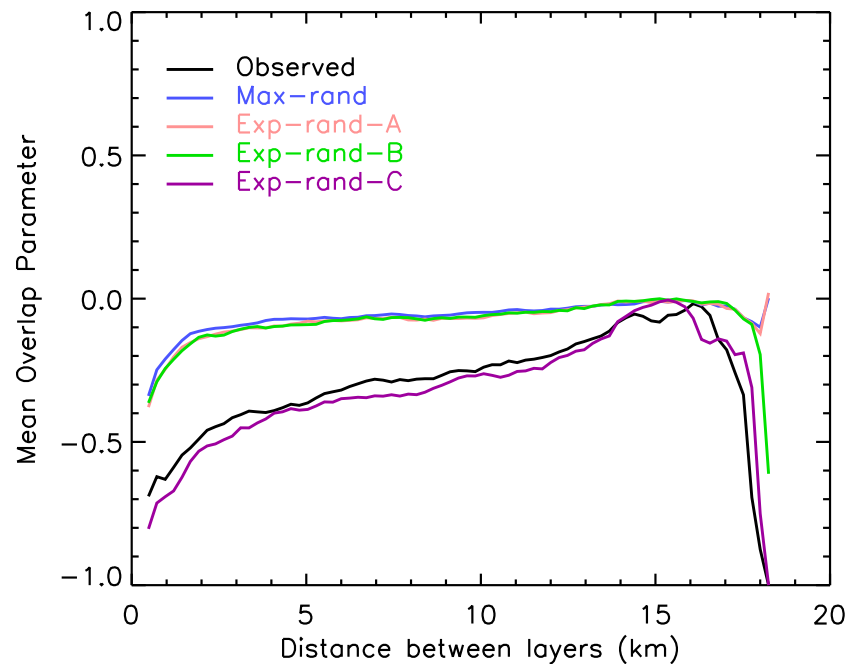


Figure 4.13 Mean β overlap parameter as a function of distance between layers for discontinuous clouds in gridboxes containing 200 columns. The line colours correspond to the different overlap parametrizations, as indicated by the key.

4.7.2 EFFECT ON TOTAL CLOUD COVER AND OLR

While an analysis of the overlap parameters is informative, overlap parameters are not relevant in themselves. The introduction to this chapter contains a discussion of the variables that may be influenced by the overlap parametrization; this section focuses on the effect it has on total cloud cover (which strongly influences the SW surface irradiance) and OLR.

The total cloud cover for each parametrization is shown in Table 4.1. Note that this is calculated for cloudy gridboxes only, which is why it decreases with increasing gridbox size. As found in previous studies (e.g. Willén *et al.*, 2005), maximum-random overlap leads to a slight underestimate of the total cloud cover. Although the decorrelation length was chosen to give correct total cloud cover for the exp-rand-A case, all the exponential-random overlap parametrizations give very good estimates of the total cloud cover, despite the differences in the mean overlap

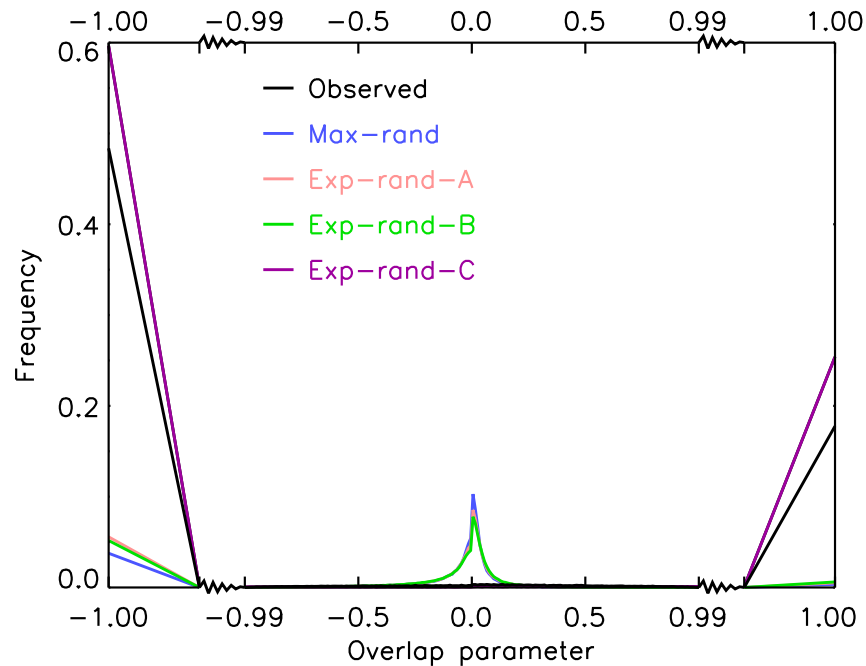


Figure 4.14 Distribution of beta overlap parameter for discontinuous clouds in gridboxes containing 200 columns. Note that in order to ensure the differences at minus one and one are clear, the horizontal axis is not continuous. The line colours correspond to the different overlap parametrizations, as indicated by the key.

parameter shown in Figures 4.9 and 4.10.

Table 4.2 shows mean absolute total cloud cover errors. These are generally quite small, which is due in part to the inclusion of overcast layers in the calculation. The max-rand, exp-rand-A and exp-rand-B parametrizations perform similarly well. The exp-rand-C parametrization gives slightly larger errors. This is due to the occurrence of intermediate overlap parameters in the observations; if the observations were always either maximum or minimum overlap, the errors would be the same for exp-rand-A and exp-rand-C. However when the intermediate values occur the errors are smaller for exp-rand-A.

To estimate the effect of the various overlap parametrizations on OLR, we calculated the OLR for each observed and generated gridbox using the following method. First, the temperature of each layer in each profile was extracted from the ECMWF-AUX dataset. This was used to

Overlap Param.	Profiles/gridbox (gridbox size (km))			
	25(42.5)	50(85)	100(170)	200(340)
Observed	0.68	0.60	0.52	0.44
max-rand	0.67	0.57	0.48	0.40
exp-rand-A	0.69	0.60	0.52	0.44
exp-rand-B	0.69	0.60	0.52	0.44
exp-rand-C	0.69	0.60	0.52	0.44

Table 4.1 Total cloud fraction for the observations and each of the overlap parametrizations. Note that only cloudy gridboxes were included in the calculation, which is why the values decrease as gridbox size increases.

Overlap Param.	Profiles/gridbox (gridbox size (km))			
	25(42.5)	50(85)	100(170)	200(340)
max-rand	0.02	0.03	0.04	0.05
exp-rand-A	0.03	0.03	0.04	0.04
exp-rand-B	0.03	0.03	0.04	0.04
exp-rand-C	0.03	0.04	0.05	0.06

Table 4.2 Total cloud fraction absolute error for each of the overlap parametrizations.

calculate the mean temperature in each layer of the gridbox. Next, the highest cloudy layer in each observed profile and generated sub-column was identified. The OLR for the profile/sub-column was then calculated using the Stefan-Boltzmann law and the layer mean temperature, under the assumption that the cloud in that layer is a black body. Where the profile/sub-column was cloud-free, the OLR was calculated using the surface temperature. Finally, the OLR was averaged across the profiles/sub-columns, resulting in a single estimate of the mean OLR in each observed and generated gridbox.

The mean OLR estimates are shown in Table 4.3. The OLR increases with gridbox size, due to the decrease in total cloud fraction with gridbox size shown in Table 4.1, with the observed mean values ranging from 270 Wm^{-2} to 291 Wm^{-2} . These estimates are very simple and overestimate the effect of clouds while ignoring all the greenhouse gases which reduce OLR. However, they

allow us to at least make a qualitative comparison between the different overlap parametrizations.

As a consequence of underestimating the mean total cloud cover, as shown in Table 4.1, the max-rand parametrization overestimates the mean OLR. On the other hand, despite their accurate predictions of the mean total cloud cover, each of the exp-rand parametrizations underestimates the OLR by a larger margin. These underestimates imply that the clouds emitting the radiation are too cold, which means that there is too much high cloud exposed to space. This could be corrected by applying a smaller decorrelation length for high clouds, which is consistent with the findings of Barker (2008b). The differences in OLR between the max-rand and exp-rand parametrizations are similar in magnitude to those that can be inferred from the cloud-forcing values obtained by Shonk and Hogan (2010).

Overlap Param.	Profiles/gridbox (gridbox size (km))			
	25(42.5)	50(85)	100(170)	200(340)
Observed	270	281	287	291
max-rand	271	282	289	293
exp-rand-A	269	279	284	287
exp-rand-B	268	278	284	287
exp-rand-C	269	279	284	287

Table 4.3 Mean estimated OLR (Wm^{-2}) for the observations and each of the overlap parametrizations. OLR was estimated from the cloud profile and the temperature of each layer, as explained in the text.

The mean absolute OLR errors are shown in Table 4.4 and are smallest for maximum-random overlap. This can be explained by considering Figure 4.12; for adjacent cloudy layers, the maximum overlap assumption used in max-rand is correct 95% of the time. The exp-rand-A and exp-rand-B parametrizations lead to smaller mean absolute OLR errors than exp-rand-C. This is because exp-rand-A and exp-rand-B lead to small amounts of cloud exposed to space (and hence contributing to OLR) in many layers, which can lead to a cancellation of errors when contributions from clouds that are too high and cold and clouds that are too low and warm are combined. Exp-rand-C will tend to have larger cloud fractions exposed to space in fewer layers, which Figure 4.12 implies is similar to the observations. However, the layers containing the cloud that is

exposed to space will not be correct, resulting in larger OLR errors.

Overlap Param.	Profiles/gridbox (gridbox size (km))			
	25(42.5)	50(85)	100(170)	200(340)
max-rand	1.3	1.8	2.5	3.4
exp-rand-A	2.5	3.5	4.6	5.7
exp-rand-B	2.5	3.5	4.6	5.7
exp-rand-C	3.0	4.2	5.7	7.1

Table 4.4 Mean OLR absolute error (Wm^{-2}) for each of the overlap parametrizations, calculated as described in the text.

The exp-rand-C parametrization, which performed best in terms of predicting the mean and distribution of β , is the worst performing parametrization in terms of OLR and has the largest mean absolute total cloud fraction errors. A better representation of horizontal cloud structure should improve these results. Alternatively, it may be possible to predict where the shift from maximum to random overlap should occur.

As mentioned in the introduction, the overlap parametrization can also affect the vertical heating rate profiles. However, we have not considered heating rates in this study. There are two reasons for this; firstly, heating rates are not as easy to estimate without performing computationally expensive radiative transfer calculations. Secondly, heating rate errors are not relevant themselves, but are important for their impacts on the modelled meteorology, which would require further experiments to estimate. We would expect the observed heating rate profiles to have relatively large heating rates where the overlap goes from maximum to minimum, which would occur in exp-rand-C, but not necessarily in the correct layers. The other overlap parametrizations are expected to have smoother heating rate profiles. The effects of these predicted heating rate errors on the model meteorology are harder to predict.

4.8 CONCLUSIONS

This chapter describes the use of combined CloudSat and CALIPSO data to study cloud overlap. Previous articles on this topic have focused on the mean overlap parameter. This study has also considered the *distribution* of the overlap parameters, leading to the following insights:

- For randomly overlapped clouds, the distribution of overlap parameters is dependent on the cloud horizontal structure.
- Cloud overlap tends to be either maximum or minimum. Intermediate values as predicted by decorrelation lengths occur infrequently.
- Given the correct horizontal cloud structure, random overlap predicts the observed bimodal distribution of overlap parameters for discontinuous clouds.

A stochastic cloud generator based on Räisänen *et al.* (2004) was used to generate clouds according to various different overlap parametrizations. The different parametrizations were then evaluated by comparing the generated clouds to the observed clouds. The overlap parametrization that incorporated the above insights performed best in terms of the mean and distribution of the overlap parameter, but was one of the worst in terms of total cloud fraction and estimated OLR. This highlights the importance of considering the statistics of the impacts in addition to the statistics of the overlap parameters when studying cloud overlap.

The main problem with the CloudSat and CALIPSO data used in this study is the effect that precipitation has on estimates of overlap. As it is difficult to remove precipitation fairly, we cannot draw quantitative conclusions about overlap. The conclusions that we *have* drawn are not sensitive to whether or not we include gridboxes containing possible precipitation. Another problem with using this data is noise in the lidar data during daylight periods, which has been shown to lead to clouds artificially appearing more randomly overlapped during the day (Barker, 2008a). Finally, given the effect of cloud horizontal structure on overlap that has been highlighted by this analysis, it would be useful to examine the cloud size distribution in the CloudSat data to confirm that it is consistent with other observations and models.

This work has shown that the gradual decrease in overlap predicted by the exponential-random parametrization occurs very infrequently. Consequently, future attempts to parametrize cloud overlap in terms of meteorology should focus on estimating the meteorological impacts on overlap parameters or decorrelation lengths derived by considering pairs of cloudy layers rather than decorrelation lengths derived by considering multiple layers concurrently (e.g. Barker, 2008a).

We have shown that cloud horizontal structure can have significant impacts on cloud overlap. Cloud horizontal structure is also important for calculations of cloud erosion (e.g. Morcrette, 2012). Future work will consider observations with the aim of developing a simple model of cloud horizontal structure.

CHAPTER 5:

**THE IMPACT OF CHANGES TO
SUBGRID CLOUD STRUCTURE ON
CLIMATE SIMULATIONS**

5.1 INTRODUCTION

In chapter 3, we described the development of a parametrization of horizontal subgrid-scale ice water content variability, that includes the effects of horizontal and vertical resolution, and cloud fraction. In this chapter we consider the effects of changes to the subgrid-scale cloud structure (in particular the impact of adopting the fractional standard deviation (FSD) parametrization) on 10-year Met Office Unified model (MetUM) climate simulations.

While several experiments have investigated the impact of representing the radiative effects of subgrid-scale water content variability in general circulation models (GCMs) (e.g. Gu *et al.*, 2003; Shonk *et al.*, 2012), they have generally used a constant global value for this variability. As far as we know, there is only one analysis of the sensitivity of a climate model to changes in the distribution of subgrid-scale water content variability (Gu and Liou, 2006). They compared two 5 year simulations, each with a different scaling factor applied to the water content in high clouds before passing to the radiation scheme. Their control used a constant global scaling factor to represent the radiative impact of unresolved water content variability, while the other simulation used a geographically varying annual mean scaling factor derived from International Satellite Cloud Climatology Project (ISCCP) observations described by Rossow *et al.* (2002). Both simulations applied a constant global scaling factor to mid-level and low clouds. As we shall discuss later when comparing our experiment to their results, they found that their scaling factor changes led to changes to the geographical distribution of cloud, with associated changes to the distributions

of precipitation and top of atmosphere (TOA) radiative fluxes.

In the following section, we describe the experiments run to examine the effect of the changes to the subgrid-scale cloud structure. In section 5.3 we present the model FSD climatology that results from the parametrization, explain some of the features, and compare it to the ISCCP based climatology of Rossow *et al.* (2002). Section 5.4 shows the impact of subgrid cloud structure changes on other model fields, with a focus on TOA fluxes. Conclusions are drawn in section 5.5.

5.2 MODEL CONFIGURATION

The simulations discussed in this chapter are based on the GA4.0 configuration of the MetUM (Walters, 2012). The model has a regular latitude-longitude grid, with 192 columns and 145 rows, corresponding to a resolution of around 150 x 150 km in mid-latitudes. There are 85 levels, which decrease in thickness as altitude increases. Sea surface temperatures are prescribed, according to the Operational Sea-surface Temperature and sea Ice Analysis (OSTIA) dataset, which limits the scope of this analysis. In order to ensure that the representation of subgrid cloud structure within each simulation is consistent, the incremental time-stepping scheme (Manners *et al.*, 2009), which is designed to improved the temporal sampling of clouds and assumes maximum-random overlap of homogeneous clouds is switched off.

We shall compare four different climate simulations each run for ten years and three months. We shall consider annual and seasonal means of the final ten years of each simulation. The simulations run were as follows.

- The first experiment uses the default GA4.0 representation of subgrid clouds structure (but without incremental time-stepping as explained above); the FSD of water content is set to 0.75 globally and exponential-random overlap is used with a decorrelation pressure scale of 100 hPa. We shall refer to this experiment as GA4.0.
- The second experiment uses the parametrization of chapter 3 to diagnose an FSD of the cloud water content in each cloudy gridbox. Otherwise it is identical to the first experiment. This will be referred to as FSD param.

- In the third experiment the area-weighted mean FSD of the second experiment, which equals 0.85 is applied globally. This is denoted FSD=0.85
- The fourth experiment assumes that clouds are plane-parallel and horizontally homogeneous and uses the maximum-random overlap parametrization. This experiment does not use the McICA scheme. We shall refer to this as PP-MRO.

For the purposes of model development, the pertinent comparison is between the default GA4.0 and FSD param experiments. However, the other experiments provide more useful data for analysing and understanding the effect of the FSD parametrization, which is the focus of this chapter. The FSD param and FSD=0.85 experiments will be considered in most detail as the difference between them shows the effect of using an FSD parametrization instead of a constant global value. The PP-MRO experiment was run in order to put the other experiments into some context. Changes to the FSD and overlap parametrization have a direct impact on the calculation of radiative fluxes and heating rates, but do not affect other processes directly; changes to other atmospheric properties are due to the radiative changes.

Although the FSD parametrization was derived for ice clouds, it is also applied in these experiments to liquid clouds. Thus there is an assumption that the variability of ice and liquid clouds behave identically. The validity of this assumption is not clear; Oreopoulos and Cahalan (2005) found that ice and liquid cloud water optical depth variability were similar, but Shonk and Hogan (2008) found that water content of ice clouds was more variable (i.e had a larger mean FSD) than liquid clouds.

The CloudSat data used to derive the FSD parametrization consisted of ice water content observations along a *1D* line through each layer of the atmosphere. The model requires an estimate of the FSD for the *2D* domain represented by each cloudy gridbox. To account for this difference, the FSD used in the model is multiplied by a factor of $\sqrt{2}$, a scaling derived by studying the FSD of water content in cloud resolving models (CRMs). Thus the modelled FSD is given by equation 5.1 (cf. equation 3.8), where x is the ‘length’ of the gridbox (calculated as the square root of the area), Δz is the thickness of the layer, and c is the cloud fraction in that layer of the gridbox.

$$\text{FSD} = \begin{cases} (0.41 - 0.07c)(xc)^{1/3} \left[(0.016xc)^{1.10} + 1 \right]^{-0.26} (\Delta z^{0.11}) & \text{if } c < 1; \\ 0.21x^{1/3} \left[(0.016x)^{1.10} + 1 \right]^{-0.26} (\Delta z^{0.11}) & \text{if } c = 1, \end{cases} \quad (5.1)$$

5.3 MODELLED FSD CLIMATOLOGY

Figure 5.1 shows the modelled global distribution of annual mean in-cloud FSD of water content from the FSD param simulation. As mentioned in the previous section, the area-weighted global mean FSD predicted by the parametrization is 0.85 and this is the value used globally in the FSD=0.85 experiment. To highlight the differences between these two experiments, the FSD values shown are differences with respect to 0.85, so that positive (red) values indicate that the mean parametrized values are larger than 0.85 and negative (blue) values indicate that the mean parametrized values are less than 0.85.

The annual mean values of FSD in the FSD param simulation are smaller at very high latitudes. This is due to the regular longitude/latitude grid used in the model; as the lines of longitude converge at high latitudes, the gridbox area decreases, leading to the decrease in FSD shown in Figure 5.1.

There is significant geographical variation of the mean annual FSD in the tropics and subtropics. Much of this appears to coincide with the mean cloud cover, shown in Figure 5.2. This suggests that this variability is due to the cloud fraction dependence in the parametrization. However, it should be noted that the mean cloud cover and mean FSD are not directly linked; the mean cloud cover depends on the cloud vertical overlap assumptions and the cloud frequency of occurrence in addition to the layer cloud fractions, while the parametrization depends on layer cloud fractions only.

Figure 5.3 shows the modelled FSD climatology binned into two seasons, December-January-February (DJF) and June-July-August (JJA) and by cloud height. The thresholds for binning the cloud by height coincide with those used in ISCCP: low clouds exist between the surface and 3.2

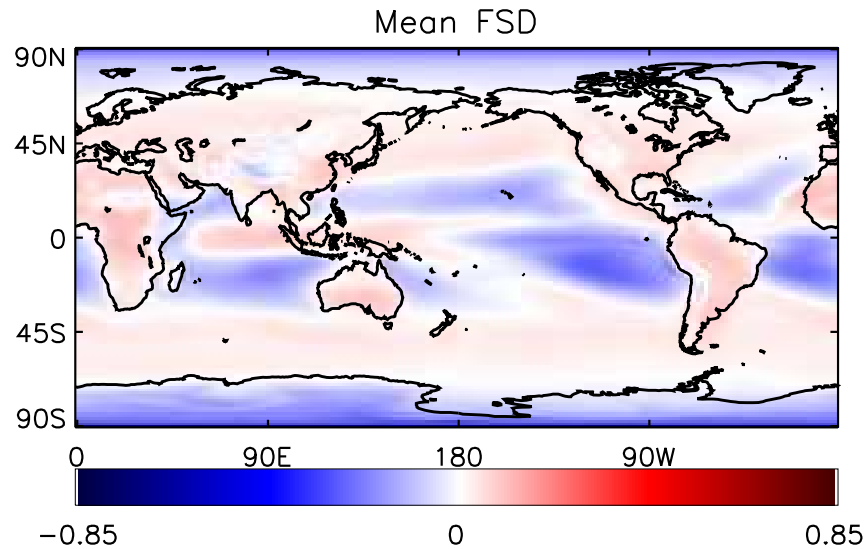


Figure 5.1 10year mean time and height averaged modelled in-cloud FSD (from the FSD param experiment) minus the mean value (0.85)

km, mid-level clouds exist between 3.2 and 6.5 km and high clouds exist between 6.5 km and the top of the model.

The mean modelled FSD increases significantly with height. This is because the parametrization predicts larger FSD for thicker layers and vertical resolution decreases with height in the model. Inter-seasonal differences are small. However, there is a definite land-sea divide for the low and mid-level clouds, which is particularly evident for low clouds over South America.

Figure 5.4 shows the mean cloud cover for the same seasons and cloud heights. Note that this is the mean cloud cover for clouds with *cloud top* in the given height range. Many low and mid-level cloudy layers that are below higher clouds are excluded from the low and mid-level cloud cover distributions shown in Figure 5.4, but contribute to the mean FSD values shown in Figure 5.3. The cloud cover and FSD are obviously correlated in some regions (e.g. for high clouds in the tropics). However, on a global scale, the correlation between cloud cover and FSD appears to be smaller than for the all-levels annual mean values, which is probably due to the different

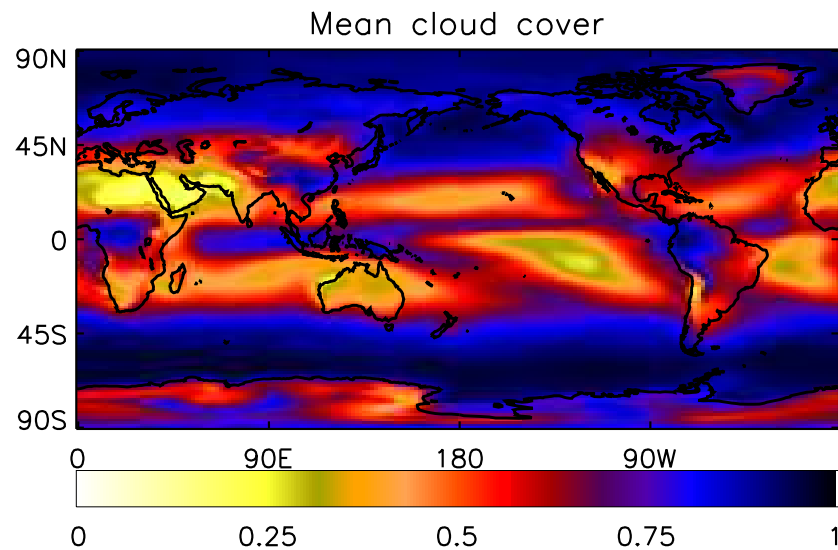


Figure 5.2 Mean modelled cloud cover

definitions of low and mid-level clouds that are used.

Rossow *et al.* (2002) describes a climatology of cloud optical thickness variability derived from ISCCP data. A direct comparison between the modelled FSD climatology shown above and the ISCCP derived climatology is not possible, due to the different inhomogeneity parameters, cloud variables, and scales considered. However, it is possible to compare the relative changes to the climatologies with height and location, which may highlight weaknesses of the FSD parametrization. The most obvious difference between the modelled and ISCCP climatologies (Rossow *et al.*'s (2002) Figure 15) is that the ISCCP inhomogeneity parameter increases at high latitudes. However, the ISCCP value does not have to account for increasing resolution and ISCCP optical thickness retrievals are much less accurate over snow and ice. The obvious land-sea difference for low clouds shown in Figure 5.3 is not present for low ISCCP cloud, but is for mid-level ISCCP clouds. Other than this, the distributions for low and mid-level clouds are similar, with both exhibiting variability distributions that appear to be related to cloud cover. However, for high clouds, the ISCCP climatology shows a decrease in inhomogeneity for mid-latitude clouds

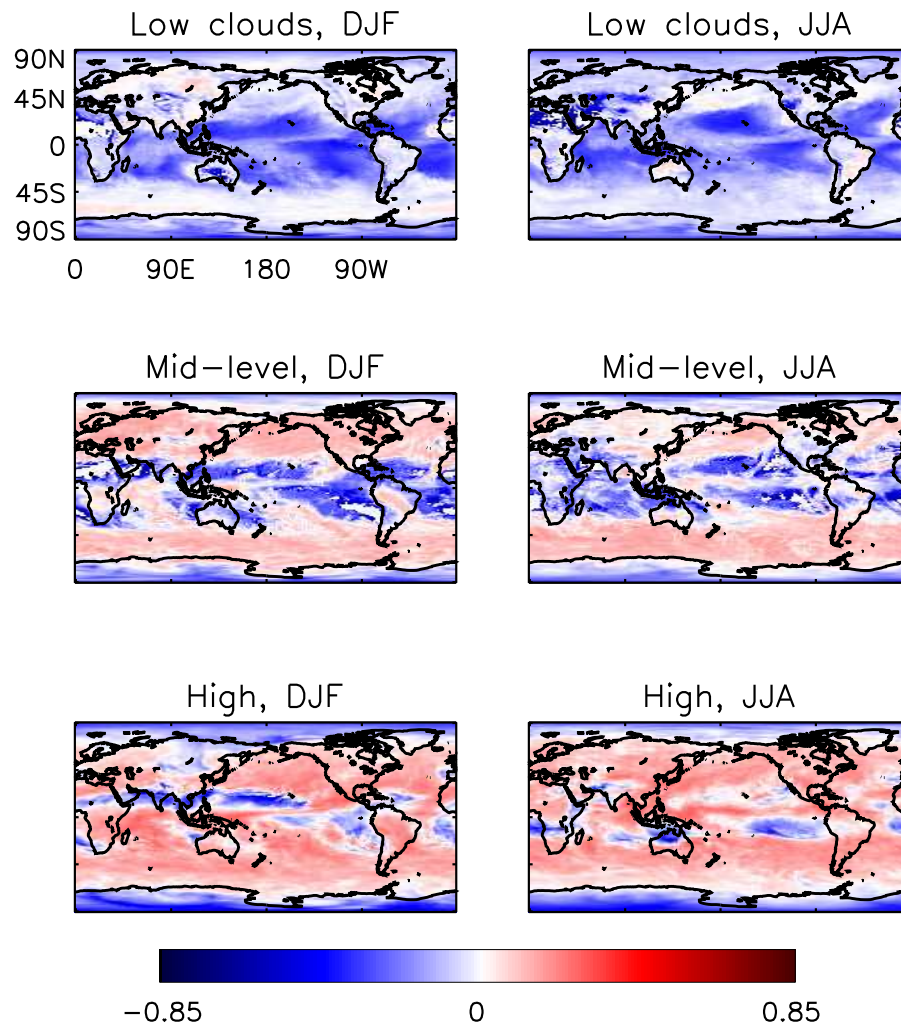


Figure 5.3 Mean modelled FSD minus 0.85, broken down into DJF (left column) and JJA (right column), and low (lower than 3.2 km), mid-level (between 3.2 and 6.5 km) and high clouds (above 6.5 km) (top, middle and bottom rows respectively).

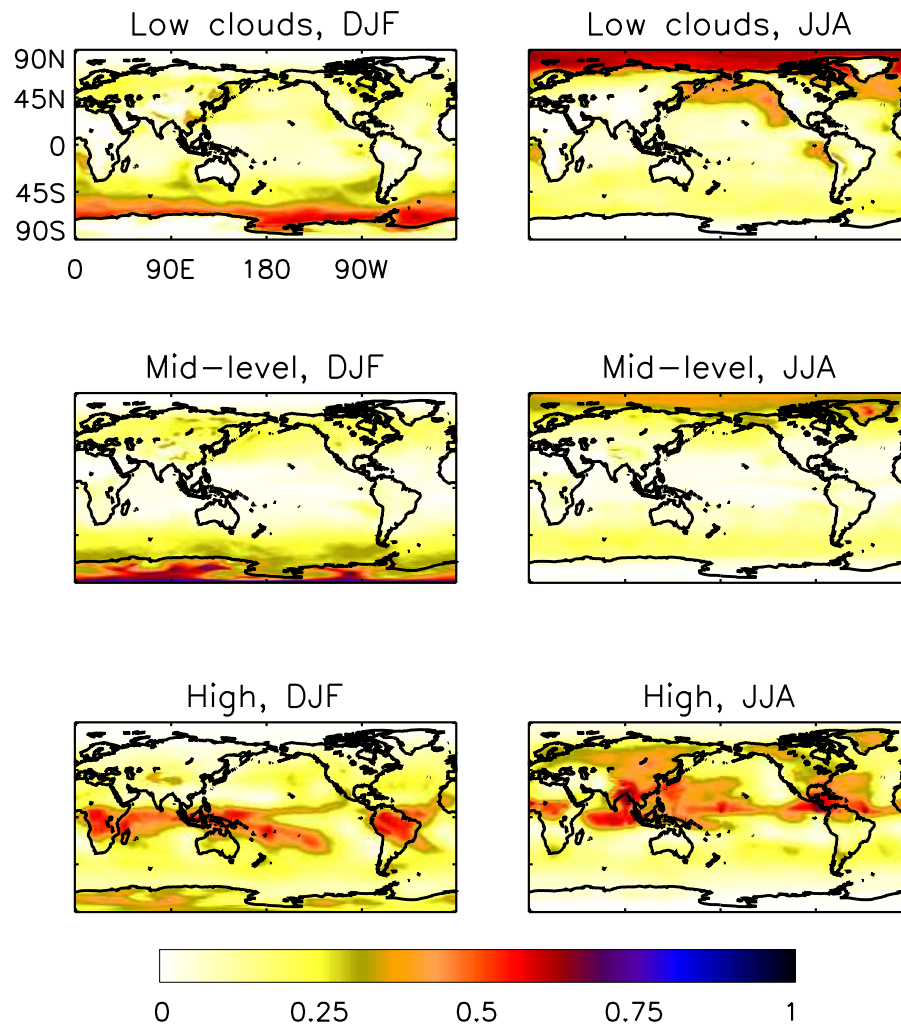


Figure 5.4 Mean modelled cloud fraction, broken down into DJF (left column) and JJA (right column), and low (lower than 3.2 km), mid-level (between 3.2 and 6.5 km) and high clouds (above 6.5 km) (top, middle and bottom rows respectively).

that is not evident in the model climatology.

The behaviour of the FSD predicted by the parametrization can be summarised as follows:

- The average FSD value equals 0.85, which is within the range of FSD estimates considered by Shonk *et al.* (2010), but larger than their estimate of the mean FSD (0.75), which is used operationally in GA4.0.
- As a result of the gridbox size dependence in the parametrization, the parametrization predicts smaller FSD values at high latitudes. This complicates the comparison with other observations, where the size of the gridbox used to calculate subgrid-scale variability is independent of latitude.
- The layer thickness dependence in the parametrization leads to larger FSD values for higher clouds. Again, this complicates the comparison with other observations.
- Areas of small mean cloud fraction tend to correspond to smaller FSD values. The resulting geographical distribution of FSD is a reasonable match to the ISCCP based inhomogeneity climatology described by Rossow *et al.* (2002).

5.4 EFFECT OF FSD PARAMETRIZATION

5.4.1 GLOBAL MEAN EFFECTS

Table 5.1 shows global mean values for TOA and surface cloud radiative effects (CREs) and other key model variables. The global mean total cloud cover, surface temperature and precipitation are very similar in all four experiments. However, the global mean CREs differ significantly. The largest CRE differences are between the PP-MRO and FSD param experiments, where the difference is as much as 10% of the CRE.

Table 5.2 shows changes in global mean CREs for noteworthy pairs of experiments. These changes are significant: the difference in net TOA CRE between the PP-MRO and FSD param experiments (1.14 Wm^{-2}), is comparable to the difference (1.0 Wm^{-2}) between two completely different cloud schemes (Wilson *et al.*, 2008b). However, the changes are much smaller than the

Experiment	GA4.0	FSD param	FSD=0.85	PP-MRO
Total cloud cover	0.67	0.67	0.67	0.65
Precipitation (mmday ⁻¹)	3.05	3.06	3.05	3.05
Surface temperature (K)	288.19	288.18	288.19	288.22
LW TOA CRE (Wm ⁻²)	25.10	23.61	24.69	26.49
SW TOA CRE (Wm ⁻²)	-45.52	-43.37	-44.68	-47.40
Net TOA CRE (Wm ⁻²)	-20.42	-19.76	-19.99	-20.90
LW surface CRE (Wm ⁻²)	24.64	23.63	24.16	25.77
SW surface CRE (Wm ⁻²)	-48.20	-45.98	-47.30	-50.18
Net surface CRE (Wm ⁻²)	-23.56	-22.35	-23.14	-24.41

Table 5.1 Global mean values for given variables for each of the 10-year climate simulations.

Experiment	Δ param	Δ FSD	Δ GA4.0
LW TOA CRE (Wm ⁻²)	-1.08	-0.41	-1.39
SW TOA CRE (Wm ⁻²)	1.31	0.84	1.88
Net TOA CRE (Wm ⁻²)	0.23	0.42	0.49
LW surface CRE (Wm ⁻²)	-0.53	-0.48	-1.14
SW surface CRE (Wm ⁻²)	1.31	0.90	1.98
Net surface CRE (Wm ⁻²)	0.78	0.42	0.85

Table 5.2 Change in global mean values of given variables. The Δ param column shows the difference between the FSD param and FSD=0.85 experiments (i.e. the impact of allowing the FSD to vary globally), the Δ FSD column shows the difference between the FSD=0.85 and GA4.0 experiments (i.e the effect of changing the FSD from 0.75 to 0.85) and the Δ GA4.0 shows the difference between the GA4.0 and PP-MRO experiments.

inter-model spread of values (e.g. Wild and Roeckner (2006) shows TOA SW CREs from -44 to -57 Wm^{-2} in the IPCC AR4 models). Moreover changes to global mean fluxes are important because GCMs are usually tuned to match the observed global mean TOA radiative fluxes. Re-tuning after changing the representation of subgrid cloud structure may further affect the model (though this is beyond the scope of this chapter).

The rightmost column of table 5.2 shows the difference between the PP-MRO experiment and the GA4.0 experiment. This comparison is useful for putting the others into context. These differences are consistent with those found by Shonk *et al.* (2012) using ‘Tripleclouds’ and an earlier version of the MetUM. Shonk *et al.* (2012) showed that this arises from a partial cancellation of increased CREs due to the overlap changes and decreased CREs due to the representation of horizontal water content inhomogeneity.

The middle column shows the effect of increasing a globally constant FSD from 0.75 to 0.85. This highlights that the global mean radiative fluxes are quite sensitive to fairly small changes in FSD. Assuming that the effect of larger changes to the global mean FSD can be estimated by extrapolating linearly, this effect is much smaller than that found by Shonk and Hogan (2010), but agrees very well with the sensitivity estimates of Barker and Räisänen (2005).

Now, consider the ‘ Δ param’ column, which shows the difference between the FSD param and FSD=0.85 experiments, we see that both TOA and surface CREs are reduced in the FSD param experiment. In the SW this is thought to be due to a combination of the cloud fraction dependence in the parametrization and the fact that FSDs are larger at low latitudes which contribute more to the global mean CRE. In the LW, the increase in FSD with height is also important and explains the difference in LW CRE at the surface and TOA (cf. the other two columns where the surface and TOA LW CRE differences are much more closely matched). The magnitude of both SW and LW CRE changes are of the same order as the other two columns.

The fact that the global mean TOA and surface CREs differ between the FSD param and FSD=0.85 experiments is probably the key result of this chapter, as it implies that a globally varying FSD parametrization is necessary in order to obtain unbiased TOA and surface radiative fluxes; even a perfect estimate of the global mean FSD will lead to global mean radiative biases if applied globally.

5.4.2 IMPACT ON GEOGRAPHICAL DISTRIBUTIONS

Figure 5.5 shows the difference in TOA seasonal mean outgoing SW and LW fluxes between the FSD param and FSD=0.85 experiments. The model clear sky fluxes (not shown) in the experiments are practically identical, apart from over China and Mongolia during DJF, where the model has a long-standing bias and most changes to the model result in quite large random differences. All other changes in the all-sky fluxes are due to cloud radiative effect changes. In both seasons, SW fluxes are generally reduced, while LW fluxes are generally increased. In the LW, the largest changes (both increases and decreases) occur in tropical regions of deep convection. There are also large changes in the outgoing SW flux in these regions. The distribution of TOA flux changes shown in Figure 5.5 cannot be explained by the FSD changes shown in Figure 5.3, as there are areas where the mean TOA flux changes are in the opposite direction to those one would expect from the mean FSD changes (e.g. over Russia in JJA). This suggests that the cloud fields have been changed.

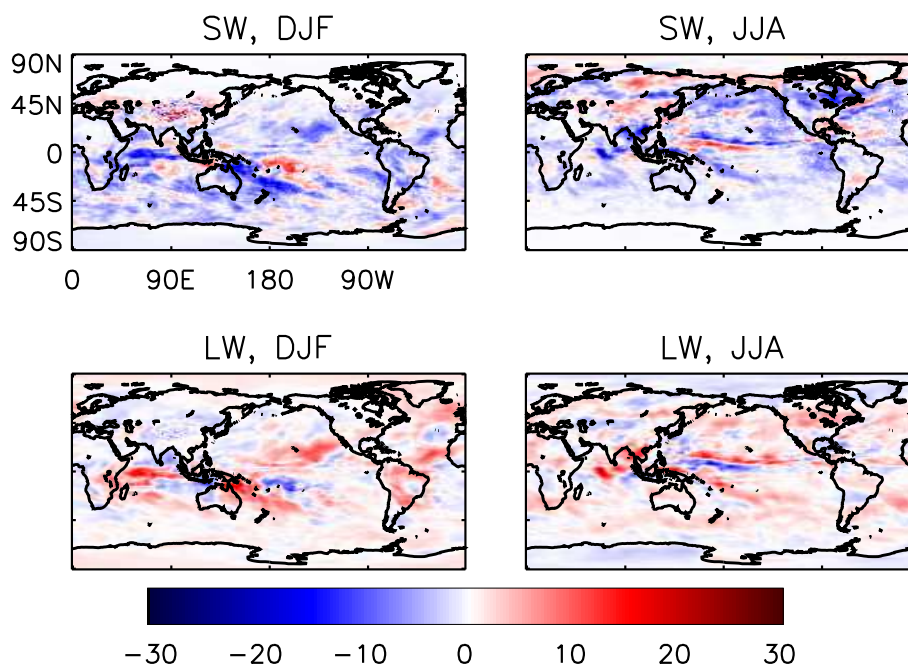


Figure 5.5 Time mean difference in TOA radiative fluxes between the FSD param and FSD=0.85 experiments: outgoing SW (top) and LW (bottom) fluxes, for DJF (left) and JJA (right).

Figures 5.6 and 5.7 show the corresponding changes in DJF and JJA mean cloud fractions respectively. Note that the global mean cloud cover is unchanged in both DJF and JJA. These cloud fraction changes correspond quite closely to the TOA flux changes shown in Figure 5.5. The few remaining differences can be explained by the FSD changes. For example, the reduction in both SW and LW cloud radiative effect over the north Pacific can be explained by the increase in FSD over this region. This result is consistent with the study of Gu and Liou (2006), which also found that the difference in the global distribution TOA radiative fluxes between their experiments appeared to be better correlated with cloud cover changes than with their scaling factor changes. These changes are fairly small compared to those obtained from modifications to the models cloud scheme (e.g. Wilson *et al.*, 2008b). Moreover, they are much smaller than the difference between the model and observations; the area-weighted RMS (root mean square) difference between the simulations is around 0.02 in both seasons, while the RMS difference between the models and the ISCCP climatology for both experiments is 0.19 in DJF and 0.16 in JJA.

In order to estimate the statistical significance of the change in total cloud cover, the pooled standard error, SE , of the annual mean values was calculated for each gridbox,

$$SE = \frac{\sqrt{(\sum_{i=1}^{10} (x_i - \bar{x})^2 + \sum_{i=1}^{10} (y_i - \bar{y})^2)/18}}{\sqrt{5}} \quad (5.2)$$

where x denotes one experiment and y denotes the other, the x_i, y_i variables refer to the annual mean cloud cover in the i -th year of each experiment and \bar{x}, \bar{y} denote the 10-year mean values for the two experiments. This pooled standard error is the denominator of the test statistic for a conventional Student's t-test (though such a test is not applicable due to the small sample sizes and the correlation between the annual mean values). The hatching in Figures 5.6 and 5.7 indicates where the change in total cloud cover is greater than the pooled standard error for each point (thin increasing lines) and twice the pooled standard error for each point (thicker decreasing lines). For such a small number of samples, statistical significance tests generally have thresholds larger than two, which means that they require the difference to be greater than twice the standard error (e.g. for the Student t-test the threshold for a 95% significance test is 2.101 while for the table lookup test (Zwiers and von Storch, 1995), where the threshold depends on the sample correlation, it is at least 2.84). For a 95% significance test, approximately 5% of the points would give a false rejection. For the cloud fraction changes shown in figures 5.6 and 5.7 2.66% of the gridboxes

are changed by more than twice the standard error in DJF and 4.55% in JJA. Thus, using either threshold, we would conclude that the experiments are not significantly different.

The geographical distributions of precipitation and 1.5 m temperature (not shown) differ between the FSD param and FSD=0.85 experiments, with local mean changes as large as 6 mmday^{-1} , and 2.75 K respectively. The temperature changes are similar to those shown by Räisänen and Järvinen (2010) for changes to the cloud scheme and representation of subgrid cloud structure in the the European Centre Hamburg Model 5 (ECHAM5) and as Räisänen and Järvinen (2010) found, the experiment differences are much smaller than the differences with respect to observations. The precipitation changes are of a similar magnitude to those detected by Gu and Liou (2006), when they changed the inhomogeneity of cirrus clouds, however the differences between the experiments are again much smaller than the differences between either experiment and observations. As for the cloud cover, comparison of the precipitation and 1.5 m temperature changes to interannual variability suggests that they are not statistically significant.

Figure 5.8 shows zonal mean differences between the FSD param and FSD=0.85 experiments, with error bars showing the pooled sample error at each latitude (following equation 5.2, but using zonal mean values). Zonal averages are useful because the interannual variability is reduced, making it easier to identify significant differences. Differences in the zonal mean TOA SW and LW fluxes appear to be significant at some latitudes, notably between 50 South and the Equator in DJF. However, for the other three variables considered, the zonal mean differences don't appear to be significant; the latitudes with largest differences also have largest uncertainty.

Comparing the FSD=0.85 experiment to the GA4.0 experiment and the GA4.0 experiment to the PP-MRO experiment, the zonal mean differences are of a similar magnitude. As a result, it is also not possible to detect statistically significant differences between the cloud cover, precipitation and surface temperature in these pairs of experiments. This remains the case even when comparing the two experiments with largest differences in global mean CREs (i.e. the FSD param and PP-MRO experiments).

Although it is not possible to conclude that differences to cloud cover, 1.5 m temperature and precipitations are statistically significant based on the simulations described here, it may be possible to detect statistically significant changes using longer experiments which have smaller

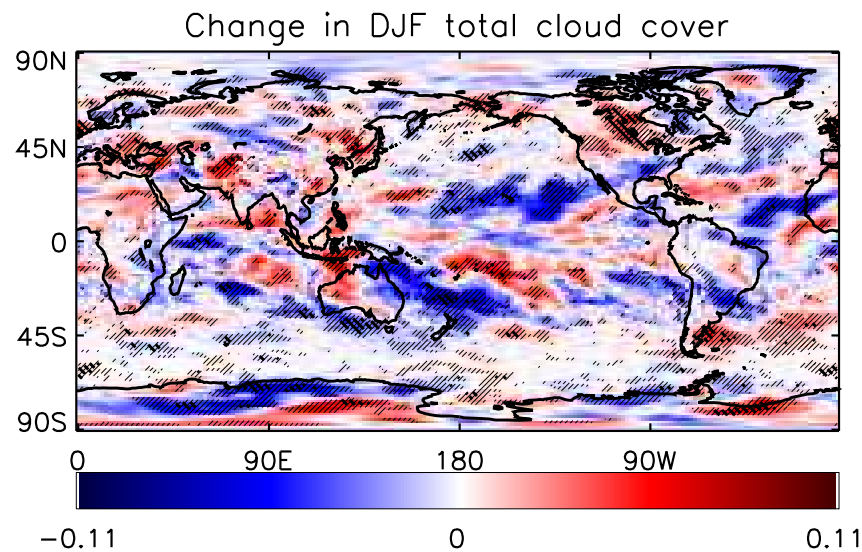


Figure 5.6 Time mean difference in DJF total cloud cover between the FSD param and FSD=0.85 experiments. The thin increasing hatching indicates where the difference exceeds the pooled standard error and the thicker decreasing hatching indicates where the hatching exceeds twice the pooled standard error.

sampling errors. For instance, Shonk *et al.* (2012) compares two 20-year experiments, with different treatments of the radiative effect of subgrid cloud structure, similar to the GA4.0 PP-MRO comparison described here. They were able to detect statistically significant changes to cloud fraction and temperature, while the global mean radiative flux changes were similar to those observed in this study.

Although the impacts of the changes to subgrid cloud structure are fairly small in these simulations of current climate, this does not preclude them from having larger impacts on climate change experiments. For example, in simulations with ECHAM5, Räisänen and Järvinen (2010) found that using McICA combined with subgrid cloud information from the cloud scheme made little difference to the model performance for present climate, but led to marked differences in the response to increased atmospheric carbon dioxide.

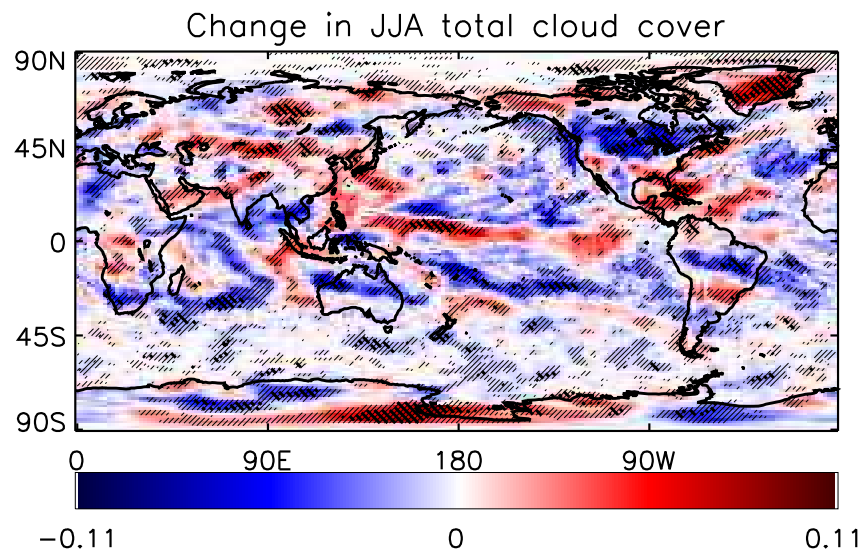


Figure 5.7 As Figure 5.6, but for JJA.

5.5 CONCLUSIONS

This chapter has considered the impact of changing the representation of subgrid-scale cloud structure in 10-year MetUM climate simulations. Four experiments were run and compared in order to analyse the impact of changes to the subgrid-scale cloud structure: the GA4.0 experiment used McICA with a global FSD of 0.75 and exponential-random overlap with a decorrelation pressure scale of 100 hPa, in the FSD param experiment the FSD parametrization was applied, the FSD=0.85 experiment used a global FSD of 0.85 (equal to the area-weighted mean in the FSD param experiment), and the PP-MRO experiment treated clouds as horizontally homogeneous and used maximum-random overlap.

Comparison of the FSD param and FSD=0.85 experiments shows that, as expected from the design of the parametrization, the FSD param experiment has decreased inhomogeneity at very high latitudes, increased inhomogeneity for higher clouds, and more inhomogeneity in regions where mean cloud fractions are larger. The FSD parametrization was found to decrease global

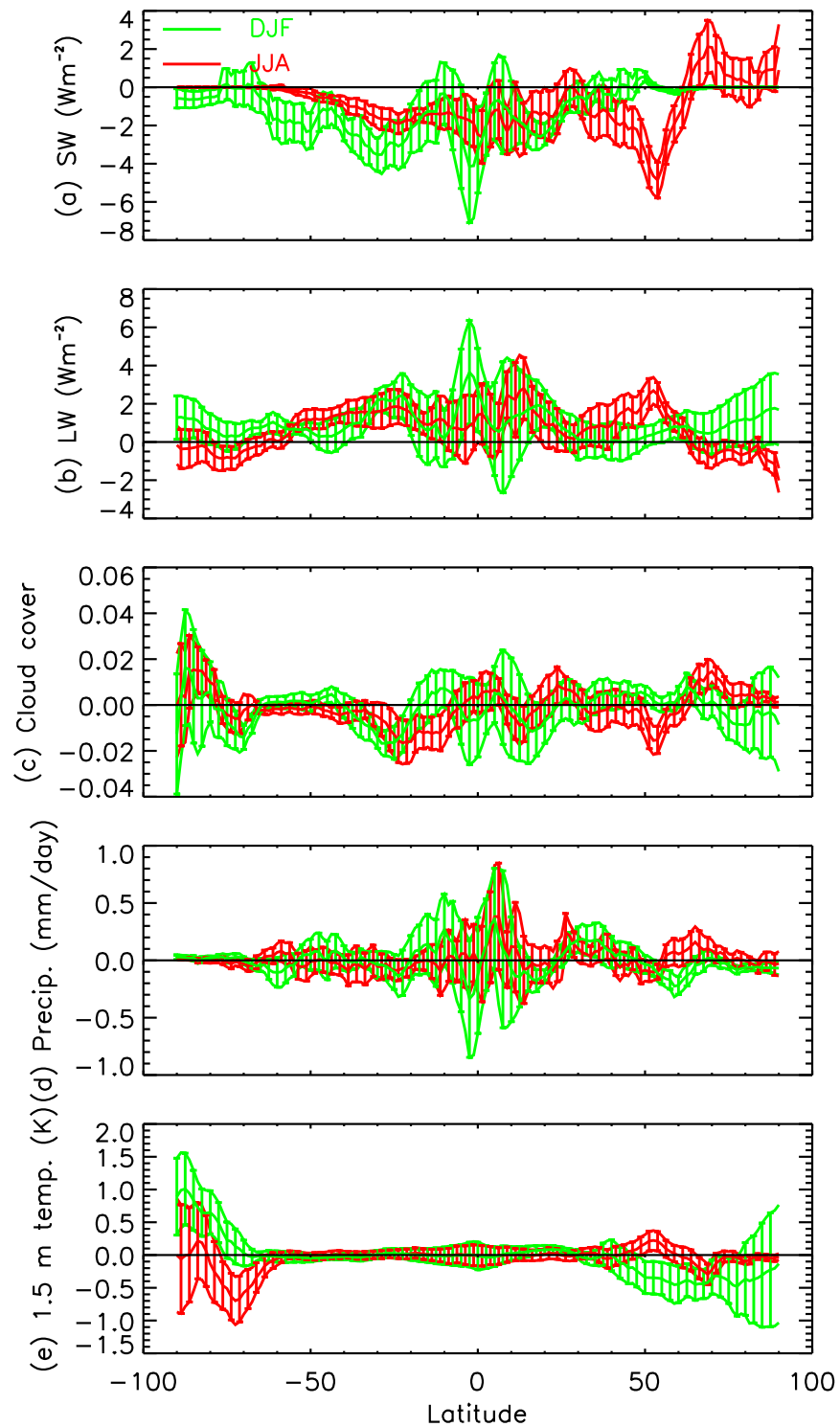


Figure 5.8 10-year zonal mean differences between FSD param and FSD=0.85 experiments. The vertical error bars show the mean difference plus and minus the pooled standard error.

mean SW and LW CRE by around 1 Wm^{-2} relative to the FSD=0.85 experiment, due to the parametrization predicting smaller FSD where FSD has less effect (i.e. at high latitudes, for smaller cloud fractions, and (for TOA LW effect) for low clouds). This implies that a globally varying FSD is required in order to get unbiased TOA radiative fluxes. Local differences in mean cloud cover, precipitation and 1.5 m temperature are fairly large in some areas, but are not statistically significant.

Comparison of the GA4.0 and PP-MRO experiments was performed to put the other experiments in context. In terms of global mean CREs, the Δ param, ΔFSD and $\Delta GA4.0$ differences are all of the same magnitude. This implies that allowing the FSD to vary globally, ensuring that the global mean FSD is correct and representing the combined effect of horizontal and vertical inhomogeneity are of roughly equal importance.

One of the advantages of the FSD parametrization is that it can be used at different model resolutions. At the particular resolution at which these climate simulations were run, the mean FSD (0.85) turned out to be quite close to the default value (0.75) used in GA4.0 for all resolutions. This leads to small but significant differences to the TOA fluxes (around 0.9 Wm^{-2} in the SW and 0.4 Wm^{-2} in the LW). However, at higher (lower) resolutions, we would expect the mean parametrized FSD to be smaller (larger). Consequently, the default FSD value may be less appropriate at other resolutions, which may have quite a large impact on the TOA fluxes.

Although the FSD parametrization was derived for ice water content only, it was applied to both liquid and ice clouds. Moreover, to account for the expected difference in variability between a 2D domain and a 1D slice through that domain, the parametrized value was multiplied by $\sqrt{2}$. Future work will aim to verify and explain this 1D-2D difference.

The parametrization may also be adopted in global numerical weather prediction (NWP) models, where the typical resolution (around 40 km), though higher, is still low enough for unresolved water content variability to have significant radiative impacts. We aim to test the performance of the parametrization in some NWP case studies in the near future.

CHAPTER 6:

CONCLUSIONS AND FUTURE WORK

This thesis examines the representation of subgrid cloud structure and its radiative effects in general circulation models (GCMs). More specifically, the representation of subgrid-scale horizontal water content variability and cloud vertical overlap is studied with the aid of state-of-the-art satellite observations.

6.1 SUMMARY AND CONCLUSIONS

While the radiative bias due to neglecting subgrid-scale water content variability has long been recognised as a problem (e.g. Cahalan *et al.*, 1994a), efficient and effective methods for representing the radiative effects of variability (e.g. Pincus *et al.*, 2005; Shonk and Hogan, 2008) are a more recent development. Chapter 2 concerns one such method, the Monte Carlo Independent Column Approximation (McICA), which introduces conditional random errors. This chapter describes evaluation, reduction and impacts of this noise in the Met Office Unified Model (MetUM). It includes a description of a new method for reducing the random errors, which reduces mean absolute flux and heating rate errors due to noise by a factor of two, while increasing the number of monochromatic calculations required by around 50%. Tests with global numerical weather prediction (NWP) simulations show that once noise is reduced sufficiently, McICA can lead to improved surface temperature forecasts, compared to a simulation using the plane-parallel maximum-random overlap (PP-MRO) representation to calculate cloud radiative effects.

The main reason for adopting McICA for representing the radiative effects of subgrid cloud structure is the flexibility that it allows. This is illustrated by chapter 4; the overlap parametrization changes would be much more complicated if the overlap assumptions were embedded in the radiative transfer solver. Another advantage is that the subgrid cloud structure used by the radiative transfer scheme is more explicit, so it is easier to use consistent subgrid cloud structure

in other physical processes. In terms of future model development, one disadvantage involves the representation of 3D radiative transfer effects; McICA may be incompatible with schemes for accounting for 3D effects (e.g. Hogan and Shonk, 2012)

Irrespective of the method used to represent the radiative effects of subgrid-scale water content inhomogeneity, the magnitude of the radiative impacts depends on the magnitude of the variability (e.g. Barker and Räisänen, 2005; Shonk and Hogan, 2010). Moreover, the amount of unresolved water content variability remains poorly characterised. This problem is addressed in chapter 3, where water content variability is studied using a CloudSat data product that combines CloudSat radar and Moderate-Resolution Imaging Spectroradiometer (MODIS) visible optical depth observations to retrieve water content. Due to issues with the effect of drizzle on the retrieved liquid water content, the study is restricted to ice water content only. This chapter resolves some of the apparently contradictory results in the existing literature (e.g. concerning the effect of cloud fraction on variability) and explains how resolution affects unresolved variability. A parametrization of the fractional standard deviation (FSD) of ice water content is derived, that accounts for the effects of horizontal and vertical resolution, and cloud fraction.

In many GCMs (e.g. Morcrette *et al.*, 2008), including the MetUM, the subgrid cloud structure required for McICA is produced by a stochastic cloud generator (Räisänen *et al.*, 2004). The combination of McICA and a stochastic cloud generator permits more flexibility in the representation of vertical cloud overlap, which is considered in chapter 4. In this chapter a combination of CloudSat radar and Cloud-Aerosol Lidar and Infrared Pathfinder Satellite Observation (CALIPSO) lidar observations are used to examine the distribution of overlap. Precipitation is found to have a large impact on the overlap; as the effect of precipitation cannot be removed cleanly, the chapter is restricted to a qualitative analysis. We show that the distribution of overlap (but not the mean) is sensitive to assumptions concerning the horizontal cloud structure. Neither the deterministic overlap required when the overlap assumptions are incorporated into the radiative transfer solver, nor the original version of the Räisänen *et al.* (2004) cloud generator can capture the observed overlap distribution. It is shown that the observed distribution of overlap can be modelled by a new version of exponential-random overlap combined with the correct horizontal cloud structure. However, while OLR and cloud cover biases for the new overlap parametrization and the default exponential-random overlap parametrization are similar, mean absolute errors are increased by

around 25% by the new parametrization.

Chapter 5 describes the effect of changes to the representation of sub-grid scale cloud on a 10-year MetUM climate simulation, with an emphasis on the impact of the FSD parametrization of chapter 3. Including the FSD parametrization in the model allows us to examine the mean geographical distribution of subgrid-scale variability predicted by the parametrization. Comparing two 10-year climate simulations, one with parametrized FSD and the other with constant FSD, but both with the same mean FSD, we find that global mean top of atmosphere (TOA) fluxes in the simulation with parametrized FSD are 1-2 Wm^{-2} smaller in both the shortwave (SW) and longwave (LW). This implies that a ‘perfect’ unbiased estimate of the global mean FSD will lead to biases in the model’s radiative fluxes and a globally varying FSD is necessary to calculate unbiased radiative fluxes. Small changes to global mean TOA fluxes are important because models are usually tuned to match the observed mean net TOA flux. Changes to the subgrid-scale cloud structure have no impact on the global mean cloud cover, surface temperature or precipitation rate, but do change the geographical distribution of each of these variables. However these local changes are not found to be statistically significant in the relatively short climate simulations performed and they are much smaller than the differences with respect to observations.

6.2 FUTURE WORK

There are still many aspects of small scale cloud structure and its representation in GCMs that are uncertain. As a result, there are many interesting areas of research in this area, some of which are detailed below.

The stochastic cloud generator of Räisänen *et al.* (2004) has been adopted in many GCMs (e.g. Cole *et al.*, 2011; Räisänen and Järvinen, 2010) including the MetUM, in order to produce the subgrid cloud fields used for McICA radiative transfer calculations. Subgrid cloud structure is also important for other processes; precipitation accretion and evaporation depend on overlap (Jakob and Klein, 1999) while autoconversion rates depend on subgrid horizontal water content variability (Larson *et al.*, 2001). The generated cloud field, or at the very least consistent assumptions, should be used throughout the model, whenever assumptions about subgrid cloud structure are required.

The FSD parametrization described in chapter 3 applies to ice water content only. Variability of liquid water content is equally important. Although some studies have shown that the variability of ice and liquid water is significantly different (e.g. Shonk and Hogan, 2008), others have drawn the opposite conclusion (e.g. Oreopoulos and Cahalan, 2005). To conduct a fair comparison of ice and liquid water content variability, a dataset that contains equally good estimates of both ice and liquid water content is required.

Studies of water content variability have found that it is related to meteorological regime (e.g. Barker *et al.*, 1996; Pincus *et al.*, 1999). Moreover, our study found a relationship with latitude (not shown in this thesis), which could not be explained by the final parametrization, suggesting that there is a meteorological regime dependence in the CloudSat observations. Analysis of the climatology of the modelled FSD in chapter 5 showed that FSD tended to be smaller in areas of frequent cumulus cloud, whereas Barker *et al.* (1996) and Pincus *et al.* (1999) both found that cumulus was more variable than other cloud types. The lack of regime dependence may also account for some of the differences between the modelled FSD climatology and the ISCCP based climatology of Rossow *et al.* (2002).

The CloudSat data on which the FSD parametrization is based, consists of 1D observations of water content along a straight line within each layer. For the climate simulation described in chapter 5, we required an estimate of the FSD within a 2D box for each layer. Based on a brief analysis of a limited amount of cloud resolving model data, we account for the difference by multiplying the parametrized FSD by a factor of $\sqrt{2}$. Ideally this difference should be analysed using 3D cloud observations. Ground-based scanning cloud radars may provide a suitable source of observations for such a study. It would also be prudent to test the robustness of FSD parametrization using other data sets, for example aircraft observations, ground based radar observations, or cloud resolving model (CRM) simulations.

GCM cloud schemes must make assumptions about the subgrid distribution of cloud water content in order to predict gridbox mean cloud variables. Ideally, the cloud scheme and cloud generator should use the same distribution (or at least make consistent assumptions). However, the distributions assumed by the prognostic cloud prognostic condensate (PC2) cloud scheme (Morcrette *et al.*, 2008) are not explicit, so cannot be easily compared to the generated distributions. The benefits of an explicit subgrid water content distribution should be considered when

future cloud schemes are developed.

We have documented the impact of the new FSD parametrization on a climate simulation. As GCMs are usually tuned so that the net mean TOA flux matches observations, further re-tuned experiments should be run. Longer (20 year) simulations would be informative because the increased sampling of interannual variability means that statistical significance tests have more power. Coupling to an ocean model would allow the oceans to respond to atmospheric changes and provide further insight. NWP models are generally run at a higher resolution than climate simulations, so the magnitude of unresolved water content variability is smaller. Nevertheless, radiative biases arising from unresolved water content variability are certainly significant at the typical scale (40 km) of global NWP models. The parametrization was designed to be applicable across a broad range of resolutions and should be tested in NWP models, which may provide more insight into the behaviour of the parametrization.

We showed that the distribution of overlap is strongly dependent on horizontal cloud structure (i.e. whether a gridbox contains one contiguous clouds or multiple broken clouds). In reality, the distribution of cloud sizes follows a power law, with an exponent around -1.66 (Wood and Field, 2011). It would be sensible to test how well the combined CloudSat and CALIPSO data captures this behaviour. Moreover, as for the FSD parametrization, the robustness of the conclusions should be tested using other data sources such as ground based observations or CRM simulations.

In chapter 4, we showed that, in terms of mean absolute outgoing longwave radiation (OLR) and total cloud cover errors, it is better to model the overlap using the mean of the distribution rather than trying to capture the distribution itself. This may not be the case for radiative heating rates. Moreover, one would expect use of the mean overlap to result in heating rate profiles that are much smoother than observed, which may have feedback effects in a GCM. Finally, while instantaneous OLR and cloud cover errors are important in NWP models, this is not the case for climate simulations. Clearly, there is more work to do before final conclusions about the importance of capturing the distribution of overlap may be made.

Two aspects of subgrid cloud structure that have not been considered in this thesis are the vertical correlation of the water content distribution in different layers of a cloud and the subgrid variability of liquid droplet and ice crystal sizes. The radiative impact of changing the vertical

correlation of the water content distribution is very small (e.g. Barker and Räisänen, 2005). The radiative impact of neglecting subgrid variability of droplet/crystal sizes, though smaller than that of neglecting water content variability (e.g. Barker and Räisänen, 2004) is more significant and probably requires more immediate attention.

BIBLIOGRAPHY

- Allan, R. P. (2011). Combining satellite data and models to estimate cloud radiative effect at the surface and in the atmosphere. *Meteorological Applications*, **18**(3), 324–333.
- Allan, R. P., Slingo, A., Milton, S. F., and Brooks, M. E. (2007). Evaluation of the Met Office global forecast model using Geostationary Earth Radiation Budget (GERB) data. *Q. J. Roy. Meteorol. Soc.*, **133**(629), 1993–2010.
- Austin, R. T., Heymsfield, A. J., and Stephens, G. L. (2009). Retrieval of ice cloud microphysical parameters using the cloudsat millimeter-wave radar and temperature. *J. Geophys. Res.*, **114**(D00A23).
- Barker, H. W. (1996). A parameterization for computing grid-averaged solar fluxes for inhomogeneous marine boundary layer clouds. Part I: Methodology and homogeneous biases. *J. Atm. Sci.*, **53**(16), 2289–2303.
- Barker, H. W. (2008a). Overlap of fractional cloud for radiation calculations in GCMs: A global analysis using CloudSat and CALIPSO data. *J. Geophys. Res.*, **113**(D00A01).
- Barker, H. W. (2008b). Representing cloud overlap with an effective decorrelation length: An assessment using CloudSat and CALIPSO data. *J. Geophys. Res.*, **113**(D24205).
- Barker, H. W. and Davies, J. A. (1992). Solar radiative fluxes for stochastic, scale-invariant broken cloud fields. *J. Atm. Sci.*, **49**(13), 1115–1126.
- Barker, H. W. and Fu, Q. (2000). Assessment and optimization of the gamma-weighted two-stream approximation. *J. Atm. Sci.*, **57**(8), 1181–1188.
- Barker, H. W. and Räisänen, P. (2004). Neglect by GCMs of subgrid-scale horizontal variations in cloud-droplet effective radius: A diagnostic radiative analysis. *Q. J. Roy. Meteorol. Soc.*, **130**(600), 1905–1920.
- Barker, H. W. and Räisänen, P. (2005). Radiative sensitivities for cloud structural properties that are unresolved by conventional GCMs. *Q. J. Roy. Meteorol. Soc.*, **131**, 3103–3122.

- Barker, H. W. and Wielicki, B. A. (1997). Parameterizing grid-averaged longwave fluxes for inhomogeneous marine boundary layer clouds. *J. Atm. Sci.*, **54**(24), 2785–2798.
- Barker, H. W., Wielicki, B. A., and Parker, L. (1996). A parameterization for computing grid-averaged solar fluxes for inhomogeneous marine boundary layer clouds. Part II: Validation using satellite data. *J. Atm. Sci.*, **53**(16), 2304–2316.
- Barker, H. W., Morcrette, J.-J., and Alexander, G. D. (1998). Broadband solar fluxes and heating rates for atmospheres with 3D broken clouds. *Q. J. Roy. Meteorol. Soc.*, **124**(548), 1245–1271.
- Barker, H. W., Stephens, G. L., and Fu, Q. (1999). The sensitivity of domain-averaged solar fluxes to assumptions about cloud geometry. *Q. J. Roy. Meteorol. Soc.*, **125**, 2127–2152.
- Barker, H. W., Cole, J. N. S., Morcrette, J.-J., Pincus, R., Raisanen, P., von Salzen, K., and Vailancourt, P. A. (2008). The Monte Carlo Independent Column Approximation: An assessment using several global atmospheric models. *Q. J. Roy. Meteorol. Soc.*, **134**, 1463–1478.
- Bäumli, G., Chlond, A., and Roeckner, E. (2004). Estimating the PPH-bias for simulations of convective and stratiform clouds. *Atmospheric Research*, **72**(1-4), 317–328.
- Bergman, J. W. and Rasch, P. J. (2002). Parameterizing vertically coherent cloud distributions. *J. Atm. Sci.*, **59**(14), 2165–2182.
- Bodas-Salcedo, A., Webb, M. J., Brooks, M. E., Ringer, M. A., Williams, K. D., Milton, S. F., and Wilson, D. R. (2008). Evaluating cloud systems in the Met Office global forecast model using simulated CloudSat radar reflectivities. *J. Geophys. Res.*, **113**(D00A13).
- Bony, S. and Emanuel, K. A. (2001). A parameterization of the cloudiness associated with cumulus convection; evaluation using TOGA COARE data. *J. Atm. Sci.*, **58**(21), 3158–3183.
- Borde, R. and Isaka, H. (1996). Radiative transfer in multifractal clouds. *J. Geophys. Res.*, **101**(D23), 29461–29478.
- Boutle, I. A. and Morcrette, C. J. (2010). Parametrization of area cloud fraction. *Atmospheric Science Letters*, **11**(4), 283–293.
- Cahalan, R. F. (1994). Bounded cascade clouds: albedo and effective thickness. *Nonlinear Processes in Geophysics*, **1**(2/3), 156–167.

- Cahalan, R. F. and Joseph, J. H. (1989). Fractal statistics of cloud fields. *Monthly Weather Review*, **117**(2), 261–272.
- Cahalan, R. F., Ridgway, W., Wiscombe, W. J., Bell, T. L., and Snider, J. B. (1994a). The albedo of fractal stratocumulus clouds. *J. Atm. Sci.*, **51**(16), 2,434–2,455.
- Cahalan, R. F., Ridgway, W., Wiscombe, W. J., Gollmer, S., and Harshvardhan (1994b). Independent pixel and Monte Carlo estimates of stratocumulus albedo. *J. Atm. Sci.*, **51**(24), 3776–3790.
- Cahalan, R. F., Oreopoulos, L., Marshak, A., Evans, K. F., Davis, A. B., Pincus, R., Yetzer, K. H., Mayer, B., Davies, R., Ackerman, T. P., Barker, H. W., Clothiaux, E. E., Ellingson, R. G., Garay, M. J., Kassianov, E., Kinne, S., Macke, A., O’Hirok, W., Partain, P. T., Prigarin, S. M., Rublev, A. N., Stephens, G. L., Szczap, F., Takara, E. E., Vrnai, T., Wen, G., and Zhuravleva, T. B. (2005). THE I3RC: Bringing Together the Most Advanced Radiative Transfer Tools for Cloudy Atmospheres. *Bull. Amer. Meteor. Soc.*, **86**(9), 1275–1293.
- Cairns, B., Lacis, A. A., and Carlson, B. E. (2000). Absorption within inhomogeneous clouds and its parameterization in general circulation models. *J. Atm. Sci.*, **57**(5), 700–714.
- Carlin, B., Fu, Q., Lohmann, U., Mace, G. G., Sassen, K., and Comstock, J. W. (2002). High-cloud horizontal inhomogeneity and solar albedo bias. *J. Climate*, **15**(17), 2321–2339.
- Cess, R. D., Potter, G. L., Blanchet, J. P., Boer, G. J., Del Genio, A. D., Dqu, M., Dymnikov, V., Galin, V., Gates, W. L., Ghan, S. J., Kiehl, J. T., Lacis, A. A., Le Treut, H., Li, Z.-X., Liang, X.-Z., McAvaney, B. J., Meleshko, V. P., Mitchell, J. F. B., Morcrette, J.-J., Randall, D. A., Rikus, L., Roeckner, E., Royer, J. F., Schlese, U., Sheinin, D. A., Slingo, A., Sokolov, A. P., Taylor, K. E., Washington, W. M., Wetherald, R. T., Yagai, I., and Zhang, M.-H. (1990). Intercomparison and interpretation of climate feedback processes in 19 atmospheric general circulation models. *J. Geophys. Res.*, **95**(D10), 16601–16615.
- Chan, M. A. and Comiso, J. C. (2011). Cloud features detected by MODIS but not by CloudSat and CALIOP. *Geophys. Res. Lett.*, **38**(L24813).
- Chen, T., Zhang, Y., and Rossow, W. B. (2000). Sensitivity of atmospheric radiative heating rate profiles to variations of cloud layer overlap. *Journal of Climate*, **13**(16), 2941–2959.

- Cheng, A. and Xu, K.-M. (2006). Simulation of shallow cumuli and their transition to deep convective clouds by cloud-resolving models with different third-order turbulence closures. *Quarterly Journal of the Royal Meteorological Society*, **132**(615), 359–382.
- Cole, J., Barker, H. W., Loeb, N. G., and von Salzen, K. (2011). Assessing simulated clouds and radiative fluxes using properties of clouds whose tops are exposed to space. *J. Climate*, **24**(11), 2715–2727.
- Davis, A., Marshak, A., Wiscombe, W., and Cahalan, R. (1996). Scale invariance of liquid water distributions in marine stratocumulus. Part I: Spectral properties and stationarity issues. *J. Atm. Sci.*, **53**(11), 1538–1558.
- Davis, A. B., Marshak, A., Gerber, H., and Wiscombe, W. J. (1999). Horizontal structure of marine boundary layer clouds from centimeter to kilometer scales. *J. Geophys. Res.*, **104**(D6), 6123–6144.
- de la Torre Juárez, M., Davis, A. B., and Fetzer, E. J. (2011). Scale-by-scale analysis of probability distributions for global MODIS-AQUA cloud properties: how the large scale signature of turbulence may impact statistical analyses of clouds. *Atmospheric Chemistry and Physics*, **11**(6), 2893–2901.
- Dee, D. P., Uppala, S. M., Simmons, A. J., Berrisford, P., Poli, P., Kobayashi, S., Andrae, U., Balmaseda, M. A., and P. Bauer, G. B., Bechtold, P., Beljaars, A. C. M., van de Berg, L., Bidlot, J., Bormann, N., Delsol, C., Dragani, R., Fuentes, M., Geer, A. J., Haimberger, L., Healy, S. B., Hersbach, H., Hlm, E. V., Isaksen, L., Killberg, P., Khler, M., Matricardi, M., McNally, A. P., Monge-Sanz, B. M., Morcrette, J.-J., Park, B.-K., Peubey, C., de Rosnay, P., Tavolato, C., Thpaut, J.-N., and Vitart, F. (2011). The ERA-Interim reanalysis: configuration and performance of the data assimilation system. *Q. J. Roy. Meteorol. Soc.*, **137**(656), 553–597.
- Delanoë, J. and Hogan, R. J. (2010). Combined CloudSat-CALIPSO-MODIS retrievals of the properties of ice clouds. *J. Geophys. Res.*, **115**(D00H29).
- Delanoë, J., Hogan, R. J., Forbes, R. M., Bodas-Salcedo, A., and Stein, T. H. M. (2011). Evaluation of ice cloud representation in the ECMWF and UK Met Office models using CloudSat and CALIPSO data. *Q. J. Roy. Meteorol. Soc.*, **137**(661), 2064–2078.

- Edwards, J., Havemann, S., Thelen, J.-C., and Baran, A. (2007). A new parametrization for the radiative properties of ice crystals: Comparison with existing schemes and impact in a GCM. *Atmospheric Research*, **83**(1), 19–35.
- Edwards, J. M. (1996). Efficient calculation of infrared fluxes and cooling rates using the two-stream equations. *J. Atm Sci*, **53**, 1921–1932.
- Edwards, J. M. and Slingo, A. (1996). Studies with a flexible new radiation code. 1: Choosing a configuration for a large-scale model. *Q. J. Roy. Meteorol. Soc.*, **122**, 690–719.
- Eliasson, S., Buehler, S. A., Milz, M., Eriksson, P., and John, V. O. (2011). Assessing observed and modelled spatial distributions of ice water path using satellite data. *Atmospheric Chemistry and Physics*, **11**(1), 375–391.
- Fox, N. I. and Illingworth, A. J. (1997). The potential of a spaceborne cloud radar for the detection of stratocumulus clouds. *Journal of Applied Meteorology*, **36**(6), 676–687.
- Fu, Q. (1996). An accurate parameterization of the solar radiative properties of cirrus clouds for climate models. *J. Climate*, **9**(9), 2058–2082.
- Fu, Q. and Liou, K. N. (1992). On the correlated k-distribution method for radiative transfer in nonhomogeneous atmospheres. *J. Atm. Sci.*, **49**(22), 2,139–2,156.
- Fu, Q., Carlin, B., and Mace, G. (2000). Cirrus horizontal inhomogeneity and OLR bias. *Geophys. Res. Lett.*, **27**(20), 3341–3344.
- Geleyn, J. F. and Hollingsworth, A. (1979). An economical analytical method for the computation of the interaction between scattering and line absorption of radiation. *Contrib. Atmos Physics*, **52**, 1–16.
- Gollmer, S. M., Harshvardhan, Cahalan, R. F., and Snider, J. B. (1995). Windowed and wavelet analysis of marine stratocumulus cloud inhomogeneity. *J. Atm. Sci.*, **52**(16), 3013–3030.
- Gounou, A. and Hogan, R. J. (2007). A sensitivity study of the effect of horizontal photon transport on the radiative forcing of contrails. *J. Atmos. Sci.*, **64**(5), 1706–1716.
- Greuell, W., van Meijgaard, E., Clerbaux, N., and Meirink, J. F. (2011). Evaluation of model-predicted top-of-atmosphere radiation and cloud parameters over africa with observations from GERB and SEVIRI. *J. Climate*, **24**(15), 4015–4036.

- Gu, Y. and Liou, K. N. (2006). Cirrus cloud horizontal and vertical inhomogeneity effects in a GCM. *Meteorol Atmos Phys*, **91**, 223–235.
- Gu, Y., Farrara, J., Liou, K. N., and Mechoso, C. R. (2003). Parameterization of cloud-radiation processes in the UCLA general circulation model. *J. Climate*, **16**(20), 3357–3370.
- Han, Q., Rossow, W. B., Chou, J., and Welch, R. M. (1998). Global survey of the relationships of cloud albedo and liquid water path with droplet size using ISCCP. *J. Climate*, **11**(7), 1516–1528.
- Hill, P. G., Manners, J., and Petch, J. C. (2011). Reducing noise associated with the Monte Carlo Independent Column Approximation for weather forecasting models. *Q. J. Roy. Meteorol. Soc.*, **137**(654), 219–228.
- Hill, P. G., Hogan, R. J., Manners, J., and Petch, J. C. (2012). Parametrizing the horizontal inhomogeneity of ice water content using CloudSat data products. *Q. J. Roy. Meteorol. Soc.*, **In press**.
- Hogan, R. J. and Illingworth, A. J. (1999). The potential of spaceborne dual-wavelength radar to make global measurements of cirrus clouds. *Journal of Atmospheric and Oceanic Technology*, **16**(5), 518–531.
- Hogan, R. J. and Illingworth, A. J. (2000). Deriving cloud overlap statistics from radar. *Q. J. Roy. Meteorol. Soc.*, **126**, 2903–2909.
- Hogan, R. J. and Illingworth, A. J. (2003). Parameterizing ice cloud inhomogeneity and the overlap of inhomogeneities using cloud radar data. *J. Atm. Sci.*, **60**(5), 756–767.
- Hogan, R. J. and Kew, S. F. (2005). A 3D stochastic cloud model for investigating the radiative properties of inhomogeneous cirrus clouds. *Q. J. Roy. Meteorol. Soc.*, **131**(611), 2585–2608.
- Hogan, R. J. and Shonk, J. K. P. (2012). Incorporating the effects of 3D radiative transfer in the presence of clouds into two-stream radiation schemes. *Submitted to J. Atm. Sci.*
- Jakob, C. and Klein, S. A. (1999). The role of vertically varying cloud fraction in the parametrization of microphysical processes in the ECMWF model. *Q. J. Roy. Meteorol. Soc.*, **125**(555), 941–965.

- Jensen, J. (1906). Sur les fonctions convexes et les inégalités entre les valeurs moyennes. *Acta Mathematica*, **30**, 175–193. 10.1007/BF02418571.
- Kato, S., Sun-Mack, S., Miller, W. F., Rose, F. G., Chen, Y., Minnis, P., and Wielicki, B. A. (2010). Relationships among cloud occurrence frequency, overlap and effective thickness derived from CALIPSO and CloudSat merged vertical profiles. *J. Geophys. Res.*, **115**(D00H28).
- Khairoutdinov, M. F. and Randall, D. A. (2001). A cloud resolving model as a cloud parameterization in the NCAR Community Climate System Model: Preliminary results. *Geophys. Res. Lett.*, **28**(18), 3617–3620.
- King, W. D., Maher, C. T., and Hepburn, G. A. (1981). Further performance tests on the CSIRO liquid water probe. *J. Appl. Met.*, **20**(2), 195–202.
- Kogan, Z. N., Lilly, D. K., Kogan, Y. L., and Filyushkin, V. (1995). Evaluation of radiative parameterizations using an explicit cloud microphysical model. *Atmospheric Research*, **35**(2-4), 157–172.
- Lacis, A. A. and Oinas, V. (1991). A description of the correlated k distribution method for modeling nongray gaseous absorption, thermal emission, and multiple scattering in vertically inhomogeneous atmospheres. *J. Geophys. Res.*, **96**(D5), 9027–9063.
- Larson, V. E., Wood, R., Field, P. R., Golaz, J.-C., Haar, T. H. V., and Cotton, W. R. (2001). Systematic biases in the microphysics and thermodynamics of numerical models that ignore subgrid-scale variability. *J. Atm. Sci.*, **58**(9), 1117–1128.
- Larson, V. E., Golaz, J.-C., Jiang, H., and Cotton, W. R. (2005). Supplying local microphysics parameterizations with information about subgrid variability: Latin hypercube sampling. *Journal of the Atmospheric Sciences*, **62**(11), 4010–4026.
- Lee, S., Kahn, B. H., and Teixeira, J. (2010). Characterization of cloud liquid water content distributions from CloudSat. *J. Geophys. Res.*, **115**(D20203).
- Lewis, G. M., Austin, P. H., and Szczodrak, M. (2004). Spatial statistics of marine boundary layer clouds. *J. Geophys. Res.*, **109**(D04104).
- Li, J., Dobbie, S., Räisänen, P., and Min, Q. (2005). Accounting for unresolved clouds in a 1-D solar radiative transfer model. *Q. J. Roy. Meteorol. Soc.*, **131**, 1607–1629.

- Liang, X.-Z. and Wang, W.-C. (1997). Cloud overlap effects on general circulation model simulations. *J. Geophys. Res.*, **102**(D10), 11039–11047.
- Liou, K.-N. (1986). Influence of cirrus clouds on weather and climate processes: A global perspective. *Monthly Weather Review*, **114**(6), 1167–1199.
- Mace, G. G. and Benson-Troth, S. (2002). Cloud overlap characteristics derived from long-term cloud radar data. *J. Climate*, **15**, 2505–2515.
- Mace, G. G., Zhang, Q., Vaughan, M., Marchand, R., Stephens, G., Trepte, C., and Winker, D. (2009). A description of hydrometeor layer occurrence statistics derived from the first year of merged CloudSat and CALIPSO data. *J. Geophys. Res.*, **114**(D00A26).
- Manners, J., Thelen, J.-C., Petch, J., Hill, P., and Edwards, J. M. (2009). Two fast radiative transfer methods to improve the temporal sampling of clouds in numerical weather prediction and climate models. *Q. J. Roy. Meteorol. Soc.*, **135**, 457–468.
- Marchand, R., Mace, G. G., Ackerman, T., and Stephens, G. (2008). Hydrometeor detection using Cloudsat – an earth-orbiting 94-GHz cloud radar. *Journal of Atmospheric and Oceanic Technology*, **25**(4), 519–533.
- Marshak, A., Davis, A., Wiscombe, W., and Cahalan, R. (1997). Scale invariance of liquid water distributions in marine stratocumulus. Part II: Multifractal properties and intermittency issues. *J. Atm. Sci.*, **54**(11), 1423–1444.
- McKee, T. B. and Cox, S. K. (1974). Scattering of visible radiation by finite clouds. *J. Atm. Sci.*, **31**(7), 1885–1892.
- Meador, W. E. and Weaver, W. R. (1980). Two-stream approximations to radiative transfer in planetary atmospheres: A unified description of existing methods and a new improvement. *J. Atmos. Sci.*, **37**(3), 630–643.
- Mittermaier, M. (2012). A critical assessment of surface cloud observations and their use for verifying cloud forecasts. *Q. J. Roy. Meteorol. Soc.*, **In press**.
- Morcrette, C. J. (2012). Improvements to a prognostic cloud scheme through changes to its cloud erosion parametrization. *Atmospheric Science Letters*, **13**(2), 95–102.

- Morcrette, J.-J. (2000). On the effects of the temporal and spatial sampling of radiation fields on the ECMWF forecasts and analyses. *Mon. Wea. Rev.*, **128**(3), 876–887.
- Morcrette, J.-J. and Fouquart, Y. (1986). The overlapping of cloud layers in shortwave radiation parameterizations. *J. Atm Sci*, **43**, 321–328.
- Morcrette, J.-J. and Jakob, C. (2000). The response of the ECMWF model to changes in the cloud overlap assumption. *Monthly Weather Review*, **128**(6), 1707–1732.
- Morcrette, J.-J., Barker, H. W., Cole, J. N. S., Iacono, M. J., and Pincus, R. (2008). Impact of a new radiation package, McRad, in the ECMWF integrated forecasting system. *Monthly Weather Review*, **136**(12), 4773–4798.
- Naud, C. M., Del Genio, A., Mace, G. G., Benson, S., Clothiaux, E. E., and Kollias, P. (2008). Impact of dynamics and atmospheric state on cloud vertical overlap. *J. Climate*, **21**, 1758–1770.
- Oreopoulos, L. and Cahalan, R. F. (2005). Cloud inhomogeneity from MODIS. *J. Climate*, **18**, 5110–5124.
- Oreopoulos, L. and Davies, R. (1998a). Plane parallel albedo biases from satellite observations. Part I: Dependence on resolution and other factors. *J. Climate*, **11**(5), 919–932.
- Oreopoulos, L. and Davies, R. (1998b). Plane parallel albedo biases from satellite observations. Part II: Parameterizations for bias removal. *J. Climate*, **11**(5), 933–944.
- Oreopoulos, L. and Khairoutdinov, M. (2003). Overlap properties of clouds generated by a cloud-resolving model. *J. Geophys. Res.*, **108**(D15), 4479.
- Oreopoulos, L. and Norris, P. M. (2011). An analysis of cloud overlap at a midlatitude atmospheric observation facility. *Atmospheric Chemistry and Physics Discussions*, **11**(1), 597–625.
- Oreopoulos, L., Mlawer, E. J., Delamere, J. S., Shippert, T., Cole, J., Fomin, B., Iacono, M. J., Jin, Z., Li, J., Manners, J., Risnen, P., Rose, F. G., Zhang, Y., Wilson, M. J., and Rossow, W. B. (2012). The continual intercomparison of radiation codes: Results from phase I. *J. Geophys. Res.*, **117**(D6).
- Pincus, R. and Klein, S. A. (2000). Unresolved spatial variability and microphysical process rates in large-scale models. *J. Geophys. Res.*, **105**(D22), 27059–27065.

- Pincus, R., McFarlane, S. A., and Klein, S. A. (1999). Albedo bias and the horizontal variability of clouds in subtropical marine boundary layers: Observations from ships and satellites. *J. Geophys. Res.*, **104**(D6), 6183–6191.
- Pincus, R., Barker, H. W., and Morcrette, J.-J. (2003). A fast, flexible, approximate technique for computing radiative transfer in inhomogeneous cloud fields. *J. Geophys. Res.*, **108**(D13), 4376.
- Pincus, R., Hannay, C., and Evans, K. F. (2005). The accuracy of determining three-dimensional radiative transfer effects in cumulus clouds using ground-based profiling instruments. *Journal of the Atmospheric Sciences*, **62**(7), 2284–2293.
- Pomroy, H. R. and Illingworth, A. J. (2000). Ice cloud inhomogeneity: Quantifying bias in emissivity from radar observations. *Geophys. Res. Lett.*, **27**(14), 2101–2104.
- Räisänen, P. and Barker, H. W. (2004). Evaluation and optimization of sampling errors for the Monte Carlo Independent Column Approximation. *Q. J. Roy. Meteorol. Soc.*, **130**, 2069–2085.
- Räisänen, P. and Järvinen, H. (2010). Impact of cloud and radiation scheme modifications on climate simulated by the ECHAM5 atmospheric GCM. *Q. J. Roy. Meteorol. Soc.*, **136**(652), 1733–1752.
- Räisänen, P., Isaac, G. A., Barker, H. W., and Gultepe, I. (2003). Solar radiative transfer for stratiform clouds with horizontal variations in liquid-water path and droplet effective radius. *Quarterly Journal of the Royal Meteorological Society*, **129**(592), 2135–2149.
- Räisänen, P., Barker, H. W., Khairoutdinov, M. F., Li, J., and Randall, D. A. (2004). Stochastic generation of subgrid-scale cloudy columns for large-scale models. *Q. J. Roy. Meteorol. Soc.*, **130**, 2047–2067.
- Räisänen, P., Barker, H. W., and Cole, J. N. S. (2005). The Monte Carlo Independent Column Approximation's conditional random noise: Impact on simulated climate. *J. Climate*, **18**(22), 4715–4730.
- Räisänen, P., Järvenoja, S., Järvinen, H., Giorgetta, M., Roeckner, E., Jylhä, K., and Ruosteenoja, K. (2007). Tests of Monte Carlo Independent Column Approximation in the ECHAM5 atmospheric GCM. *J. Climate*, **20**(19), 4995–5011.

- Räisänen, P., Järvenoja, S., and Järvinen, H. (2008). Noise due to the Monte Carlo independent-column approximation: short-term and long-term impacts in ECHAM5. *Q. J. Roy. Meteorol. Soc.*, **134**, 481–495.
- Ramanathan, V., Cess, R. D., Harrison, E. F., Minnis, P., Barkstrom, B. R., Ahmad, E., and Hartmann, D. (1989). Cloud-radiative forcing and climate: Results from the earth radiation budget experiment. *Science*, **243**(4887), 57–63.
- Ramaswamy, V., Boucher, O., Haigh, J., Hauglustaine, D., Haywood, J., Myhre, G., Nakajima, T., Shi, G., and Solomon, S. (2001). Radiative forcing of climate change. In J. Houghton, Y. Ding, D. Griggs, M. Nougier, P. van der Linden, X. Dai, K. Maskell, and C. Johnson, editors, *Climate Change 2001: The Scientific Basis. Contribution of Working Group I to the Third Assessment Report of the Intergovernmental Panel on Climate Change*, chapter 6, pages 349–416. Cambridge University Press, Cambridge, United Kingdom and New York, USA.
- Ronnholm, K., Baker, M. B., and Harrison, H. (1980). Radiative transfer through media with uncertain or variable parameters. *Journal of the Atmospheric Sciences*, **37**(6), 1279–1290.
- Rossow, W. B., Delo, C., and Cairns, B. (2002). Implications of the observed mesoscale variations of clouds for the earth's radiation budget. *J. Climate*, **15**(6), 557–585.
- Shonk, J. K. P. and Hogan, R. J. (2008). Tripleclouds: An efficient method for representing horizontal cloud inhomogeneity in 1D radiation schemes by using three regions at each height. *J. Climate*, **21**(11), 2352–2370.
- Shonk, J. K. P. and Hogan, R. J. (2010). Effect of improving representation of horizontal and vertical cloud structure on the Earth's radiation budget. Part II: The global effects. *Q. J. Roy. Meteorol. Soc.*, **136**, 1205–1215.
- Shonk, J. K. P., Hogan, R. J., Mace, G. G., and Edwards, J. M. (2010). Effect of improving representation of horizontal and vertical cloud structure on the Earth's radiation budget. Part I: Review and parameterisation. *Q. J. Roy. Meteorol. Soc.*, **136**, 1191–1204.
- Shonk, J. K. P., Hogan, R. J., and Manners, J. (2012). Impact of improved representation of horizontal and vertical cloud structure in a climate model. *Climate Dynamics*, **38**(11-12), 2365–2376.

- Slingo, A. and Schrecker, H. M. (1982). On the shortwave radiative properties of stratiform water clouds. *Q. J. Roy. Meteorol. Soc.*, **108**(456), 407–426.
- Smith, R. N. B. (1990). A scheme for predicting layer clouds and their water content in a general circulation model. *Q. J. Roy. Meteorol. Soc.*, **116**(492), 435–460.
- Smith, S. A. and Del Genio, A. D. (2001). Analysis of aircraft, radiosonde, and radar observations in cirrus clouds observed during FIRE II: The interactions between environmental structure, turbulence, and cloud microphysical properties. *J. Atm. Sci.*, **58**(5), 451–461.
- Soden, B. J. and Held, I. M. (2006). An assessment of climate feedbacks in coupled ocean-atmosphere models. *Journal of Climate*, **19**(14), 3354–3360.
- Stephens, G. L., Vane, D. G., Tanelli, S., Im, E., Durden, S., Rokey, M., Reinke, D., Partain, P., Mace, G. G., Austin, R., L'Ecuyer, T., Haynes, J., Lebsock, M., Suzuki, K., Waliser, D., Wu, D., Kay, J., Gettelman, A., Wang, Z., and Marchand, R. (2008). CloudSat mission: Performance and early science after the first year of operation. *J. Geophys. Res.*, **113**(D00A18).
- Su, W., Bodas-Salcedo, A., Xu, K.-M., and Charlock, T. P. (2010). Comparison of the tropical radiative flux and cloud radiative effect profiles in a climate model with Clouds and the Earth's Radiant Energy System (CERES) data. *J. Geophys. Res.*, **115**(D1).
- Szczap, F., Isaka, H., Saute, M., Guillemet, B., and Ioltukhovski, A. (2000). Effective radiative properties of bounded cascade nonabsorbing clouds: Definition of the equivalent homogeneous cloud approximation. *J. Geophys. Res.*, **105**(D16), 20617–20633.
- Tian, L. and Curry, J. A. (1989). Cloud overlap statistics. *J. Geophys. Res.*, **94**(D7), 9925–9935.
- Tiedtke, M. (1993). Representation of clouds in large-scale models. *Monthly Weather Review*, **121**(11), 3040–3061.
- Tiedtke, M. (1996). An extension of cloud-radiation parameterization in the ECMWF model: The representation of subgrid-scale variations of optical depth. *Monthly Weather Review*, **124**(4), 745–750.
- Tompkins, A. M. (2002). A prognostic parameterization for the subgrid-scale variability of water vapor and clouds in large-scale models and its use to diagnose cloud cover. *J. Atm. Sci.*, **59**(12), 1917–1942.

- Tompkins, A. M. and Giuseppe, F. D. (2007). Generalizing cloud overlap treatment to include solar zenith angle effects on cloud geometry. *J. Atm. Sci.*, **64**(6), 2116–2125.
- Trenberth, K. E., Fasullo, J. T., and Kiehl, J. (2009). Earth's global energy budget. *Bull. Amer. Meteor. Soc.*, **90**(3), 311–323.
- Van Blerkom, D. J. (1971). Diffuse reflection from clouds with horizontal inhomogeneities. *Astrophys. J.*, **166**, 235–242.
- Vaughan, M., Young, S., Winker, D., Powell, K., Omar, A., Liu, Z., Hu, Y., and Hostetler, C. (2004). Fully automated analysis of space-based lidar data: An overview of the CALIPSO retrieval algorithms and data products. *Proc. SPIE Int. Soc. Opt. Eng.*, **5575**, 16–30.
- Venema, V., Schomburg, A., Ament, F., and Simmer, C. (2007). Two adaptive radiative transfer schemes for numerical weather prediction models. *Atmospheric Chemistry and Physics*, **7**(21), 5659–5674.
- Walters, D. N. (2012). The Met Office Unified Model Global Atmosphere 4.0 and JULES Global Land 4.0 configurations. *In preparation*.
- Walters, D. N., Best, M. J., Bushell, A. C., Copsey, D., Edwards, J. M., Falloon, P. D., Harris, C. M., Lock, A. P., Manners, J. C., Morcrette, C. J., Roberts, M. J., Stratton, R. A., Webster, S., Wilkinson, J. M., Willett, M. R., Boutle, I. A., Earnshaw, P. D., Hill, P. G., MacLachlan, C., Martin, G. M., Moufouma-Okia, W., Palmer, M. D., Petch, J. C., Rooney, G. G., Scaife, A. A., and Williams, K. D. (2011). The Met Office Unified Model Global Atmosphere 3.0/3.1 and JULES Global Land 3.0/3.1 configurations. *Geoscientific Model Development Discussions*, **4**(2), 1213–1271.
- Wang, L. and Dessler, A. E. (2006). Instantaneous cloud overlap statistics in the tropical area revealed by ICESat/GLAS data. *Geophys. Res. Lett.*, **33**(L15804).
- Weinman, J. A. and Swarztrauber, P. N. (1968). Albedo of a striated medium of isotropically scattering particles. *J. Atm. Sci.*, **25**(3), 497–501.
- Wild, M. and Roeckner, E. (2006). Radiative Fluxes in the ECHAM5 General Circulation Model. *J. Climate*, **19**(16), 3792–3809.

- Willén, U., Crewell, S., Baltink, H. K., and Sievers, O. (2005). Assessing model predicted vertical cloud structure and cloud overlap with radar and lidar ceilometer observations for the Baltex Bridge Campaign of CLIWA-NET. *Atmospheric Research*, **75**(3), 227–255.
- Wilson, D. R., Bushell, A. C., Kerr-Munslow, A. M., Price, J. D., and Morcrette, C. J. (2008a). PC2: A prognostic cloud fraction and condensation scheme. I: Scheme description. *Q. J. Roy. Meteorol. Soc.*, **134**, 2093–2107.
- Wilson, D. R., Bushell, A. C., Kerr-Munslow, A. M., Price, J. D., Morcrette, C. J., and Bodas-Salcedo, A. (2008b). PC2: A prognostic cloud fraction and condensation scheme. II: Climate model simulations. *Q. J. Roy. Meteorol. Soc.*, **134**, 2109–2125.
- Wood, R. and Field, P. (2011). The distribution of cloud horizontal sizes. *J. Climate*, **24**(18), 4800–4816.
- Wu, X. and Liang, X.-Z. (2005). Radiative effects of cloud horizontal inhomogeneity and vertical overlap identified from a monthlong cloud-resolving model simulation. *J. Atm. Sci.*, **62**(11), 4105–4112.
- Zhang, Y., Klein, S. A., Boyle, J., and Mace, G. G. (2010). Evaluation of tropical cloud and precipitation statistics of Community Atmosphere Model version 3 using CloudSat and CALIPSO data. *J. Geophys. Res.*, **115**(D12).
- Zwiers, F. W. and von Storch, H. (1995). Taking serial correlation into account in tests of the mean. *J. Climate*, **8**(2), 336–351.